Oblique Angle Deposition of Thin Films – Theory, Modelling, and Application

Der Fakultät für Physik und Geowissenschaften
der Universität Leipzig
genehmigte
DISSERTATION
zur Erlangung des akademischen Grades

Doctor rerum naturalium

Dr. rer. nat.,

vorgelegt

von M.Sc. Christoph Grüner

geboren am 12.01.1988 in Halle / Saale

Gutachter: Prof. Dr. Dr. h.c. Bernd Rauschenbach
Prof. Dr. Agustín R. Gonzólez-Elipe

Tag der Verleihung: 17. Juni 2019

Bibliographische Beschreibung

Grüner, Christoph
Oblique Angle Deposition of Thin Films – Theory, Modelling, and Application
Universität Leipzig, Dissertation
133 S., 199 Lit., 69 Abb., 2 Anlagen

Referat:

Mit dem Ziel ein besseres Verständnis des Einflusses des Einfallswinkels in der physikalischen Gasphasenabscheidung zu erreichen, wurden experimentell realisierte und am Computer simulierte Dünnschichten untersucht. Als Abscheidetechniken kamen sowohl Elektronenstrahl-Verdampfen als auch Ionenstrahl-Zerstäubung zum Einsatz. Es wurden die Materialien Germanium, Silicium und Molybdän verwendet, die bei verschiedenen Einfallswinkeln, verschiedenen Substrattemperaturen und variiertem Restgas abgeschieden wurden. Die beobachteten Zusammenhänge, von bspw. kolumnarer Verkippung und Einfallswinkel, konnten nicht mit den etablierten Modellen in Einklang gebracht werden. Um das genaue Zusammenspiel von Abschattung und Konkurrenz-Wachstum zu verstehen, wurde eine „on-lattice“ Computersimulation entwickelt, mit dem besonderen Augenmerk auf die Vermeidung von gitterbasierten Anisotropien. Dies wurde durch Vergleich mit einer, ebenfalls entwickelten, „off-lattice“ Simulation sichergestellt. Ausgehend von den beobachteten Effekten konnte ein analytisches Modell entwickelt werden, welches die Materialeigenschaften und Abscheidebedingungen in einen einzigen Parameter vereint. Die Vorhersagen des Modells wurden an den hergestellten Schichten, den Computersimulationen und an Literaturdaten verifiziert. Abschließend werden Methoden aufgezeigt, die schräg abgeschiedenen nanostrukturierten Schichten verschiedenen Anwendungen anzupassen. Dies umfasst die *in situ* Dotierung von Siliciumnanostrukturen, die Erzeugung von Kern-Schale-Strukturen, sowie die biochemische Oberflächenfunktionalisierung von Silbernanostrukturen. Am Beispiel der letztgenannten werden verschiedene Anwendungen in der Biosensorik detaillierter vorgestellt.

Abstract:

With the aim to gain a deeper understanding of the role of the angle of incidence in physical vapor deposition, experimental, and computer-based studies were conducted. Electron beam evaporation and ion beam sputtering were used as deposition methods. The materials germanium, silicon, and molybdenum were deposited at different incidence angle, different temperatures and varied residual gas atmospheres. Established models could not be used to adequately explain the obtained relations between morphological parameters, as the tilt angle, with the incidence angle. To investigate the interplay of self-shadowing and competitive growth, an on-lattice simulation was developed. Care was taken to avoid any artificial anisotropy. Comparison with an, additionally developed, off-lattice simulation was used to verify this. Based on the made observations, an analytical model was deduced that combines the material properties and the deposition conditions into a single parameter. The predictions of this model were verified for the experimental observations, the results of the computer simulations, and on literature data. In the last part of the thesis, methods are shown that facilitate to modify the properties of the obliquely deposited thin films to fit requirements of various applications. This includes *in situ* doping of silicon nanostructures, creation of core-shell structures, as well as biochemical surface functionalization of silver nanostructures. On the example of the latter, various bio-sensing applications are presented.

Contents

1 Motivation

Many technological important properties of tools and devices are determined by the structure and composition of their surface. Properties, such as optical behavior (e.g., color and reflectivity), hardness, and biocompatibility can be modified and improved by providing surface coatings of different materials and morphologies. Besides, coating technologies also allow to manufacture electronic and optic devices, such as thin film transistors, laser cavities, or optical sensors. Due to the large number of involved materials and the versatile requirements on the final morphology of the coating, a large variety of methods to control and design the desired surface topography precisely has been developed.

These techniques are usually divided into two groups: Chemical Vapor Deposition (CVD) and Physical Vapor Deposition (PVD). In PVD, material is brought into gas phase by physical techniques. For this purpose, the atoms are removed from a material source (the "target"), e.g. by evaporation, sputtering or laser ablation. The free atoms travel through the vacuum environment to the surface (the "substrate"), where they finally condense and become incorporated into the growing film.

Compared to CVD, the PVD approach allows to produce coatings with higher purity and a more precise and flexible control of the composition and morphology. A drawback is the more cost-intensive deposition equipment, since a better vacuum as well as a vaporization device are required. Nevertheless, PVD coatings become increasingly important for industrial applications due to the superior coating quality. Such PVD made coatings can be found in manifold tools of the everyday life such as optical storages devices (e.g. DVDs), tools, and lenses, to name just a few. Additionally, the production of high-technology devices as silicon-on-insulator transistors or X-ray mirrors is strongly connected to the use of PVD techniques.

The control of the many parameters during PVD opens the opportunity to influence the properties of the growing films. The roles of the substrate temperature, growth rate, vapor composition, vapor energy, and a few more parameters are of interest for the scientific and industrial community and are part of various research items and projects. A less often considered parameter is the angle of incidence of the vaporized atoms. Previous research has already shown that even slightly oblique incidence angles can have an enormous impact on the structural film parameters, such as density and microstructure. Hence, important film properties as hardness, conductivity, or refractive index are influenced.

Combining PVD with highly oblique particle incidence angles results in the self-assembled growth of highly porous thin films composed of separated nanostructures. This technique, known as oblique angle deposition (OAD), allows to create nanostructured thin films with completely new structural features and properties. Due to the large surface area, such films open the opportunity to fabricate sensors based on Surface Enhanced Raman Scattering (SERS), for example. The development of such sensors plays a key role for the certain, precise, and fast identification and quantification of environmental toxics or human blood constituents, e.g., and is therefore in the focus of considerable research activities nowadays.

It is a surprising fact that oblique deposition has gained just minor attention, because perfectly vertical deposition is just an idealized case. True deposition more often than not is oblique, caused by the geometric relation between target und substrate as well as due to surface roughness and topography.

The first aim of this thesis is to understand the role of the angle of incidence, as well as its interplay with other deposition parameters, like the substrate temperature, on the surface topography. For this purpose, a new model is developed based on experimental observations, computer simulations, and a review of commonly used theoretical models are used to develop a new model, which describes the morphology of obliquely grown films with a higher accuracy than previous models.

The second aim is to find methods to improve OAD thin film properties for later device application. Therefore, methods are developed to alter surface and materials properties of the OAD nanostructures, to fit specific requirements. The application of such modified OAD thin films for bio-sensing applications is demonstrated in detail.

2 Basic Concepts

2.1 Physical vapor deposition (PVD)

The growth of thin films with PVD methods can be divided into three processes that each atom undergoes subsequently, as shown in Figure 2.1 **a**. These are (i) the generation of the vapor particles (atoms or molecules), (ii) the travel of the particles from the target to the substrate, and finally (iii) the condensation of the vapor particles on the substrates surface. The physics of these three processes shall be shortly elucidated in the following sections, with focus on the last mentioned one, as it plays the crucial role for the oblique angle deposition.

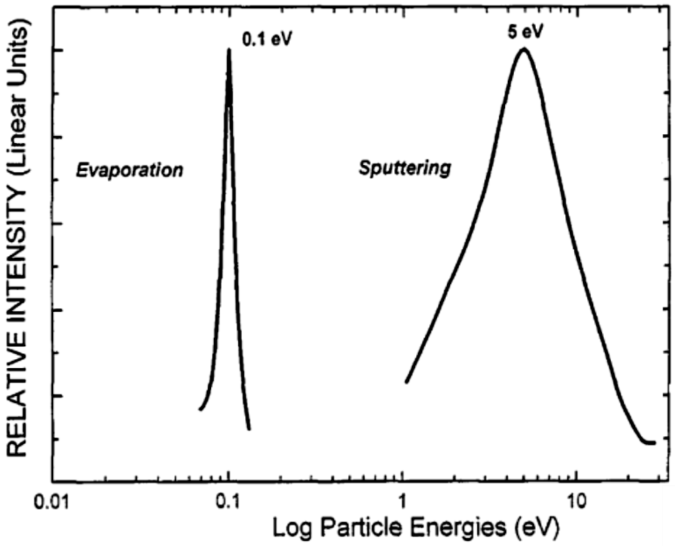

Figure 2.1: Comparison of typical particle energies of the two here used vaporization techniques. Image adapted from [1].

2.1.1 Particle Generation

Different techniques were developed to vaporize solid materials. One very often-used method is to evaporate the material. This can be done either by electric heating of a crucible liner, in which the material is placed ("thermal evaporation") or by treating the material directly with an electron beam. The last mentioned method has the advantage, that the energy is focused onto the material, and therefore the crucible that holds the material remains colder, reducing the amount of contaminations introduced from it. Electron beam evaporation is one of the used vaporization techniques for this thesis. As electron beams can reach high energy densities, nearly all materials can be evaporated by this method. Evaporated atoms have energies E that can be described with a Boltzmann distribution [2]:

$$f(E) = \frac{2}{\sqrt{\pi}}\left(\frac{1}{kT}\right)^{3/2} \sqrt{E}\, e^{-E/kT}\,, \tag{2.1.1}$$

with T denoting the temperature and k being the Boltzmann constant. Typical thermal energies lie in the range of < 0.2 eV (compare Figure 2.1 **b**). The flux of the evaporated material, defined as the deposited mass m onto an area A in a specific period of time dt, depends on the distance of the substrate to the source r and the relative angle θ of which the substrate is displaced from the source normal. An estimation is given by the Knudsen equation [3]

$$\frac{\mathrm{d}m}{A\,\mathrm{d}t} = \frac{M}{4\pi t}\frac{\cos\theta}{r^2}\,. \tag{2.1.2}$$

Hereby, M denotes the molar mass of the evaporated species. This equation is valid, if the angular flux dn from the particle source through a solid angle dω follows Knudsen's cosine-law

$$\mathrm{d}n \sim \frac{\mathrm{d}\omega}{\pi}\cos^n\theta\,, \tag{2.1.3}$$

with $n = 1$. Notice that this is not equivalent to the polar angular-probability distribution function $g(\theta)$, that can be found by integrating dn over all azimuthal angles, which finally yields (following [4])

$$g(\theta) = 2\sin\theta\cos\theta = \sin 2\theta\,. \tag{2.1.4}$$

To create such a distribution in a Monte-Carlo simulation from a random number $0 \leq x \leq 1$, one has to choose the angle of departure as

$$\theta = \arcsin\sqrt{x}\,.\ [5] \tag{2.1.5}$$

Notice further, that $n = 1$ in eq. (2.1.3) is valid for effusion from a tube or a Knudsen cell, but not necessarily for free evaporation into a vacuum. In fact, Nishimura *et al.* [6] investigated this distribution for the electron beam evaporation of gadolinium and found a dependence of n from the heating power P_h or rather the evaporation rate. They found n values of 1.0, 2.2, and 4.6 for P_h = 3 kW, 4 kW and 12 kW, respectively. This may be attributed to the fact that at higher heating powers, especially in electron beam evaporation, strong thermal gradients exist so that thermal equilibrium is left behind. For the same reason, the Boltzmann distribution also is an approximation at these conditions, at best.

In a second vaporization technique, primary ions are accelerated and directed onto the targets surface. When the energetic ions hit the target, they transfer their momentum and energy to the atoms of the target. If a target atom gains an energy, larger than a threshold energy, it has a chance to be emitted from the target - a process called sputtering. The average amount of target atoms, generated per incident primary ion is called sputter yield and depends on a few parameters, like the mass, the energy, and the angle of incidence of the primary ions as well as on the atomic mass and the surface binding energy of the target material. The flux of the sputtered target atoms therefore depends on the sputtering yield and the current of ions hitting the target. Basic mathematical description of sputtering can be found, e.g., from Sigmund [7]. The energy of the sputtered atoms can be approximately estimated by the Thompson distribution [8], which is mainly characterized by a maximum at approximately the half of the surface binding energy (few eV, compare Figure 2.1 **b**) and an energy tail, following $f(E) \sim E^{-2}$. Therefore, the energy of sputtered particles is generally larger than that of evaporated species.

Depending on the method to create the primary ions, different sputtering techniques are distinguished. Most common is magnetron sputtering, where the ions are extracted from a plasma that resides directly above the target. This technique has the disadvantage that the sputtered atoms have to travel through the plasma, so that their trajectories are likely be influenced by collisions. Another method is ion beam sputtering (IBS). In this method, the creation of the ions is spatially separated from the sputtering target in a special ion beam source. As no plasma is necessary in vicinity of the target, lower background pressures are possible inside the deposition system. Therefore, ion beam sputter deposition (IBSD) is the second method used for this thesis. A more detailed characterization of IBSD, regarding the sputter yield, energy distribution, and angular distribution can be found in [9-11].

2.1.2 Transport through the gas phase

The vaporized particles move away from the target surface. When they hit the substrate or the walls of the deposition chamber, they condense. In-between there is a chance that the atoms collide with atoms or molecules from the residual gas in the deposition system. The mean-free-path $\bar{l}$ of atoms in a low pressure environment depends on the pressure p, the atomic or molecular diameter d_m and the temperature T of the residual gas and can be estimated with the following equation [12]:

$$\bar{l} = \frac{kT}{\sqrt{2}\,\pi\, p\, d_m^2}\,. \tag{2.1.6}$$

This equation is only valid if the particle velocities are Maxwell-distributed (thermal equilibrium) and for the approximation of an ideal gas. This is not given here, as the evaporated or sputtered atoms have much higher energies than the thermalized residual gas atoms, leading to a higher mean-free-path [2]. Nevertheless, it can be used to estimate the vacuum requirements, to assure ballistic transport of the material from the target to the substrate. For a typical target-substrate distance of 30 cm and thermal background gas, a vacuum better than approximately $2 \cdot 10^{-4}$ mbar is required. If the pressure is higher than this, the particle stream at the substrate will no longer be parallel, affecting the self-shadowing effect, which is crucial to produce nanostructures with OAD.

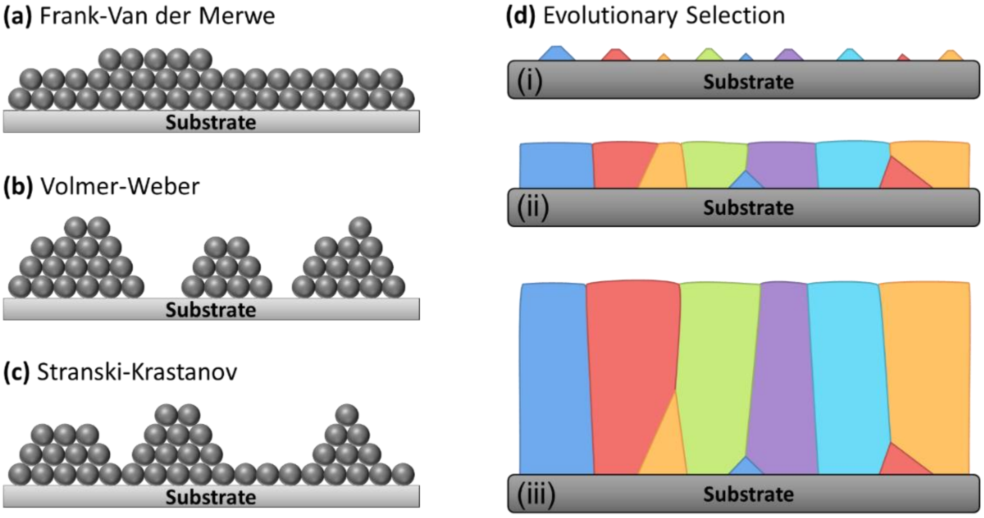

Figure 2.2: (**a**), (**b**), and (**c**) illustrate the different possible growth modes. (**d**) illustrates the coalescence of randomly oriented nuclei, and the evolutionary selection of specific, fast growing crystallite orientations (indicated by different colors).

2.1.3 Film growth

When the atoms arrive at the substrate and the growing film, different processes can happen. If the atoms have high enough energies, they can be reflected or induce further sputtering. If the substrate temperature is high enough, the atoms may shortly adsorb to the surface, before they are re-evaporated again. These processes shall not be taken into account in the following discussion, as they are not expected at the used energy and temperature regimes. Atoms that have reached the substrates surface may have the chance to diffuse over it, provided the temperature of the substrate or the atoms kinetic energy are large enough. This diffusion is a random-walk process over the energy landscape of the substrates surface. If enough diffusing atoms - called adatoms – stick together, nuclei are formed. Details about the thermodynamics and kinetics of the nucleation process can be found in [13].

Three possible growth modes are typically distinguished for crystalline materials [14]. The thin film may grow layer-by-layer (called Frank-Van der Merwe growth, see Figure 2.2 **a**) if the adatoms tend to attach primarily on surface sites. In contrast, separated 3D nuclei form first, which coalesce later (Volmer-Weber growth, Figure 2.2 **b**), if the interaction between the adatoms is stronger. The third growth mode is a combination of the both first mentioned: At first, a closed wetting layer forms on which then islands grow (Stranski-Krastanov mode, Figure 2.2 **c**).

In this thesis, mostly a low substrate temperature was used so that typically island-growth was observed. Moreover, epitaxy is not observed, as usually amorphous fused silica or natively oxidized silicon is used as substrate. Consequently, the initially forming nuclei are either amorphous or, if they are crystalline, they are randomly oriented.

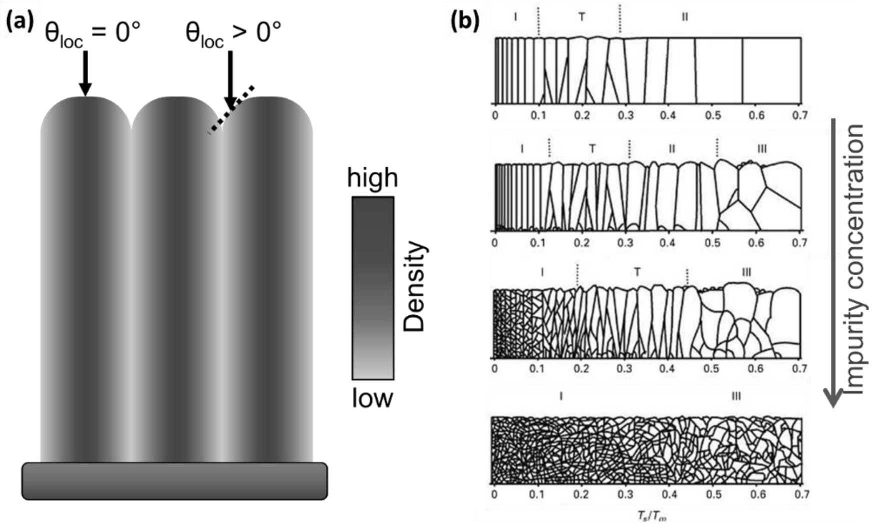

Figure 2.3: (**a**) Amorphous thin films develop a columnar structure as a consequence of the evolving surface roughness, which leads to horizontal density gradients. (**b**) Structure zone diagram, illustrating the influence of increasing impurity levels. At higher impurity concentrations, the columnar structure is lost and the crystallites do not extend from the substrate to the surface anymore. Image adapted from [15].

An often-observed feature in non-epitaxial films is a columnar structure [16-21]. For polycrystalline thin films, this fibrous structure arises due to the different orientations of the individual crystallites, which do not coalesce on crystallographic equivalent planes, and therefore remain distinguishable during growth of the thin film, as indicated in Figure 2.2 **d**. Furthermore, as the crystallites show and orientation dependent growth speed, some orientations are selected and grow preferably, while the other orientations loose this competitive process and therefore stop to grow [22]. Consequently, an evolutionary selection of crystallites occurs, in a way that the finally surviving crystallites show a fiber texture. The columnar morphology found in amorphous thin films, of course, has to originate from another process. This process is the increasing roughness of such growing films [23]. A rough surface in a collimated particle flux will always show regions, where the local angle of incidence θ_{loc} is larger than zero (compare Figure 2.3 **a**). The growth rate at these positions is reduced compared to the regions that are parallel to the substrate. Therefore, on these tilted regions, the thin film will grow slower in height and it will further exhibit a reduced density. The locally lower growth speed leads to an even higher roughness of the growing film and therefore intensifies this effect, what finally leads to the formation of distinguishable columns. It should be noted that the formation of such columns could be inhibited by contaminations that are incorporated during the growth process (see Figure 2.3 **b**). These impurities force the formation of new crystallites [15] or smear out the statistical roughness of the amorphous thin films.

The three mainly in this thesis used materials (Si, Ge, Mo) show such a columnar structure, as displayed in Figure 2.4.

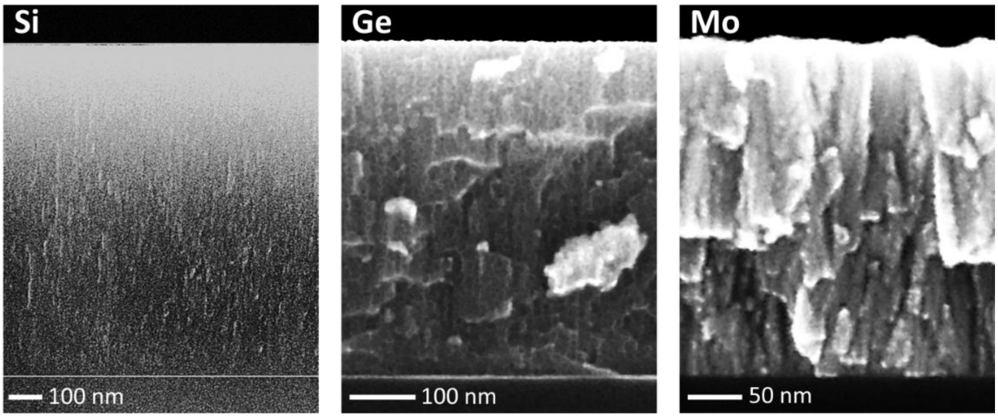

Figure 2.4: SEM image of Si, Ge, and Mo thin films, deposited at normal incidence by electron beam evaporation. Vertical features can be observed in all of these films, indicating the formation of a columnar morphology. The images are sharpened and contrast enhanced, to increase the visibility of the columns.

2.2 Deposition at oblique angles

If the substrate is tilted in a way that between the substrate normal and the direction of the incoming particle flux an angle θ is formed, the deposition process is called Oblique Angle Deposition (OAD). In normal, vertical, deposition, the columns are also oriented vertical, whereas in OAD, the columns are tilted into the direction of the incoming particles, as demonstrated in Figure 2.5 **a**. For highly oblique deposition conditions, the columns start to separate, forming a porous thin film, consisting of isolated needles. The obtained porosities can be as high as 90% [24, 25]. The reason for the columns to separate is the self-shadowing effect. It describes the fact that a highly oblique incidence combined with a rough surface leads to the formation of regions that are geometrically shadowed from the particle flux. In other words, these regions are not in direct line-of-sight with the particle source. Consequently, no further atoms reach the shadowed areas, which then remain unfilled. This is the cause for the formation of the porous structure.

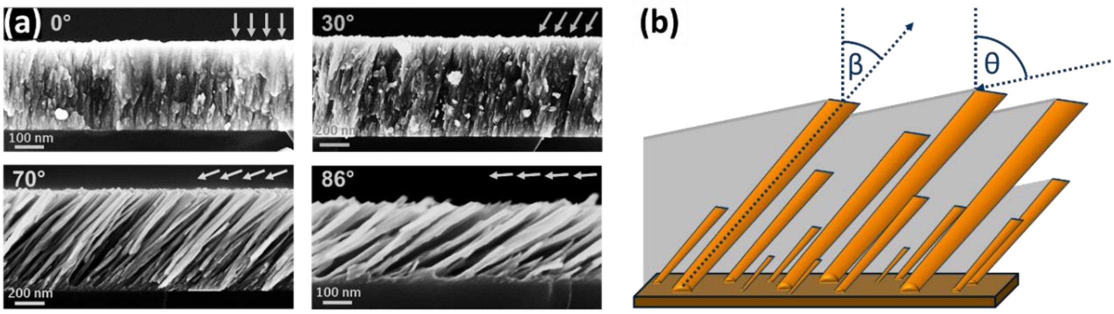

Figure 2.5: (**a**) Cross-sectional scanning electron microscopy images of Mo thin films, deposited at an increasingly oblique geometry. The actual angle of incidence is also indicated by the white arrows. A tilt of the columnar structure as well as the separation of individual needles at higher tilt angles can be observed. (**b**) Schematic illustration of the self-shadowing effect, which leads to the formation of the porous thin film morphology. All angles are measured with respect to the surface normal.

Considering surface diffusion and assuming oblique deposition onto a flat substrate, the formation of isolated structures starts, as soon as the geometric shadowing length l exceeds the mean surface diffusion length. The shadowing length is simply given by

$$l = h \cdot \tan\theta \,, \tag{2.2.1}$$

where h denotes the height of the object casting the shadow. Assuming spherical nuclei, h would equal the half of the nuclei's diameter. A noteworthy peculiarity of such a tilted columnar structure is, that the column's tilt angle β (measured also with respect to the substrates normal, compare Figure 2.5 **b**) is not equal to the angle of incidence θ. In fact, $\beta < \theta$ is found in all conducted experiments and computer simulations. This behavior is under discussion for decades and shall be discussed in more detail in chapter 6.

Historically, the deviation of the physical properties of obliquely deposited films was firstly discovered 1886 by Kundt [26]. It took until 1950, until König and Helwig were able to describe the microstructure of such films [27]. In 1966 Nieuwenhuizen and Haanstra performed scanning electron microscopy studies on OAD thin films, formulating the first hypothesis for a β-θ-relation [28]. Since then, OAD and related techniques have gained increasing interest as a highly versatile surface sculpturing technique and as a beautiful example for self-organization processes. [29]

2.3 Controlling the thin film morphology

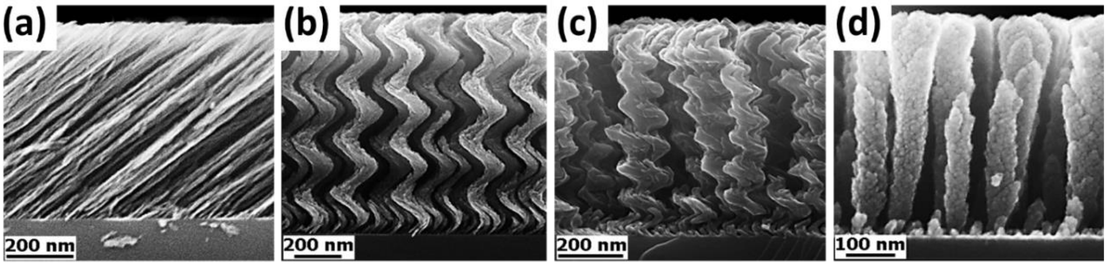

Figure 2.6: Silicon thin films, grown at highly oblique angles of incidence. (**a**) Tilted structures (no substrate rotation – OAD). (**b**) Spirals (slow rotation). (**c**) Screws (medium rotation speed). (**d**) Vertical columns (fast rotation).

As shown above (Figure 2.5 **a**), the angle of material incidence influences the tilt angle of the columns, as well as the porosity of the whole film. In order to customize the thin films further, an additional degree of freedom has to be introduced. An often-used parameter is azimuthal substrate rotation. The process is then often conducted at highly oblique deposition angles and usually called Glancing Angle Deposition (GLAD) [30]. Since the columns grow tilted into the direction of the incoming particle flux, a slow substrate rotation leads to the formation of spiral-like structures. The growing nanostructures thereby follow the substrate rotation. At larger rotation speeds, the pitch of the spirals decreases, so that the structures rather resemble screws. At high rotation frequencies, the influence of the individual revolutions gets lost and the structures degrade into upright columns. The influence of increasing rotation speed is shown in Figure 2.6 for the example of silicon.

Another parameter is the substrate temperature, for example, which influences the diameter of the individual structures. (see Figure 2.7 **a**, and compare section 4.1).

Combining different parameters, allows to create shapes that are more complex. A fast substrate rotation with a varying angle of incidence permits to vary the diameter of the individual nanostructures during growth (Figure 2.7 **b**, **c**). Further, a rapid change of the azimuthal substrate orientation allows to combine tilted needles with different orientations, so that zigzag structures (Figure 2.7 **d**) or n-fold spirals can be grown. More complex movement schemes, as phi-sweep [31, 32] and phase-rotation [33], can be used to further tune individual morphological properties of such film.

Another possibility to control the morphology of the thin films is to link GLAD with pre-patterned substrates. Such substrates can be prepared by classical lithography methods. As the nanostructures, forced by the shadowing effect, grow on the highest features of a surface, the prepared pre-pattern is transferred to the growing GLAD film (Figure 2.7 **e** – **g**). Therefore, it becomes possible to control the number and positioning of the individual structures. Furthermore, as the cross-sectional shape of such nanostructures is defined by the shadows from the surrounding nanostructures, pre-patterned substrates also enable to control this property.

Finally, different materials can be combined into the individual structure (Figure 2.7 **h**), further allowing to tailor the properties of such film.

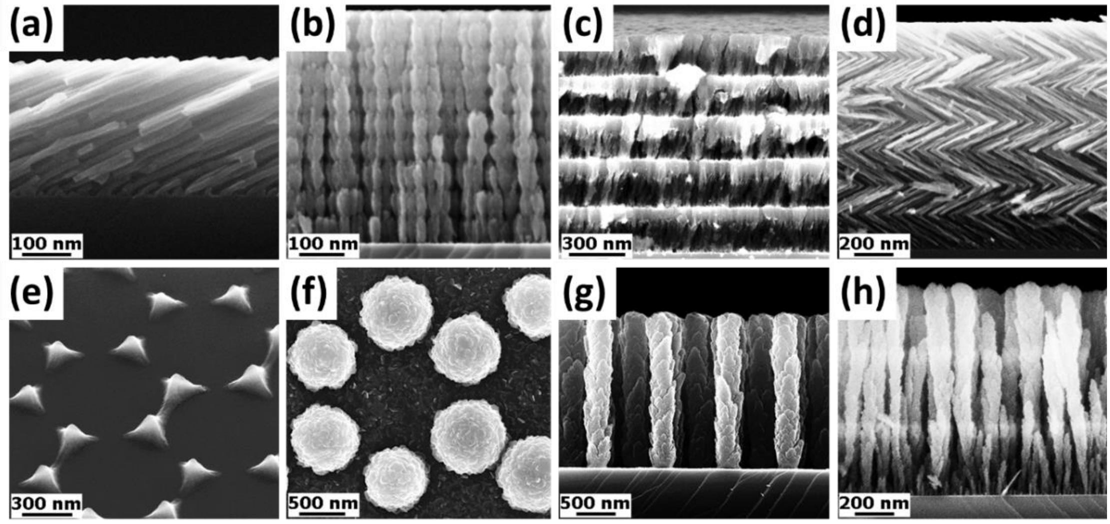

Figure 2.7: (**a**) Tilted silicon nanostructures, grown at a substrate temperature of 500 °C, showing a larger diameter than the ones deposited at room temperature. (**b**) and (**c**) show vertical columns, where the structure diameter was periodically varied during growth by control of the angle of incidence. (**d**) Rapid changes of the azimuthal angle allow combining tilted needles with different orientations. (**e**) Pre-patterned substrate with artificial seeds in a honeycomb pattern. (**f**) Top- and (**g**) side-view of GLAD structures grown on such a honeycomp template. (**h**) Vertical Si-Ge heterostructures. The Ge is located in the two brighter stripes**.**

Due to the great variety of producible shapes and the special properties of OAD and GLAD thin films, a wide field of applications is thinkable or already accessed. The large surface area that arises due to the open pore structure facilitates use for chemical applications as catalysis or sensing. The controllable density allows to precisely tailor the optical properties, as the refractive index, of GLAD films. Anti-reflection coatings, distributed Bragg reflectors, as well as optical filters are prominent examples of the use of such films. Furthermore, the mechanical, magnetic, thermal, and electrical properties of OAD and GLAD thin films can be tunes in a way, to be interesting for possible applications. Overviews are given in [29] and [34].

3 Experimental Methods

3.1 Sample preparation

3.1.1 Electron beam evaporation system

The majority of the samples that lead to the results presented in this thesis were produced by electron beam evaporation. The electron beam evaporation chamber (*e-beam chamber*, see Figure 3.1) is pumped by a turbomolecular pump, backed by a roots pump and has a base pressure in the range of $1 \cdot 10^{-9}$ mbar. It is equipped with a load-lock chamber that permits a fast sample transfer without the need to lose the vacuum. A four-pocket electron beam evaporator is located in the lower part of the chamber, while the sample holder is centered in the upper part. The entire deposition system is controlled by a software developed by BesTec, the company that realized the chamber as well. The sample holder allows a computer-controlled movement of the sample. This facilitates to set the angle of incidence θ and the azimuthal angle Φ (both with respect to the substrate normal). Complex movements can be programmed by using a ‘macro editor’. The substrate holder is further equipped with an electric heater, providing temperature control up to 850 °C. The growth speed is measured by a quartz crystal microbalance located at the top of the chamber. This sensor is calibrated for each material by test samples. Calibration is checked on a regular basis. A shutter between sample holder and evaporator allows an accurate control of the film thickness. The substrate holder is made of molybdenum and can be anchored at the substrate manipulator by a transfer rod. Samples are usually glued with carbon tape atop the sample holder. For higher deposition temperatures carbon paste is used to attach the sample, as the tape loses it adhesive force at around 300 °C.

Aiming at the substrate holder, different effusion cells allow manipulation of the material properties. A gas cracker cell was used to provide atomic hydrogen. It consists of a thin tungsten tube (inner diameter: 1 mm) that can be heated up to temperatures around 1900 °C, providing a mix of molecular and atomic hydrogen with a thermal energy distribution. Hydrogen flow is regulated by a mass flow controller (MFC), specially calibrated by the manufacturer for hydrogen. Typically, a gas flux of 0.4 sccm and a temperature of 1800 °C is chosen to increase the lifetime of the tungsten capillary.

A second effusion cell provides boron vapor, by sublimation of boron from an electrically heated carbon crucible liner. The cell temperature can be varied to set the desired boron flux. This was calibrated using test samples that were analyzed by secondary ion mass spectrometry (see section 3.2.3). Finally, a simple tube points to the sample holder, allowing the MFC regulated addition of process gases.

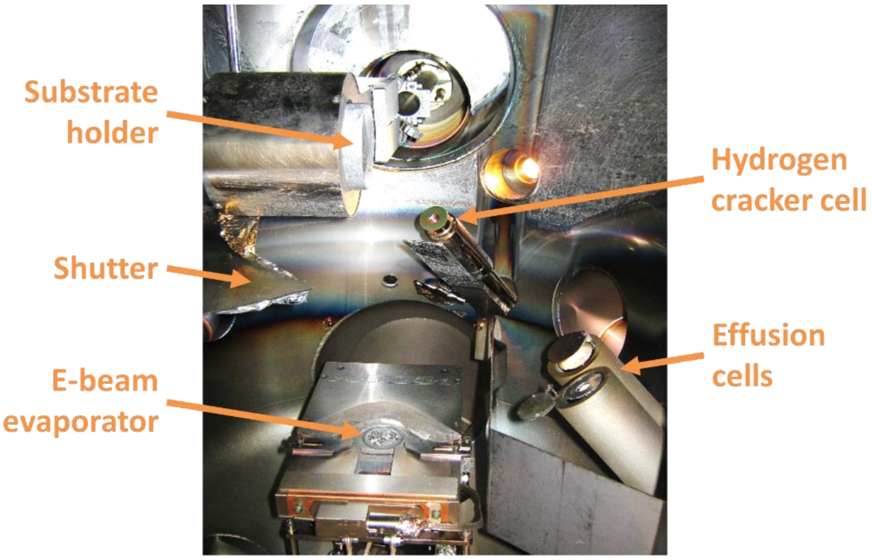

Figure 3.1: View into the e-beam chamber. The important parts are labeled. The substrate holder is in the transfer-position (pointing to the load-lock chamber).

Evaporating materials with a high melting point (as Mo) leads to massive heat radiation from the evaporator (see Figure 3.2). At an evaporation voltage of 7000 kV and a beam current of ~ 300 mA, approximately 2 kW of energy are transferred to the deposition chamber. This causes a heating of the chamber itself and, consequently, after some time an increase of the residual gas pressure, as more gas is released by the chamber's inner surfaces. Additionally, the differentially pumped rubber seals of the front door and the manipulator feedthrough are temperature sensitive. In order to circumvent this problem, a massive air cooling was added to the chamber. The 'Active Chamber Cooling System' (ACCS) consists of four large electric fans, pointing on the sidewalls of the chamber and two smaller fans, cooling the bottom of the chamber. The total airflow of the system is around 0.8 m^3/s. This system is attached for long deposition times of the respective materials and detached for the bake-out procedure.

A problem often encountered in thin film deposition systems is the calibration of the substrate temperature. The thermocouple (TC) that is used to regulate the heating power is located a few millimeters behind the substrate holder and can therefore not be expected to provide the actual substrate temperature. At lower substrate temperatures (< 300 °C), temperature calibration was done using a second k-type TC, clamped to the sample holder. At higher temperatures, the relation between the temperature measured by this TC and the applied heating power becomes strongly non-linear. A probable explanation can be found in the increasing heat transfer through the TC wires that lose more energy due to intensified thermal radiation. A second possible method to measure substrate temperature is using an infrared thermometer (pyrometer). As the emissivity of the substrate holder is unknown, the procedure proposed by Mizutani was used [35]. A large piece of silicon

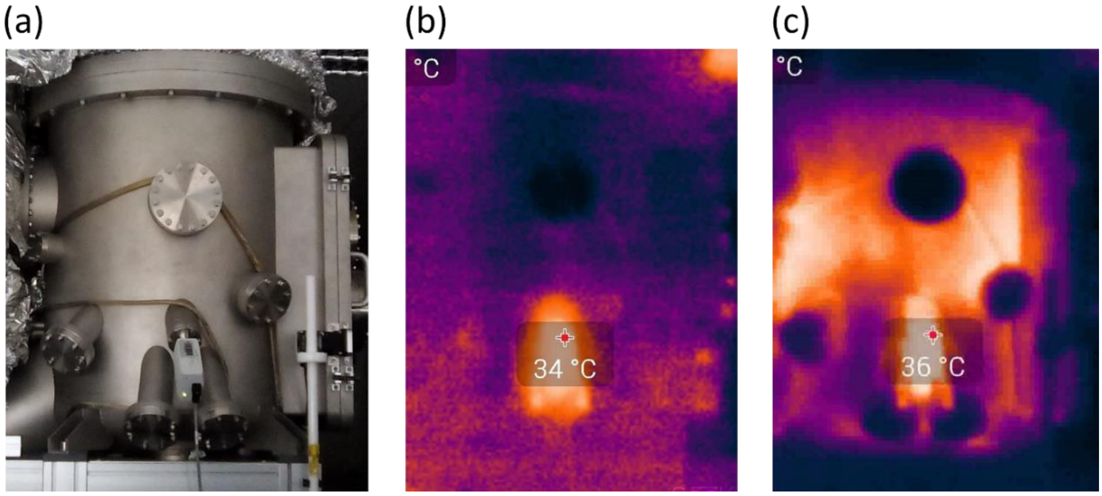

Figure 3.2: (**a**) Photo of the chamber. The front door is on the right side of the image. (**b**) IR image of the chamber before deposition. The hot spot is the vacuum gauge. Since it has a plastic housing and the IR camera does not consider different emissivity values, it is shown as the warmest spot in all images. (**c**) IR image of the chamber after 5 minutes evaporation of Mo. Wall temperatures above 100 °C are reached after long depositions without external cooling.

wafer is glued onto the sample holder. Inside the vacuum chamber, 500 nm silicon, followed by 100 nm aluminum are deposited onto the silicon substrate. The temperature of the sample is increased step-wise and the temperatures of the heater TC T_{Heater} and the pyrometer T_{Pyro} are logged. When a specific temperature is exceeded – the eutectic point of the Al-Si-system – both components rapidly form an alloy, causing a massive change of the emissivity. As a result, a jump of T_{Pyro} as well as a change of slope is obtained. As the temperature of this alloy formation is well known (577 °C [36]), a fixed point of the temperature scale exists. The formation of the Al-Si alloy was observed at $T_{\mathrm{Heater}} \approx 515$ °C (see Figure 3.3 **a**), which consequently can be identified with a real surface temperature of 577 °C. Between $T_{\mathrm{Heater}} = 300$ °C and 515 °C the real temperatures were interpolated linearly and for temperatures above 515 °C extrapolated in the same way. For temperatures below 300 °C, the calibration obtained by the clamped TC is used. Figure 3.3 **b** shows the finally used temperature calibration. All temperatures, given in this thesis refer to that.

Despite the substrate temperature, the shape of the particle beam, called beam divergence, is important for oblique deposition. This property is mainly influence by two parameters. Firstly, the scattering probability at the residual gas in the chamber and secondly, the geometric arrangement of the crucible and substrate to each other.

Let the divergence Ψ be defined as the maximum deviation of the particle flux around the mean value θ_{mean} so that the incidence angles θ_i of all incoming particles follow $\theta_{\mathrm{mean}} - \Psi/2 < \theta_i < \theta_{\mathrm{mean}} + \Psi/2$. The geometric part of Ψ is caused by the diameter of the

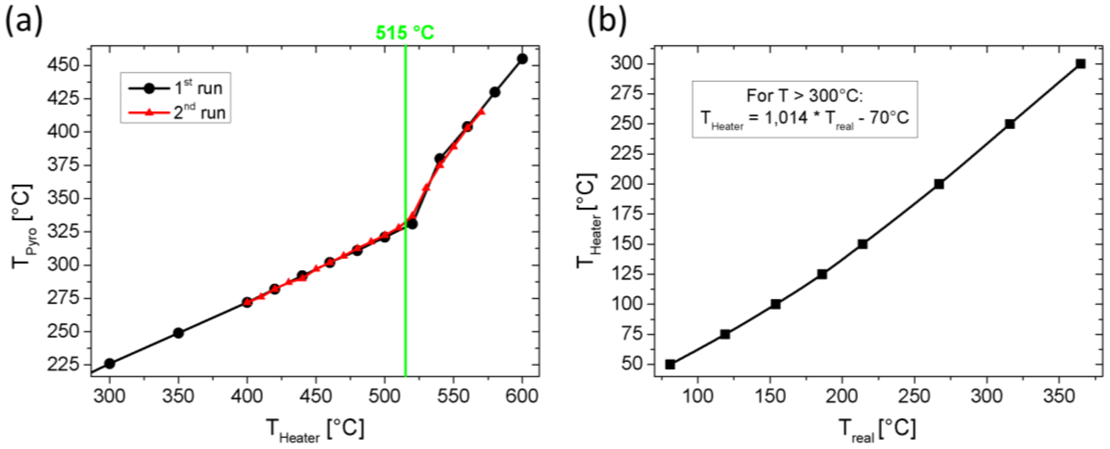

Figure 3.3: (**a**) Temperature measured by the pyrometer vs. temperature setting of the heater. Two different samples were used; the second run had smaller step width. At the beginning of the change of slope, the eutectic Al-Si alloy forms. (**b**) Final temperature calibration curve of the heater.

molten spot in the crucible and can be calculated to be $\Psi = 2\ \tan(d/(2a))$, with a denoting the distance of the substrate to the crucible and d being the diameter of the molten material spot in the crucible (size of the particle source). With a = 30 cm and $d \approx$ 1 cm (depending on the used material and heating power), one yields 1.9° as the maximum divergence angle. A general calculation of the actual distribution of the flux components in the divergence range is not possible. Even if the emission distribution at an isolated point of the surface of the molten material would be known, the total surface of the melt usually shows a strong curvature depending on the used material. For example, the surface of the molten spot is aprixmately flat for Ge, convexly curved for Si, concavely curved for Ti and completely irregularly shaped for Cr (which sublimes, rather than forming a melt).

The scattering probability can be estimated from the mean free path at the respective pressure. Depending on the reactivity of the material that is evaporated, the chamber's working pressure is in the range from $5 \cdot 10^{-9}$ mbar (for Ti) to $2 \cdot 10^{-6}$ mbar (for Al). This corresponds to a mean free path of roughly 20 km to 50 m for thermalized nitrogen molecules at room temperature. One may argue that the pressure directly over the crucible is higher, since the gas above the hot and molten material is denser, but in the case of evaporation into a vacuum, classical equilibrium thermodynamics is not valid. All the emitted particles have velocity vectors pointing into the same hemisphere. Consequently, in the center-of-mass frame, the relative velocities of the particles are lower than in the thermalized equilibrium, strongly decreasing the chance of particle-particle collisions. Another factor, reducing the influence of possible collision events above the crucible is that the vapor expands into the chamber. Thus, most of the assumed collision events would occur directly above the crucible, where they would not lead to a strong enhancement of the geometric beam divergence at the position of the substrate.

As this included macro editor does not allow loops, periodic movements (as sweeping *Φ*) are difficult to realize. Therefore, the data format of the macro files was decrypted so that macros requiring periodic movements can be prepared externally.

3.1.2 Liquid nitrogen cooled sample holder

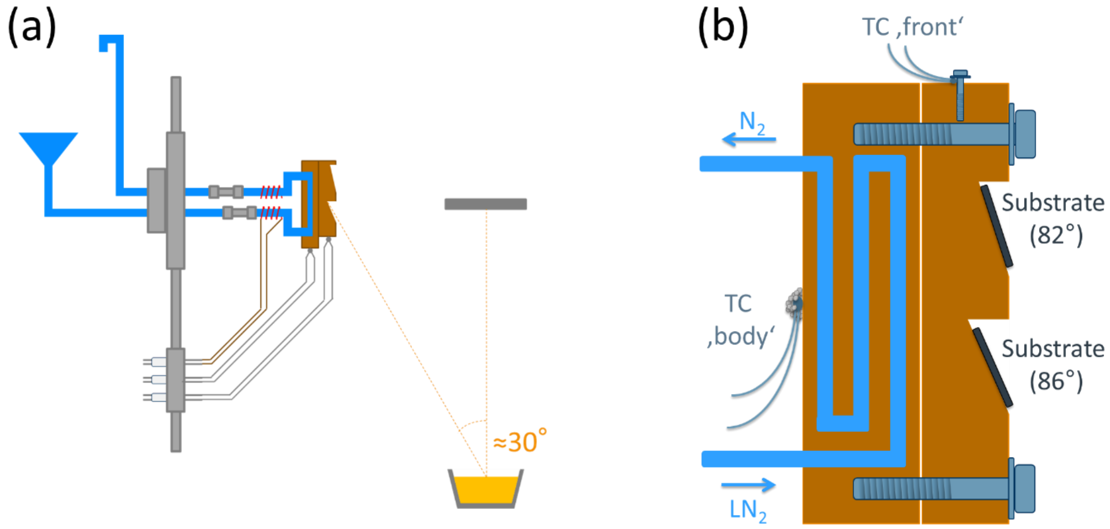

Figure 3.4: (**a**) Schematic illustration of the liquid nitrogen cooled sample holder (‘LNSH’). Blue are the nitrogen tubes, orange the two copper blocks. Two pairs of thermocouple wires and a (not used) pair of heater wires are provided by a feedthrough. The relative angle of incidence at the position of the LNSH is 60°, as shown. (**b**) Detailed drawing of the ‘body’ and ‘front’ copper blocks, as described in the text.

The GLAD process is influenced significantly by surface diffusion. The normal, build-in, sample holder allows heating of the substrate from room temperature up to 850 °C, which is accompanied by an increase of surface diffusion. Reducing surface diffusion requires a cooling system. For this purpose, a liquid nitrogen cooled sample holder has been developed (‘LNSH’, see Figure 3.4). As the main design-criterion was a reproducible, as low as possible, temperature, the ability to rotate the substrate is omitted. This allows a construction that maximizes the heat transfer. The LNSH is composed of two parts (see Figure 3.4 **b**). The first one (‘body’) is a copper block, to which holes have been drilled so that a continuous path for flowing liquid nitrogen through it is created. The penetrations to the outside are closed by soldering. Two copper tubes are soldered onto the block to connect the inner flow path to a CF feedthrough via Swagelok connectors. On the out-(air-)side of the feedthrough a reservoir is connected to the inlet and a bended tube is connected to the outlet. The outlet tube allows the escaping liquid nitrogen to evaporate. Additionally, gaseous room temperature nitrogen can be applied backwards to the system to reduce the warm-up time. The body-block has five holes (Figure 3.5 **b**), equipped with steel threads to enable a strong mechanical (and thereby also thermal) connection to the actual sample holder. This sample holder (‘front’) is a second copper block with holes according to the one in the body-block, enabling to connect both with usual steel screws. Into this front-block, five steps are face milled. This is done so that differently tilted ground-planes are achieved, which finally hold the samples (see Figure 3.4 **a** and Figure 3.5 **a**). The tilted ground-planes realize vapor incidence angles of 86°, 82°, 78°, 74° and 0°. Furthermore, an angle of 60° can be achieved by gluing a sample onto a flat part of the front-block. The samples are glued using a carbon paste, which is allowed to dry at air for at least two hours and then hardened during chamber bake-out at approx. 93°C. A drawback is that the deposition chamber has to be vented to attach the front-block with the sample to the body-block.

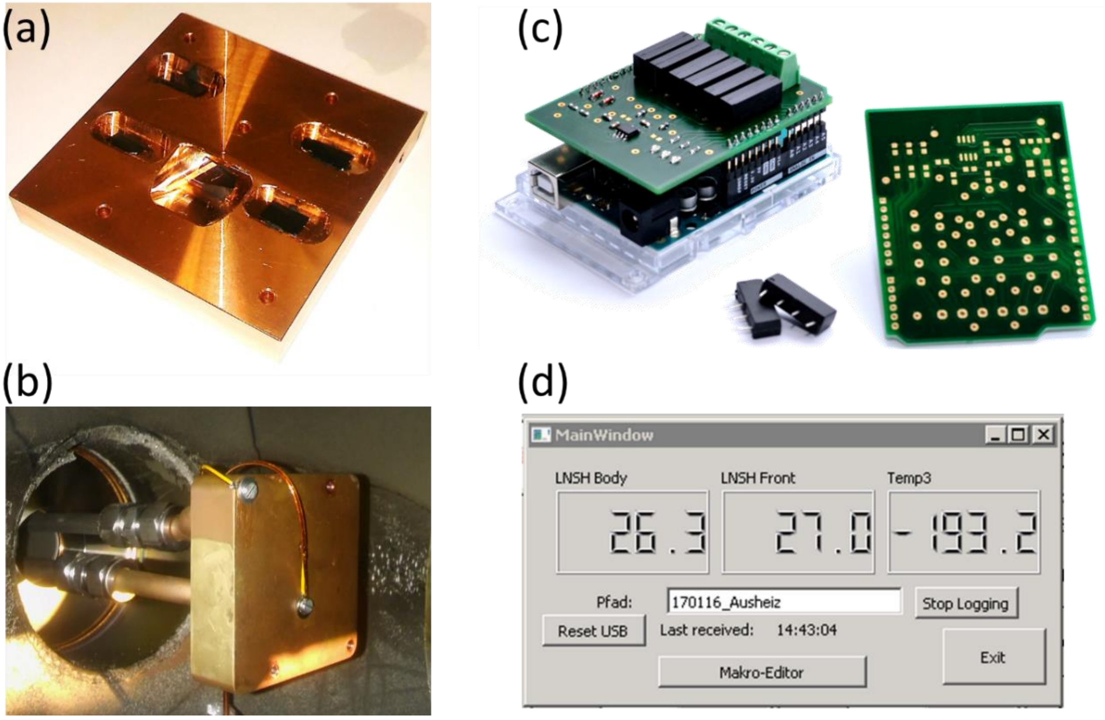

LNSH Body: 26.3
LNSH Front: 27.0
Temp3: -193.2
Pfad: 170116_Ausheiz
Last received: 14:43:04

Figure 3.5: (**a**) Image of the front-block, with samples attached. (**b**) Image of the body-block, with both thermocouples attached to the contact plane to the front-block (from the first cooling experiment). (**c**) Image of the custom temperature measurement system. Right without and left with electronic components soldered. The left images also shows the unit attached to an Arduino Uno. (**d**) Screenshot of the temperature display on the PC, programmed in C++ with Qt.

To ensure that the front and the body copper blocks have the same temperature, two k-type thermocouples (TCs) were attached to the LNSH. The first one is permanently glued by a high-performance silver paste onto the backside of the body-block. The second one if pressed to the front-block by a screw. The direct contact of both TCs ensures a good thermal conductance and hence a reliable temperature read. As both TCs now are electrically connected, a special read-out device is required (see Appendix A for circuit diagram and PCB layout, for a photo see Figure 3.5 **c**). This was realized by utilizing a MAX31855 IC that allows temperature measurements of a k-type TC with a resolution of 0.25 K. This chip includes a cold-junction compensation (what in this case is rather a hot-junction compensation) and is stated to provide an accuracy better than 1 K. The IC communicates with an Atmel AVR ATmega328 microcontroller (“uC”), located on an Arduino Uno board, via a Serial Peripheral Interface (SPI) protocol. Between the TC wires and the MAX31855, reed-relays are placed allowing to disconnect each TC wire completely. If both contacts of one TC are disconnected, the only way the thermo-electric current of the other TC to flow for is through the MAX31855, where it can be measured. Three distinct channels – using six reed-relays – are realized. The relays are also controlled individually by the uC. Two of the channels are connected via a TC feedthrough with the TCs at the body- and the front-block inside the vacuum chamber. The third channel can be connected to any other TC and was used for calibration (e.g., by dipping into liquid nitrogen) or it was clamped to the nitrogen outlet. The measured temperatures were transferred from the uC to the controlling PC via a serial connection over USB.

It should be mentioned that the thermo-electric voltage of k-type thermocouples is not linear to the temperature difference at such low temperatures. The MAX31855 does not take this into account. To compensate this, the outputted temperatures are conversed reversely to yield the thermo-electric voltage by the conversion constant 41.276 µV/K, given in the datasheet of the MAX31855 [37]. Then, the voltage is conversed back to the temperature by the relation provided by the NIST [38]. As this is a polynomial of eighth degree, this is done at the PC (as the uC runs at 16 MHz and has no built-in floating-point-math-unit). All of the components were placed on a 2-layer printed circuit board (PCB) that was designed to fit on an Arduino Uno board. A low pass filter was added into each TC channel to reduce the measurement noise during operation of the high-voltage power supply for the electron beam evaporator. During operation, some noise is still present, probably due to bombardment of die LNSH with stray electrons or ionized material atoms, leading to an underlying current, which is not correlated to the temperature measurement. The conversed temperatures are displayed on the PC by a simple C++/Qt software that allows logging of the temperature during the process (Figure 3.5 **d**). Calibration of the temperatures, given by the TCs, is done by dipping the third TC into liquid nitrogen and a water-ice-mixture. A calibration factor of around 1.0087 was necessary to obtain the expected temperatures and is considered directly in the software. Additionally, the software provides access to the above mentioned macro-editor expansion that allows realization of macros with periodic process steps.

The LNSH is cooled down by filling the reservoir with liquid nitrogen. Due to the geometry of the construction, the liquid nitrogen flows into the body-block, cooling it down to nearly 77 K in approximately 20 minutes. Temperature difference between body- and front-block typically stayed below 2 K. This difference vanished within seconds, after the minimum is reached, indicating a very good thermal contact of both blocks.

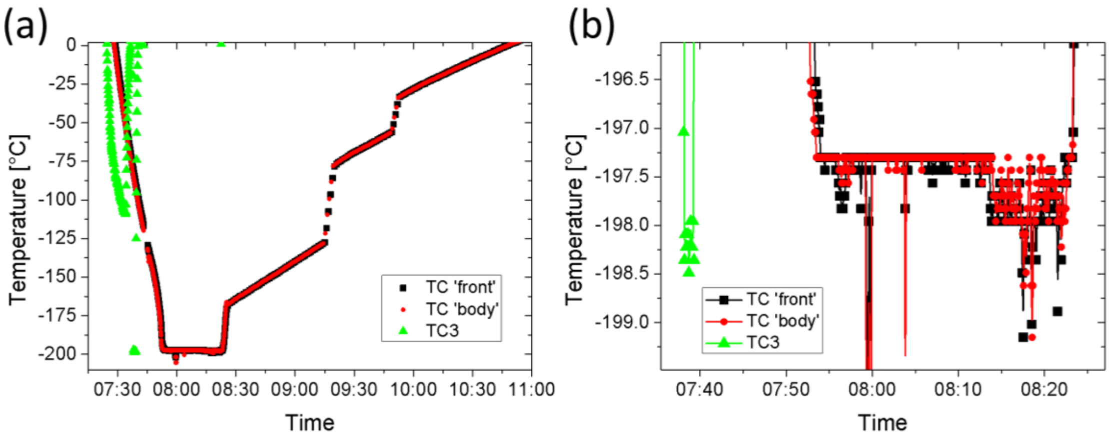

Figure 3.6: (**a**) Temperature over time for a typical sample deposition. TC3 was dipped directly into liquid nitrogen as a validation. During the warm-up, gaseous nitrogen was allowed to flow backwards to the system, speeding up the temperature rise. The times with the lower slope show the slow natural temperature rate of rise. (**b**) Detail of the low-temperature period. After the evaporator was activated at around 08:14, neither a temperature rise, nor a considerable difference between both TCs is detectible.

The continuously evaporating nitrogen escapes to the other tube to the environment. When the base temperature is reached on both copper blocks (indicated by both TCs), the system is allowed to equilibrate for around 10 minutes. Then, the deposition is started. After deposition, gaseous nitrogen is allowed to flow through the LNSH in the reversed direction to speed up the heating process (that would otherwise take around 6 hours). The chamber is opened when the temperature has risen surely over the dew-point of the environment (typically 15 °C is assumed as a save value) and then the samples are removed.

Notice, that before cooling down, an adequate vacuum should be achieved to avoid condensation of water vapor on the LNSH and the attached samples. Thus, a bake-out step is usually required, which is also used to harden the carbon glue. The presented LNSH is used in this thesis mainly for the deposition of Si and Ge, but also applied for the growth of metal nanostructures by Liedtke *et al.* [39] as well.

3.1.3 Ion beam sputter chamber

Especially for industrial applications, electron beam evaporation is of minor relevance, due to the high vacuum requirements and limitations in the coverable area. Typically, sputtering techniques are the method of choice for non-scientific usage. Various sputtering techniques exist, such as magnetron or DC sputtering. In these methods, the plasma that provides the ions, exists directly above the target. Therefore, the sputtered particles have to pass through a zone with an increased pressure and density. This leads to an increased collision rate of the sputtered particles with the plasma species and molecules from the residual gas. Consequently, a fraction of the particles becomes scattered and loses the initial trajectory. The arising randomly arriving particles are disturbing for a controllable GLAD growth [40, 41].

A sputtering technique that circumvents this is direct ion beam sputtering (IBS). Hereby, the plasma exists in a spatially separated plasma chamber. A grid system extracts the ions from the plasma and accelerates them towards the target. The plasma chamber and the extraction system form an ion beam source and the technique is known as ion beam sputter deposition (IBSD). In the used vacuum chamber, a RF coupled ion source working at 13.56 MHz is utilized. An argon flow of 3.5 sccm and a RF power of 95 W are used to create the plasma. With an acceleration voltage of 900 V, a beam current of typically 32 mA is achieved. Further technical details of the ion beam source can be found in reference [42].

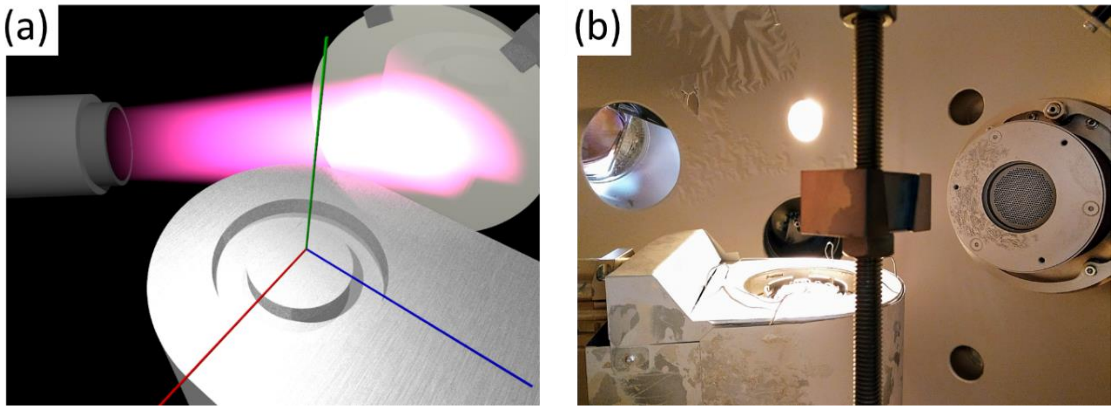

Figure 3.7: (**a**) Simulation of the beam path in the IBS chamber. If the substrate holder, the ion beam source, and the target are in the same horizontal plane, a part of the ion beam is blocked by the substrate manipulator, as can be seen in the lower right corner of the target. (**b**) Photography into the re-designed system. In the front, the target holder (without attached targets) can be seen. On the right side resides the ion beam source. The substrate manipulator is located 5 cm below the ion-source-target-plane to give the beam free path to the target.

In the deposition system, the argon ions hit an earthed 6-inch target at an angle of 45°, located approximately 17 cm away from the extraction grid system. Two targets are mounted in the system and can be chosen by a rotation feedthrough. The substrate is located at a distance of approximately 18 cm to the target. Care has to be taken that the substrate manipulator does not interact with the primary ion beam (compare Figure 3.7 **a**), what would cause increased substrate heating and increased contaminations due to parasitic sputtering as well. This occurred in the initially used deposition system, what finally lead to the decision to recreate the whole vacuum chamber. To overcome this problem, the target and the ion beam source are raised by 5 cm above the sample holder plane in the newly brought chamber. This avoids hitting the manipulator with the primary ion beam (see Figure 3.7 **b**). Moreover, the distance between the ion beam source and the target can be changed, allowing to optimize the size of the sputter beam at the target.

Comparable to the e-beam chamber, the system is equipped with a load-lock chamber for a fast sample transfer. Both chambers of the IBS system utilize turbomolecular pumps, backed by a roots-pump (deposition chamber) and a scroll pump (load-lock chamber). A base pressure of around 10^{-7} mbar and a working pressure of approx. $2 \cdot 10^{-4}$ mbar can be obtained.

The original software for controlling the substrate rotation required Windows NT and could not be adopted to run under more recent Windows versions (due to a direct processor interrupt call to load the commands into the motor control PCI-card). To enable an extensive computer control, a few hardware additions were necessary. This includes the replacement of the old stepper-motor control PCI-card with an Arduino Uno equipped with a commercial motor shield. This Arduino ('motor-Arduino') also controls a newly installed electro-pneumatic valve in the primary argon supply of the ion beam source. A second Arduino Uno ('ion-Arduino') is connected to the analog outputs of the ion beam power supply and the high voltage generators. It allows to measure the actual values of the provided ('forward') and reflected RF power, the acceleration voltage and the resulting current as well as the voltage and the current of the extraction grid. Furthermore, the ion-Arduino has the ability to switch the power supplies on and off and additionally can control the acceleration voltage by passing a low-pass filtered pulse-width-modulation (PWM) to the beam voltage supply. Finally, a custom designed readout unit evaluates the vacuum gauges of the system. Despite being from different companies, both full-range gauges of the deposition and load-lock chamber require a supply voltage of 24 V and deliver the pressure logarithmic on a 0 – 10 V analog output. The developed device provides four channels with 24 V power supply and the ability to measure 0 – 10 V with a resolution of 16 bit (based on a TI ADS1115 IC). Data from the ADS1115 are transferred to an Arduino Nano ('vacuum-Arduino') via an I²C bus. The Arduino converses the voltages to pressures, utilizing the conversion constants provided by the respective data sheets. The pressures are shown directly on a LCD, and send to the PC via RS232, which provides a more stable connection than USB (as used by the other devices). The circuit diagram and PCB layout are presented in Appendix B. A self-written C++ firmware runs on all three Arduino's to allow them to fulfill their respective purposes. Furthermore, a proprietary communication protocol is used to send data to the PC and to receive commands. Due to the existence of the Arduino bootloader, the firmware of all Arduino's can directly be changed from the PC.

The entire information of the system is gathered and displayed by a self-written C++/Qt software (shown in Figure 3.8). The software checks the status of the plasma and the ion beam from the acquired data and has the ability to stop the deposition, if a problem occurs. If the plasma vanishes from non-critical failures, the system attempts to restart

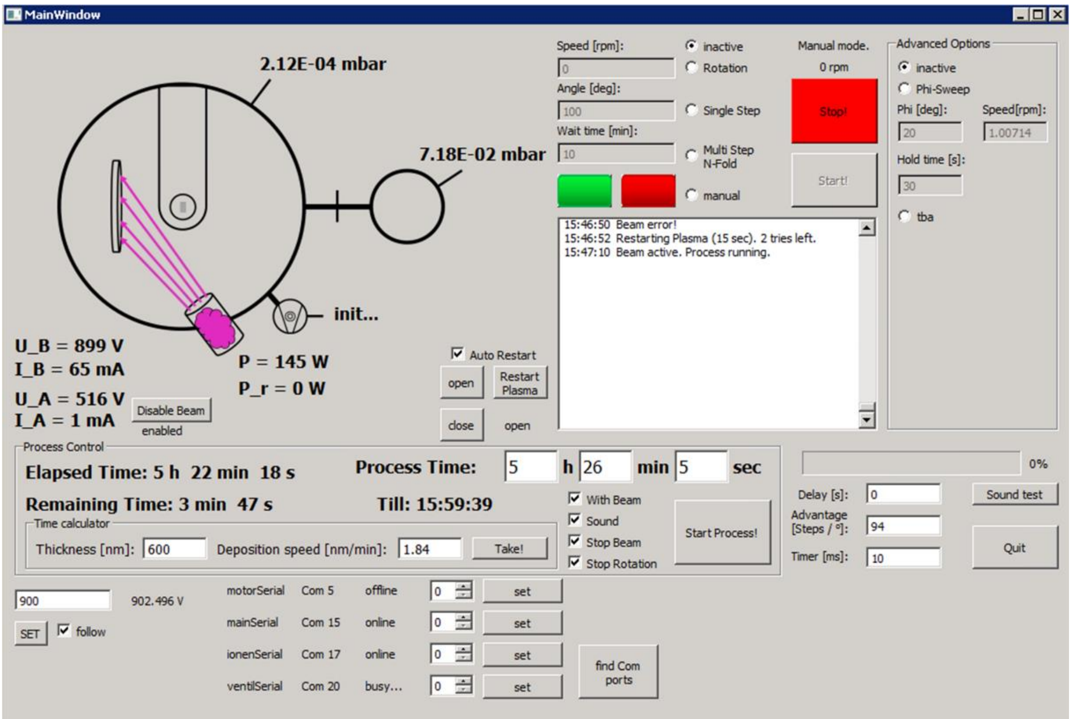

```
2.12E-04 mbar
7.18E-02 mbar
U_B = 899 V
I_B = 65 mA
U_A = 516 V
I_A = 1 mA
P = 145 W
P_r = 0 W
enabled
open
0 rpm
Speed [rpm]: 0
Angle [deg]: 100
Wait time [min]: 10
● inactive
○ Rotation
○ Single Step
○ Multi Step N-Fold
○ manual
Advanced Options: ● inactive  ○ Phi-Sweep  ○ tba
Phi [deg]: 20   Speed[rpm]: 1.00714
Hold time [s]: 30

15:46:50 Beam error!
15:46:52 Restarting Plasma (15 sec). 2 tries left.
15:47:10 Beam active. Process running.

Elapsed Time: 5 h  22 min  18 s
Process Time: 5 h 26 min 5 sec
Remaining Time: 3 min  47 s
Till: 15:59:39
Thickness [nm]: 600   Deposition speed [nm/min]: 1.84
☑ With Beam
☑ Sound
☑ Stop Beam
☑ Stop Rotation
0%
Delay [s]: 0
Advantage [Steps / °]: 94
Timer [ms]: 10

900    902.496 V
☑ follow
motorSerial   Com 5    offline   0
mainSerial    Com 15   online    0
ionenSerial   Com 17   online    0
ventilSerial  Com 20   busy...   0
```

Figure 3.8: Screenshot of the self-written control software. On the left side, the status of the system and the actual process is displayed. On the right side, the substrate rotation can be controlled. The bottom part shows some connection diagnostics that are going to be moved to a second window later. The same applies for the calibration data of the stepper motor and the alarm values of the system (yet hard-coded).

the plasma and the ion beam, by shortly closing the argon supply. After a pre-set time, the valve is opened again, and the rapidly increasing pressure enables the plasma to re-ignite. This procedure is repeated three times with increasing interrupt times. If this procedure fails or another critical error appears, an acoustic warning starts. The software allows to control the substrate rotation (including stepped rotation and phi-sweep techniques) as well. All information of the actual system and process status are displayed graphically. The state of the plasma and the beam is indicated by color changes of the respective parts in the schematic, to ensure a fast detection of possible errors.

Still, the substrate tilt angle has to be controlled manually, so that automation of the system is not finished yet.

The IBSD system was mainly used to deposit silver for plasmonic sensing applications, but also provided the possibility to compare the morphology of evolving silicon nanostructures with the e-beam deposition.

3.1.4 Nanosphere lithography

In order to create pre-patterned substrates on large scales, different lithography methods were developed in the past. Photo lithography [43], de-wetting [44] or patterning with block copolymers [45] are just a few examples of techniques that have been used to produce templates for GLAD. However, due to its experimental simplicity, the nanosphere lithography (NSL) technique is used in this thesis. With this method [46-48], templates can be produced on silicon and glass substrates. For this purpose, a hexagonally close packed (hcp) monolayer of polystyrene spheres (PSS) is immobilized atop the respective substrate. Onto the monolayer material is deposited by an evaporation technique. Part of the material passes through the gaps between the spheres, forming hillock-like seed points. These hillocks form a honeycomb arrangement, following the gaps between the PSS. If a second layer of PSS is deposited atop the first layer, the half of the previously open gaps is blocked, so that the final arrangement of the hillocks will be hcp, too. After deposition of the material, the substrates are immersed in tetra-hydro-furan (THF), dissolving the PSS. Subsequently, the substrates are cleaned in DI-water in an ultra-sonic cleaner. This cleaning procedure (THF, ultra-sonification) is repeated three times, to eliminate all remnants of the PSS and the material sticking to them. Finally, only the hillocks remain on the substrate, which can then be used for the GLAD process.

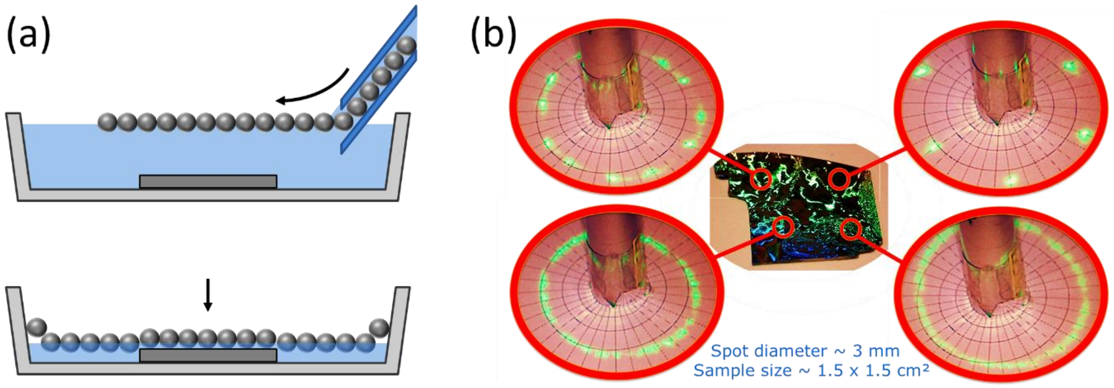

Figure 3.9: (**a**) Schematic illustration of the monolayer creation process and the subsequent transfer to the substrate. (**b**) Diffraction patterns of a NSL substrate (shown in the center) created by a green laser pointer. The distinct diffraction pattern of the top right image indicates a high quality of the monolayer at this position. The top left image shows two different orientations at this position, while the lower images indicate the existence of only very small ordered PSS domains.

Although various methods are proposed to achieve a highly ordered PSS monolayer, this crucial step is still challenging. For example, spin-coating is a fast and simple approach to obtain hcp arranged PSS on small domains. Large domains can be prepared by blade coating techniques with *in situ* control of the monolayer quality (density and order) [49]. As this kind of technique requires higher experimental effort, a compromise between achievable film area and experimental workload is provided by the following approach (adopted from [50], compare Figure 3.9 **a**). A commercially available PSS solution (10 $\%_{\text{wt.}}$ PSS dispersed in water) is mixed 1:1 with ethanol. Using an injection needle, a small amount of this mixture is applied slowly and carefully to the surface of DI-water in a petri-dish. The PSS spread out on the water surface, forming small ordered domains, which can visually be seen due to colorful interference effects. In contrast, diffuse white areas indicate that the spheres are not ordered on the entire interface. PSS are added to the water until approximately 80% of the water in the petri-dish are covered. If too many PSS are added, or if this is done too fast, the spheres penetrate into the sub-phase of the water, contaminating the substrate in the last process step. After applying the PSS, the monolayer can by crystallized further by creating gentle waves on the surface (by tilting the whole vessel). As a result, the domains grow, and the amorphous areas shrink. Subsequently, a very small amount of surfactant (e.g. Triton-X or sodium-dodecyl-sulfate (SDS)) is added to the water surface, by dipping a thin silver wire first into the surfactant and then touching the water surface. The molecules of the surfactant spread out on the water surface, thereby compressing the PSS, which then form hcp domains in the cm range. Compression of the monolayer leads to a reduction of coverage to approximately 50% of the area of the petri-dish. If too much surfactant is added, PSS might again penetrate into the sub-phase. After successful compression of the monolayer, substrate pieces are placed into the water (through the part of the petri-dish that is not covered by the PSS monolayer anymore). These substrates have been stored previously for at least 24 hours in a 10% solution of SDS, which makes their surface highly hydrophilic. The substrates are pushed beneath the monolayer and then the water is slowly drained out of the petri-dish using a pipette. When the water surface starts to bend at the edges of the substrates, draining is stopped. Finally, the last amount of water is allowed to evaporate slowly at room temperature, which takes around 12 hours until the substrates are dry. The hydrophilicity of the substrates avoids the formation of drops during the drying process so that the PSS monolayer can smoothly approach the substrate surface. After complete drying, the substrates are ready for the evaporation of the honeycomb hillock pattern.

The quality of the created monolayer can be assessed fast by using a green laser pointer and a paper screen (as illustrated in Figure 3.9 **b**). The diffraction patterns indicate the quality, orientation and domain-size of the PSS monolayer. Domain sizes of approximately 1 cm^2 can be obtained for large PSS (diameter = 1.59 μm), while with smaller spheres only smaller domains could be achieved. Further quality control is examined by scanning electron microscopy (SEM). Typical errors are too small or too large spheres, voids and sphere-triplets that are pushed out of the monolayer during drying [51] (see Figure 3.10). Dislocation lines appear as well.

A more detailed investigation of the deposition process, which follows the creation of the PSS monolayer on the substrates, can be found in section 5.4.2.

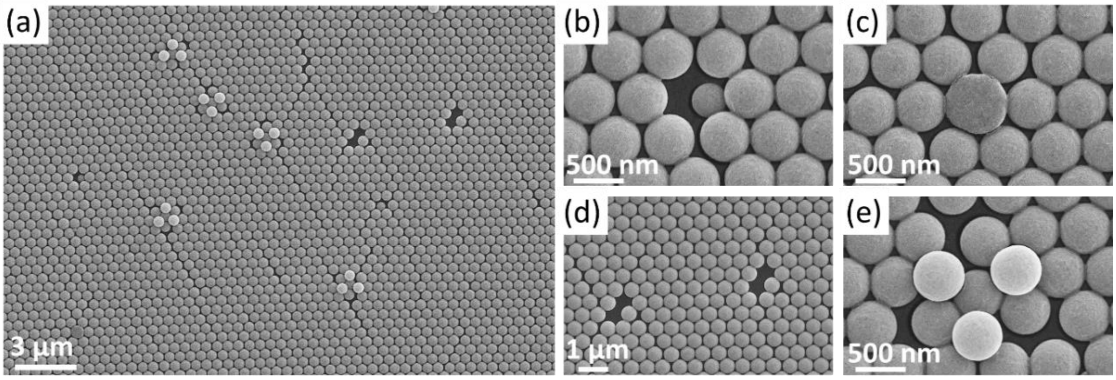

Figure 3.10: (**a**) SEM overview image, showing a large, highly ordered PSS domain with some defects. These defects can be point defects, as too small spheres (**b**), to large spheres (**c**), double-voids (**d**) and pushed out triplets (**e**). Moreover, line-defects such as dislocations can be observed.

3.2 Characterization techniques

3.2.1 Scanning electron microscopy

As the primary tool to investigate the morphology of the grown thin films served the scanning electron microscope (SEM). In a SEM, free electrons are typically produced by thermionic emission or field emission, subsequently accelerated to energies in the lower keV range, and finally focused by electro-magnetic lenses onto a sample surface. To avoid collisions of the electrons with gas atoms, high-vacuum conditions are required. The electrons that hit the sample interact with its surface, thereby leading to the emission of secondary electrons (SE), back-scattered electrons (BSE), and characteristic X-ray radiation.

SE are generated in a large interaction volume at the beam incidence point. However, as they have low kinetic energies (typically < 50 eV), only SE generated near the surface can escape out of the sample volume. This makes the SE to the primary choice if high magnifications shall be reached, providing a resolution in the range of 2 nm. The emitted SE are detected by an Everhart-Thornley detector. In this kind of detector, the SE are collected by a positively biased (and hence attracting) grid and afterwards accelerated onto a scintillator material. The created photons are transported via a glass fiber to a photo-multiplier located outside of the vacuum system. The signal is amplified further and then digitized by an analog-to-digital converter. This is the most often used mode in this thesis.

BSE have energies in the range of the primary electron beam and originate from a quite large sample volume. Compared to the SE, this leads to a low spatial resolution. This mode therefore is interesting only to provide contrast between different elements, as the back-scattering probability (and therewith the signal intensity) increases strongly with the atomic number. The BSE are measured by repelling the low-energy SE with a negatively charged grid in front of the detector.

The incident electron beam generates X-ray radiation as well. While the bremsstrahlung cannot be used for analysis, the characteristic radiation can be utilized to distinguish between different materials. As this characteristic X-rays radiation has its origin in the distinct energy levels of the valence electrons of the respective material, each material emits a unique energy spectrum. Thus, measuring this spectrum permits to determine the originating material. This technique is known as energy dispersive X-ray spectroscopy (EDX).

Other possible effects that could be used to analyze the sample further are, for example, Auger electron emission, electron beam induced current, cathodoluminescence, or electron-backscatter diffraction.

Finally, an image is created by scanning the electron beam over the surface and transferring the measured intensities into an x-y-array, correlating to the position of the electron beam.

An electron acceleration voltage of 8 kV was typically used. Cross-sectional images were taken by cleaving the substrates with the thin films on it. Images desired to measure thicknesses or angles were captured with a high scanning speed to avoid the influence of possible drift movements. Images for presentation were taken with higher integration times, to reduce signal noise. Image processing and measurements are done with the software ImageJ [52, 53].

3.2.2 X-ray reflectivity measurements

As a technique to determine the density of the deposited thin films, X-ray reflectivity measurements (XRR) were utilized. In this technique, the intensity of the specular reflectivity of X-rays is measured for small incidence angles. The measured reflectivity might be treated with the classical Fresnel theory. For this, the refractive index of the respective material in the wavelength region of X-rays is given by (following [54])

$$\tilde{n} = 1 - \delta + i\beta \, , \tag{3.2.1}$$

where δ denotes the dispersive part and β the absorption. Further

$$\delta = \frac{e^2 n_e}{2\varepsilon_0 m (2\pi c)^2} \lambda^2 = \frac{r_0 \lambda^2}{2\pi} n_e \tag{3.2.2}$$

gives an expression for the dispersion. Hereby, r_0 denotes the atomic radius and λ the X-ray wavelength. n_e denotes the electron density and can be expressed with the product of atomic number Z and the atom density n_{Atom}. For a better approximation, Z is often substituted by a complex atom form factor $\tilde{f} = Z + f' + if''$. Together one yields:

$$\delta = \frac{r_0\lambda^2}{2\pi}\,(Z + f')\,n_{Atom} \tag{3.2.3}$$

and

$$\beta = \frac{r_0\lambda^2}{2\pi}\,f''n_{Atom}\,. \tag{3.2.4}$$

Together with

$$n_{Atom} = \frac{N_A}{A}\,\rho \tag{3.2.5}$$

the density of the material can be determined from β and δ. ($N_A$denotes Avogadro's number and A the atomic weight.) Assuming the surface of a sample (so $n_{Air} = 1$) and a small incidence angle θ (yielding only a small interaction depth and therefore eliminating the absorption), one can find the critical angle of total reflection by

$$1 - \delta = \cos\theta_C \approx 1 - \frac{{\theta_C}^2}{2}\,, \tag{3.2.6}$$

yielding further

$$\theta_C \approx \sqrt{2\delta} = \sqrt{\frac{r_0\lambda^2}{\pi}N_A\frac{Z + f'}{A}\rho}\;. \tag{3.2.7}$$

This equation can be used to estimate the film density from the total reflection shoulder of the reflected intensity diagram. Anyway, a more accurate estimation of the density can be obtained, if the angle dependent reflectivity $R(Q)$ is fitted by a computer algorithm. With $R_F(Q)$ denoting Fresnel's reflectivity, $Q = 4\pi\sin\theta\,/\lambda$ and $\rho_e = \rho_e(z)$ denoting the depth dependent electron density distribution, the reflectivity is given by:

$$R(Q) = \left|\frac{1}{\rho_\infty}\int_{-\infty}^{\infty} e^{iQz}\frac{\mathrm{d}\rho_e}{\mathrm{d}z}\mathrm{d}z\right|^2 R_F(Q) \tag{3.2.8}$$

The parameters of this formula are varied by a suitable algorithm to fit the measured intensities, yielding an estimation of the surface near density of the sample. This is done here by the software MicronovaXRR [55].

The measurements were obtained by using Cu-K_α radiation with λ = 0.154056 nm. XRR allows also estimation of the film thickness and roughness, which was not used in this thesis.

3.2.3 Other Techniques

X-ray diffraction (XRD)

XRD was used to ensure a phase separation of gold and nickel in the electroplating experiments (section 7.3). In XRD, X-rays are directed onto the sample, where they interact with the crystalline material. Specific reflections appear if the Bragg condition is fulfilled. Varying the incidence angle of the X-rays results in diffraction on different crystal planes, allowing to determine the spacing of these planes. This permits the identification of different materials, phases, crystal orientations, strain, etc.

Cu-K_α radiation again was used for the measurements. Details of this technique can be found in [56, 57]

Resistivity measurements

Resistivity of doped amorphous silicon thin films was measured in an in-plane geometry utilizing evaporated metal contacts. These contacts were produced by shadow lithography, using polyimide masks that were cut out by a laser. The masks were pre-baked in air at 150 °C for at least one hour to remove any ad- and absorbed water. Then the masks are screwed to the normal sample holder of the e-beam chamber, where then the contacts are deposited by evaporation. The exact sample geometry is discussed later in section 7.1.

These metal areas are contacted by using spring loaded gold tips ("pogo pins"). A Keithley 2602A Source-Measure-Unit (SMU) was utilized to measure U-I-curves. This device provides an accuracy and resolution for sourcing and measurement of 5 µV and 1 pA. The measurements were performed in a dark environment on a temperature-controlled heat plate at (28 ± 1) °C. The sample currents never exceeded 1 mA.

Raman spectroscopy

To determine the crystallinity of the obliquely deposited silicon thin films, Raman spectroscopy was utilized. Raman scattering describes the inelastic scattering of photons on molecules or solids. When photons interact with such materials, there is a probability that a molecular oscillation is excited or, respectively, a phonon is created, consuming a part of the energy of the initial photon. As the energy of such oscillations / phonons is specific for the respective material, measuring the wavelength of the scattered photons allows to determine the bindings of the scattering material. In the experiments described in this thesis, phonons are created in silicon. In crystalline silicon, the energy of such phonons is defined very sharply by the nearly perfect atomic ordering of the silicon crystal. In amorphous silicon, no long-range order exists, so that phonons exhibit a broader energy distribution. This reflects in the measured spectrogram of the scattered light, where crystalline silicon shows sharp intensity peaks, whereas amorphous silicon shows a rather broad maximum.

Measurements were done using a 473 nm laser and an Olympus MPlan N 100x/0.90 objective in a commercial Raman spectrometer. To avoid crystallization of the amorphous material due to radiative laser heating, measurements were performed at different positions with the lowest possible laser intensity. Details of this technique may be found, e. g., in [58].

Secondary ion mass spectroscopy (SIMS)

Calibrating the boron flux of the high temperature effusion cell was performed by SIMS. Hereby, a primary gallium ion beam sputters the surface of the sample. The sputtered secondary ions are collected and analyzed by a mass spectrometer (a time-of-flight mass spectrometer in this case). A direct quantification of the observed sample composition is difficult, because the sputter yield depends on the chemical composition and various other parameters, as do the ionization probabilities of the sputtered atoms.

To ensure a reliable control and quantification of the boron concentration, the following procedure was used: A silicon film was deposited onto a commercial silicon wafer, with a known boron concentration. During deposition, growth speed was fixed at 0.1 nm/s. A boron profile was realized in this film by setting the boron effusion cell to four distinct temperatures for a fixed period of time (1000 s → 100 nm film thickness) each. Then the sample is analyzed by SIMS and the boron concentrations in the film are compared to the known concentration of the substrate, allowing to estimate the boron flux during growth.

Measurements were carried out with gallium ions for analysis and oxygen ions for depth sputtering. The fundamentals of this technique are presented, e. g., in [59].

4 Experimental results

In this chapter, the experimental observations that serve as the basis for later modelling and simulation are presented. Experimental processing aimed to alter specific properties, is summarized in chapter 7. Unless otherwise noted, all shown thin films were grown by electron beam evaporation without any substrate movement during growth.

4.1 Columnar structure and evolutionary selection

As already indicated in section 2.2, the columnar thin film morphology that is usually found for vertical deposition, is transformed to isolated, tilted nanostructures during oblique growth. This is caused by the self-shadowing effect. A difference between amorphous and crystalline material can be observed. Amorphous nanocolumns show a nearly constant diameter during growth and only a few of the columns stop to grow during the film evolution. After an initial nucleation or roughening step, the nuclei are either shadowed or they are not. As all the columns evolving from the non-shadowed nuclei show the same growth speed, no intrinsic competition mechanism exists. Changes in the shadowing condition can only appear due to statistical noise of the incoming particle flux. In Figure 4.1 **a** a SEM image of tilted Si columns is shown and in **b** the static shadowing conditions are illustrated.

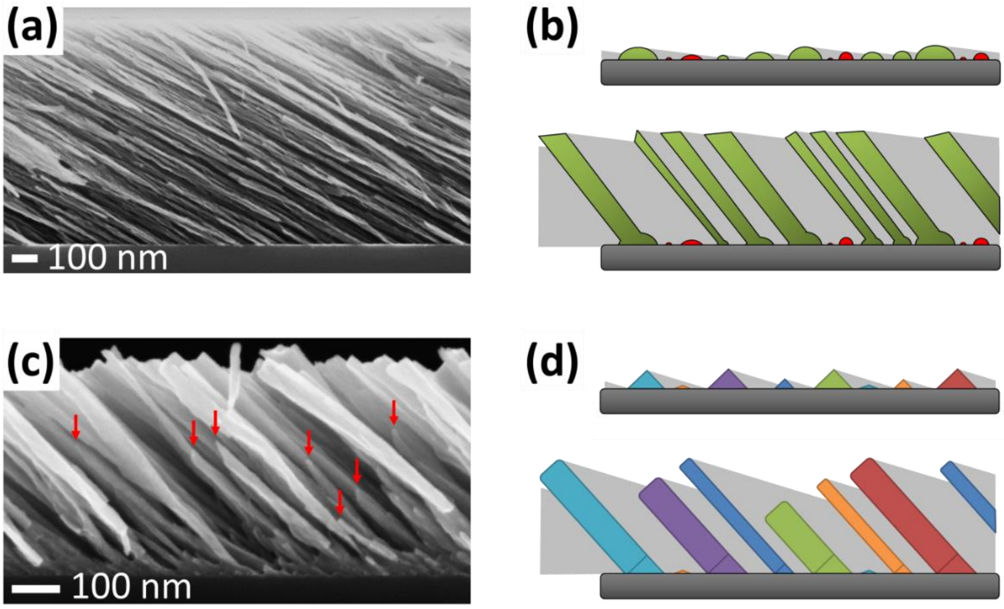

Figure 4.1: (**a**) and (**c**) respectively show SEM images of obliquely deposited Si and Mo films. Some structures that stop to grow are indicated with red arrows. (**b**) Schematic illustration of the film evolution of amorphous films. Columns that are not shadowed initially will continue to grow with the same speed and therefore will never become shadowed. (**d**) The growth speed of crystalline materials depends on the orientation of the crystallites (indicated by different colors) so that columns can also later become shadowed and therefore stop to grow.

In contrast, crystalline materials often exhibit a strong column broadening during growth and many of the columns stop to grow during the deposition process (e.g. [60, 61]). A possible explanation can be found in the randomness of the crystal orientation of the initially formed nuclei. Differently oriented crystallites show different growth directions and growth speeds. Thus, slower growing columns eventually become shadowed and consequently stop their growth. Because there are fewer developing nanostructures per unit area as the growth process proceeds, the shadows of the 'surviving' structures become longer and material can penetrate deeper into the evolving film, leading to a broadening of the remaining columns. Figure 4.1 **c** depicts a SEM image of tilted Mo columns and in **d** the selection of fastest growing crystallites is illustrated. Liedtke *et al.* have found that the tilted Mo columns are single crystalline and show an evolution from randomly oriented to highly biaxial textured during growth [39, 62]. This confirms the evolutionary crystallite selection, predicted by van der Drift [22].

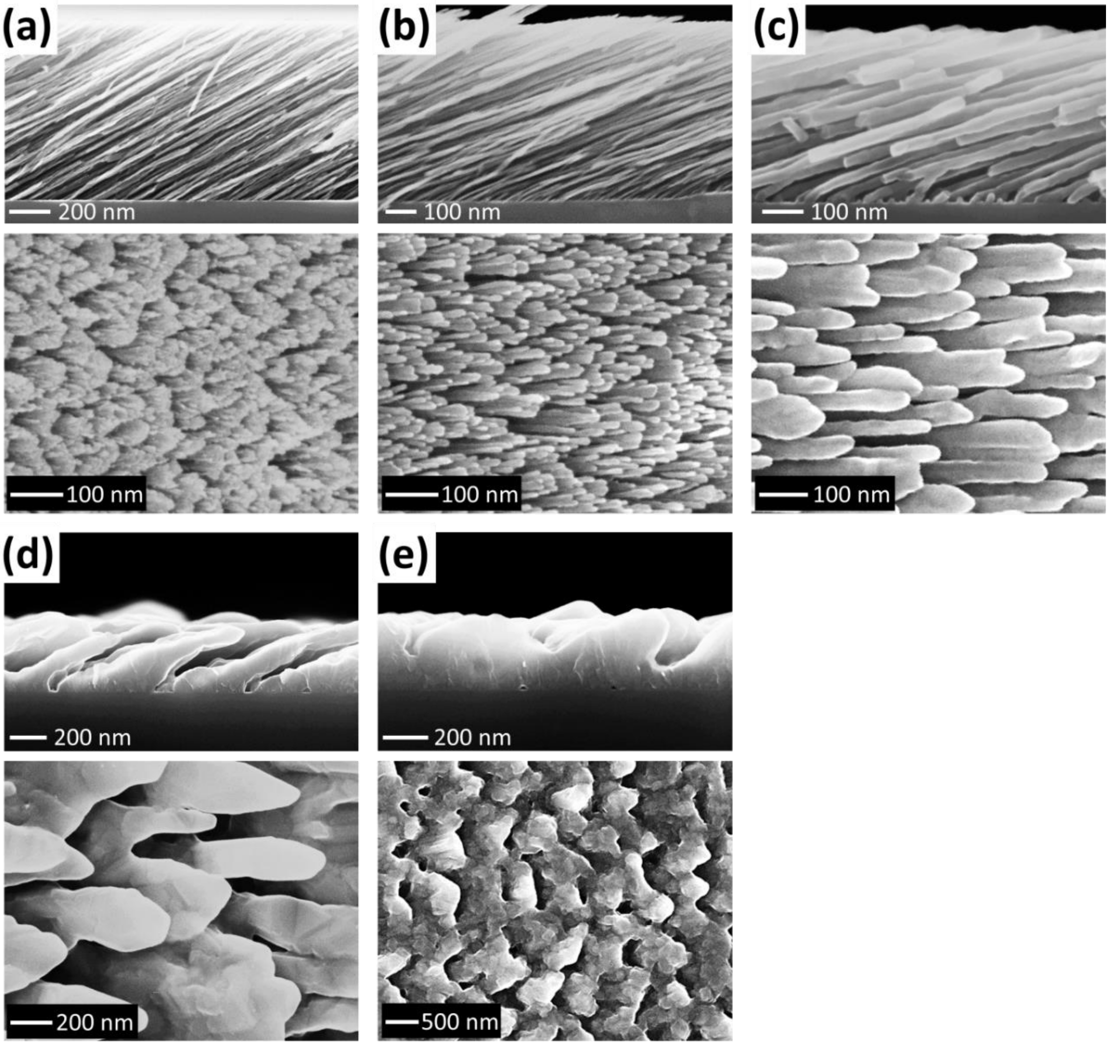

Figure 4.2: Side- and top-view SEM images of obliquely (θ = 84°) deposited Si films. Deposition temperatures were (**a**) RT, (**b**) 300 °C, (**c**) 500 °C, (**d**) 700 °C, and (**e**) 750 °C.

Besides the kind of deposited material, the deposition conditions play an important role in the morphology evolution. Figure 4.2 shows Si films, deposited at $\theta = 84°$ at varying temperatures from room temperature (RT) up to 750 °C. Three main observations can be made: With increasing temperature (i) the growth speed (and by this the final film thickness) decreases, (ii) the tilt angle increases, and (iii) the structure diameter increases. Isolated nanostructures could not be observed on samples deposited at 750 °C, but a significant porosity is still obvious. The increased diameter can be explained by the dynamics of the first nucleation step of column growth. For the column formation to start, it can be expected that the shadow lengths have to be larger than the surface diffusion lengths. This is the case, when the height of the nuclei becomes large enough. As higher temperature leads to larger diffusion lengths, the nuclei are larger at the time point when shadowing starts to dominate the growth process so that the diameter of the evolving structures is also increased.

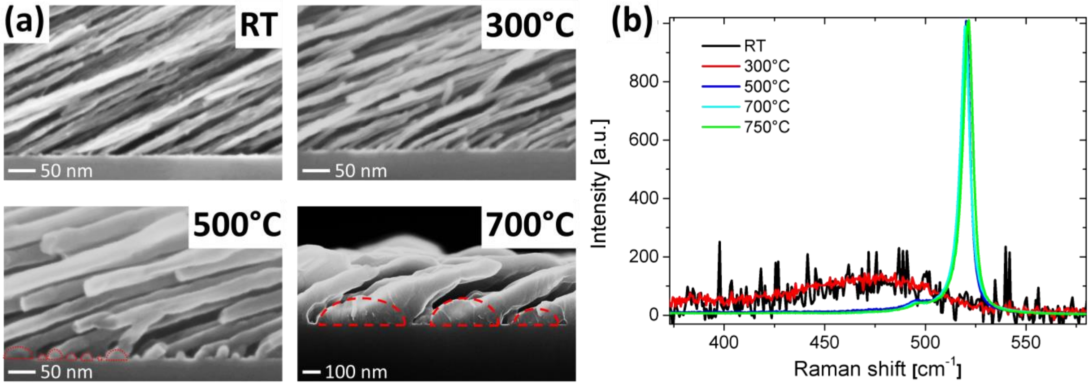

Figure 4.3: (**a**) Magnified SEM images of the substrate-structure interface for deposition at different temperatures. (**b**) Raman spectrum of Si on sapphire substrates, obliquely deposited at different temperatures, proving that the Si nanostructures are crystalline, when deposited at 500 °C and above.

In Figure 4.3 **a** high magnification SEM images of the initial growth step are shown. For the higher temperatures, the nuclei are indicated. It should be pointed out that the structure diameters of the 500 °C samples remain approximately constant during the complete growth process, in contrast to the previously shown Mo samples. This is not expected, as the Si structures are also crystalline at this temperature, which is confirmed by Raman spectroscopy (Figure 4.3 **b**).

The dynamics of the growth process can be observed in the shadows of dust particles on the sample. The particles have diameters above 1 µm and can be found on nearly all samples. These particles cast long shadows on the sample surface. Since the diameter of the particles increases during the growth process, the column evolution can be observed at the edge of the therefore as well growing shadows. Figure 4.4 shows top-view SEM images of this zone as well as 2D Fourier transformations (FFT) of the indicated areas in the nucleation zone. For the room temperature sample (**a**) shadowing acts right from the beginning, as the non-circular FFT pattern indicates. Before the nuclei develop into the actual columnar nanostructures, an orientation of the distribution of the nuclei perpendicular to the incident flux can be observed. This can be explained by the fact that shadowing does not impede the nucleation on the sides (with respect to the incoming particle beam) of the shadow casting grain. The described effect can be used to tune the direction of the magnetic easy-axis, if a very thin film (~ 2 nm) of a magnetic material (as Fe, NiFe or CoFeB) is deposited obliquely at room temperature [63, 64]. In this case, the magnetic easy-axis lies perpendicular to the incident flux. At higher temperatures, all FFTs show a full circular pattern, indicating a randomly distributed nucleation that is not influenced by shadowing. The transition from this random nucleation to the shadowing dominated growth occurs more abrupt as the temperature increases. At the highest temperature (750 °C), nucleation shows clear signs of beginning epitaxy on the natively oxidized Si(100) substrate. But still at this temperature, shadowing acts as soon as the film roughness becomes high enough. In this case, at first a nearly closed film grows (compare Figure 4.2 **e**), but then large voids appear. It can be assumed that, if film thickness is chosen large enough, isolated structures could be observed.

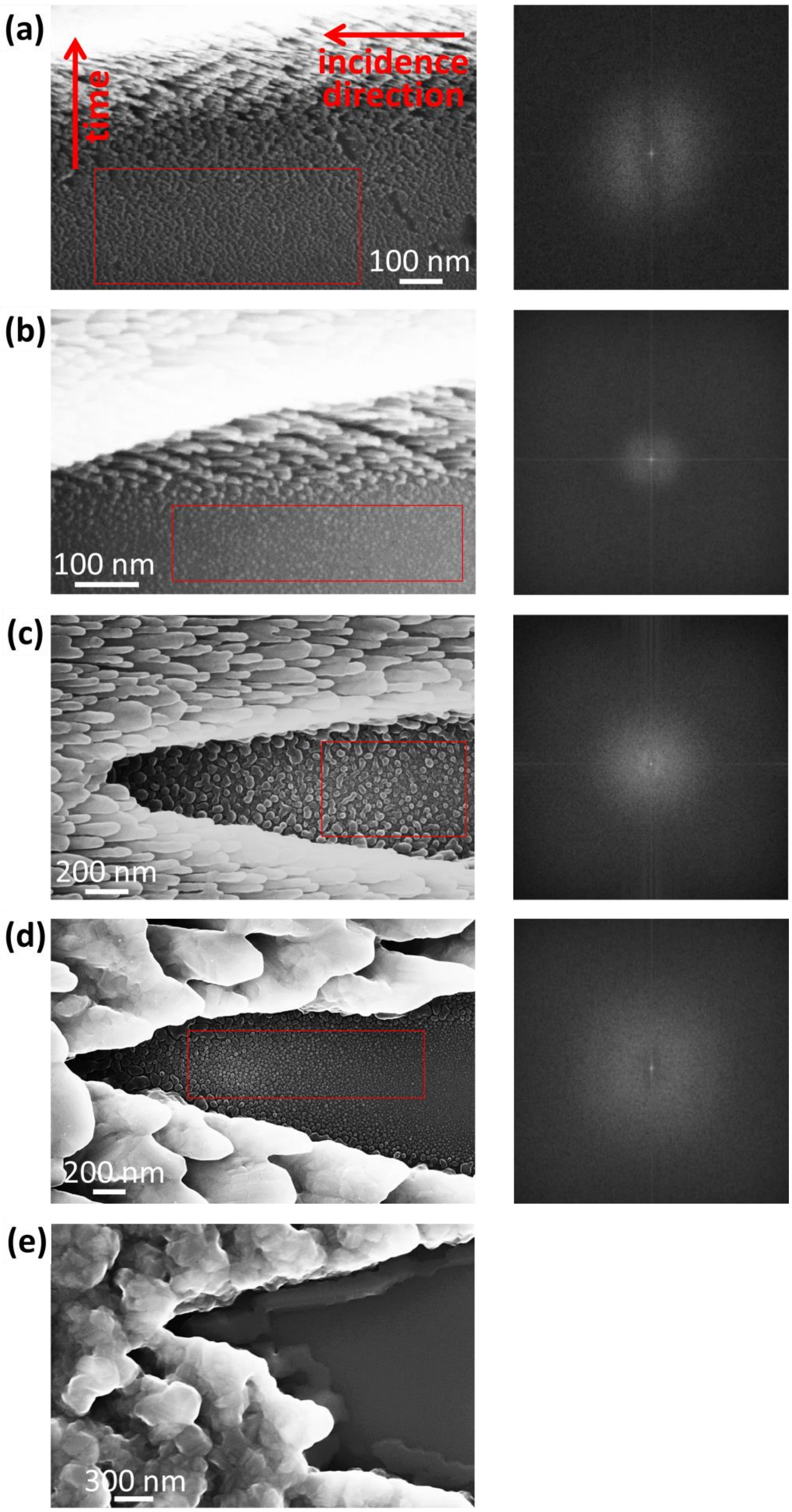

Figure 4.4: Top-view SEM images of regions that became continuously shadowed by a large dust particle during oblique deposition. Right of it, 2D FFTs from the indicated areas are presented. Deposition temperatures were (**a**) RT, (**b**) 300 °C, (**c**) 500 °C, (**d**) 700 °C, and (**e**) 750 °C.

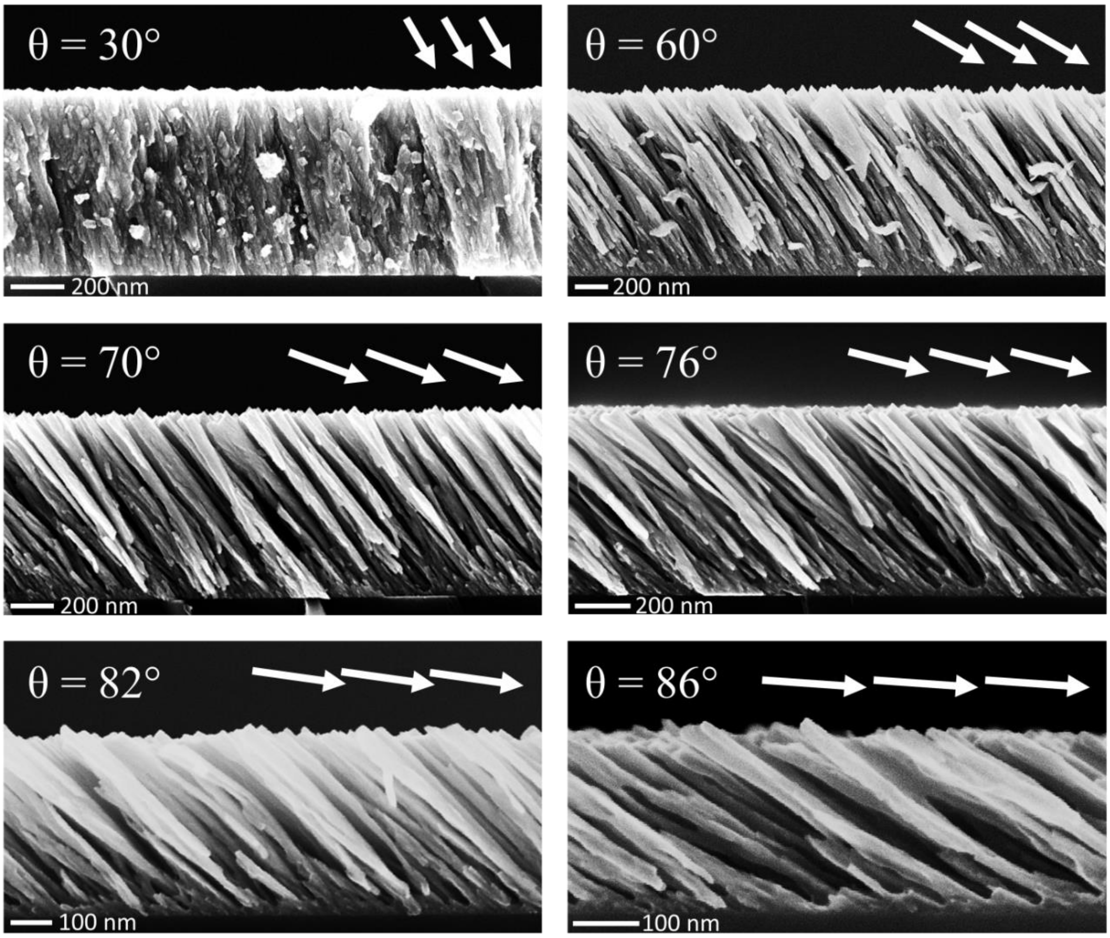

Figure 4.5: SEM images of Mo thin films, obliquely deposited at the indicated angles of incidence.

4.2 Tilt angles and density

It is known that the tilt angle β of the obliquely grown nanostructures depends on the angle of incidence θ, both measured with respect to the substrate normal. As can be seen in Figure 4.5, a more oblique incidence angle leads to a larger tilt angle. The relation between tilt angle β and the angle of incidence θ is under discussion since decades. As mentioned in chapter 2, the most commonly used mathematical expressions for this are the semi-empirical tangent rule [28] and the cosine rule [18] (also called Tait's Rule). Both give a purely geometrical relation, evading to include the influence that different materials or process conditions have. Furthermore, none of those gives an adequate estimation over the complete range of incidence angle $0 < \theta < 90°$. To study the validity of these phenomenological rules, Si, Ge and Mo thin films were deposited by e-beam evaporation at different angles of incidence at room temperature. In Figure 4.6 **a**, the measured tilt angles of this films are presented. It can be seen, that for all three materials different tilt angles can be observed and further that the cos- and tan-rules do not describe the found behavior sufficiently.

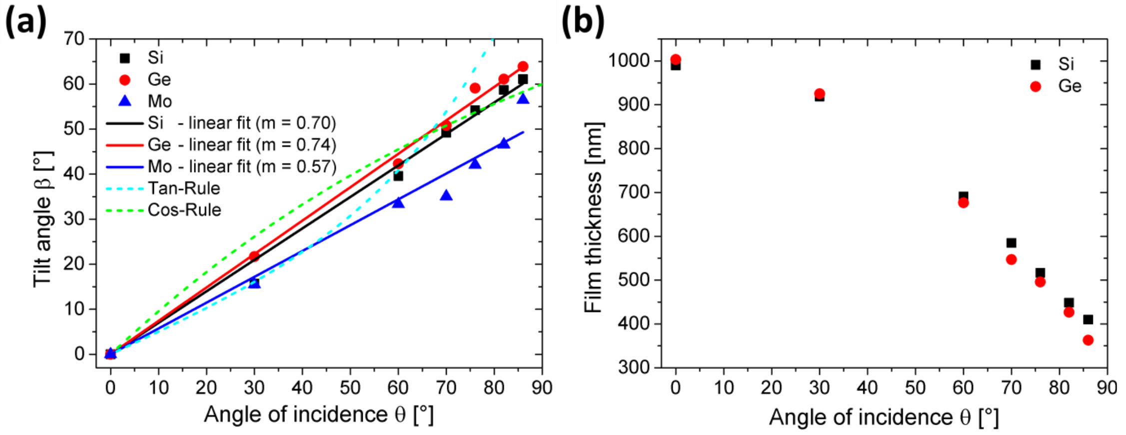

Figure 4.6: (**a**) Tilt angle vs. angle of incidence for Si, Ge, and Mo thin films at RT. Linear fits and the cos- and tan-rules are indicated. (**b**) Film thickness vs. angle of incidence for Si and Ge thin films.

The observed relation between β and θ can be estimated by a linear dependency over the complete angle of incidence range. This nearly liner behavior cannot be denied also for the experimental data, e.g., found by Tait *et al.* [18], Messier *et al.* [65], and the simulations from Krug [66], to name a few. Linear fitting provides the following slopes: $m_{Si} = 0.70$, $m_{Ge} = 0.74$, and $m_{Mo} = 0.57$.

All films were deposited with a vertical thickness equivalent (VTE) of 1000 nm. Consequently, the finally observed film thickness is a measure for the growth speed of the obliquely deposited films. Figure 4.6 **b** shows the measured thicknesses for Si and Ge. Only small differences between Si and Ge can be found, correlating with the small differences at the tilt angle measurements. Due to the high density of Mo and the enormous radiated thermal energy during evaporation, the used quartz microbalance showed strong deviations during the Mo deposition. Hence, no reliably thickness data are available for Mo.

Another parameter of interest is the density or porosity of the thin film. Direct measurement of the density of thin films is not a trivial task, as the total mass of these films is quite small. Porosimetry is only capable of determining the volume of open pores, but neglects inner voids [67]. Two different approaches were chosen to access this property. The first one uses the measured film thickness. Poxson *et al.* [68] have shown that porosity P and growth speed h/H are connected by

$$P = 1 - \frac{H}{h} \cos \theta. \tag{4.2.1}$$

The derivation of this formula is given later in chapter 6.3. The second approach utilizes X-Ray reflectometry (XRR) [69] to determine the density. As mentioned earlier, valid information about the growth speed of Mo is not available. On the other hand, the low

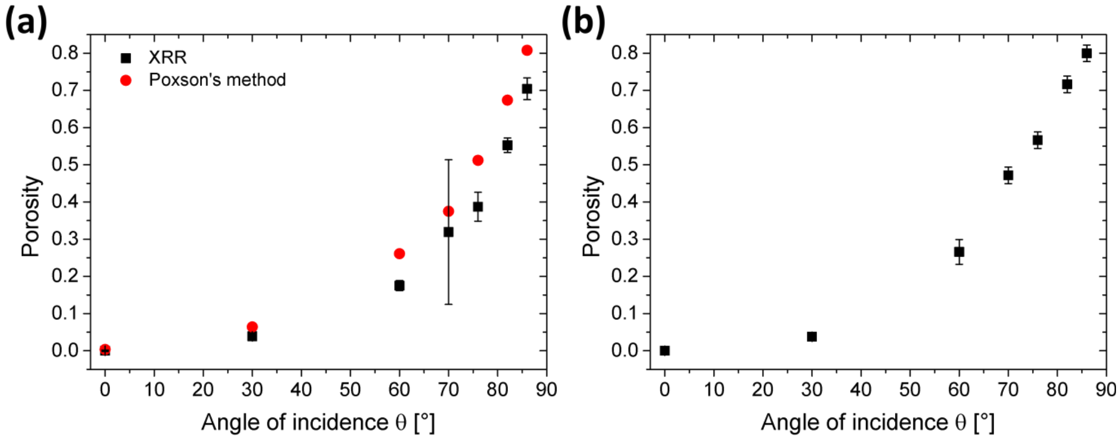

Figure 4.7: Porosity vs. angle of incidence for Ge (**a**) films, measured by XRR and calculated from the film thickness with Poxson's method [68]; as well as for Mo (**b**) films, measured by XRR.

density of the porous Si films makes it difficult to obtain reasonable XRR measurements. Thus, both methods can only be compared for Ge.

This comparison is presented in Figure 4.7 **a**. As can be seen, the porosities achieved from both methods show the same trend. In general, the porosities determined by XRR are smaller than the values obtained by Poxson's method. As Poxson verified his method by optical measurements, later the values obtained by his method are used. Figure 4.7 **b** shows the porosities obtained by XRR for the Mo thin films. In general, the expected trends could be observed. The more oblique the angle of incidence becomes, the more are the columns tilted, the slower grow the films and the higher becomes the porosity.

As a side note should be mentioned that the XRR measurements of the Mo films showed an interesting behavior when the azimuthal X-Ray incidence direction was close to the particle incidence direction during growth. For most of the azimuthal incidence angle range, a typical XRR measurement curve can be obtained, with a pronounced total-reflection 'shoulder' that indicates the actual density. However, when the sample is illuminated by the X-rays from the original material incidence direction, the curves loose this property. Smallest changes in the orientation then have a strong influence on the reflected intensity (see Figure 4.8). These curves, of course, were not used for density calculation. This effect may be caused by a reflection of the incident X-rays on the facetted surfaces of the highly oriented Mo structures or by a guiding effect in the porous thin film.

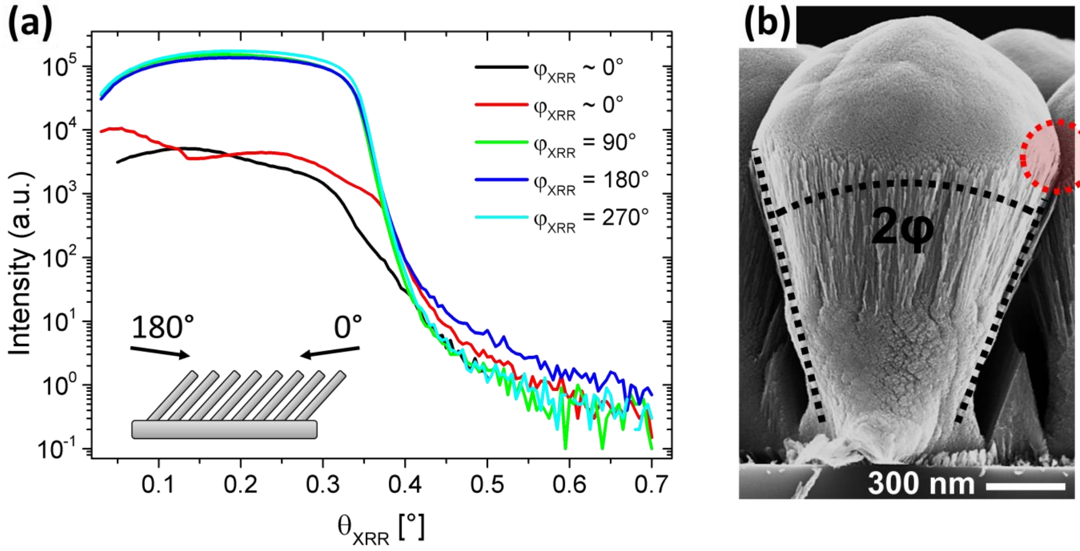

Figure 4.8: (a) Measured XRR curves for an obliquely deposited Mo sample. When the azimuthal angle of the X-Rays equals the azimuthal angle of incidence during deposition (so, when the X-Rays hit the 'tips' of the nanostructures), the curve deviates strongly from the expected results. (**b**) SEM image of a Ge 'fan structure', deposited vertically onto an isolated seed point. The fan angle φ as well as the point with the highest curvature is highlighted.

4.3 Fan angles

The main weakness of the tan- and cos-rules is the neglect of the influence of material parameters and deposition conditions. A promising approach to overcome this is the so-called 'fan model' from Tanto *et al.* [70]. In this model, oblique deposition is connected to overhang structures. Overhangs can be found, when material is deposited onto an edge or protrusion, forming a laterally broadening aggregation. Figure 4.8 **b** shows such an overhang structure that was formed by depositing Ge at normal incidence onto a lithographically prepared isolated seed point. Due to the characteristic shape, such aggregates are called 'fan structures'. The opening angle of such structures is called 'fan angle' and shall here be denoted as φ.

In an advanced model, based on Tanto's idea, it will later (chapter 6.3) be shown that the slope m of the nearly linear relationship between the tilt angle β and the angle of incidence θ can be identified with

$$m = \left(1 - \frac{\varphi}{90°}\right), \qquad \text{for } \varphi \text{ in } [°]. \tag{4.3.1}$$

Therefore, either the fan angle can be extracted from the β-θ-relation or it can be directly measured. Fan angles for various materials, deposited a different temperatures are presented in Figure 4.9. For Si, Ge and Mo, both methods give coherent results. To make the observations of different materials at different temperatures comparable, the homologous temperature T/T_{melt} is introduced. For this, the actual deposition temperature T is scaled to the melting point T_{melt} of the respective material. In general, the fan angle decreases with increasing temperature. Si and Ge show very similar results, what may be attributed to their nearly similar crystallographic characteristics.

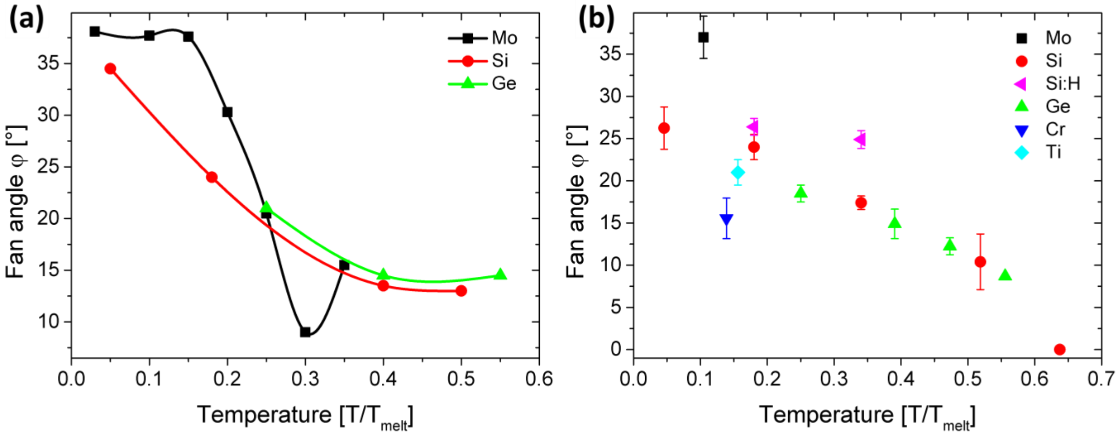

Figure 4.9: Fan angles of various materials, extracted from oblique deposition experiment (**a**) and direct measurements (**b**). Cr and Ti were investigated to have an example for other metals. T_{melt} for Si:H was assumed to be the same as for Si. The lines are a guide to the eye.

While Zhu *et al.* [71] already found a correlation between melting point and fan angle, to the best of the author's knowledge, no temperature dependent measurements are done before. The here obtained dependency of the fan angle from the deposition temperature implies a strong influence of surface diffusion. This assumption is supported by experiments that were performed with hydrogenated silicon, as described in the following. For this purpose, thermally dissociated atomic hydrogen was directed onto the substrate during silicon deposition. This leads to the formation of dihydrates on the silicon surface, increasing the adatom diffusion barrier [72-75]. Films obliquely deposited in the presence of atomic hydrogen were found to have a higher porosity and a smaller tilt angle, compared to the sample without hydrogen. Measuring the fan angle yields values as high as obtained for pure Si, deposited at 77 K. As neither the substrate temperature, nor the structural properties of the silicon are assumed to change strongly due to the incorporation of hydrogen, the found higher fan angles in this case could only be explained by the suppressed surface diffusion. A possible mechanism for the reduction can be found in the fact that surface diffusion is strongest, where curvature is largest (an estimation of exact relations can be found in [76]). The largest curvature on fan structures is found on the rim of the cone-like section, at the transition to the near-spherical growth front (highlighted red in Figure 4.8 **b**). If surface diffusion becomes stronger, adatoms tend to move away from these regions with high curvature, thereby reducing the lateral diameter of the fan structure and consequently also the fan angle.

4.4 Relevance of beam divergence

All of the previously in this chapter discussed samples were grown by electron beam evaporation. Another technique, sputter deposition, is more relevant for industrial applications for a variety of reasons (see section 2.1.1). One of the key differences between sputter deposition and evaporative deposition is the geometric divergence of the particle beam. A short overview of the morphological changes resulting from a larger beam divergence shall be given in this section. This is carried out for silicon, exemplarily.

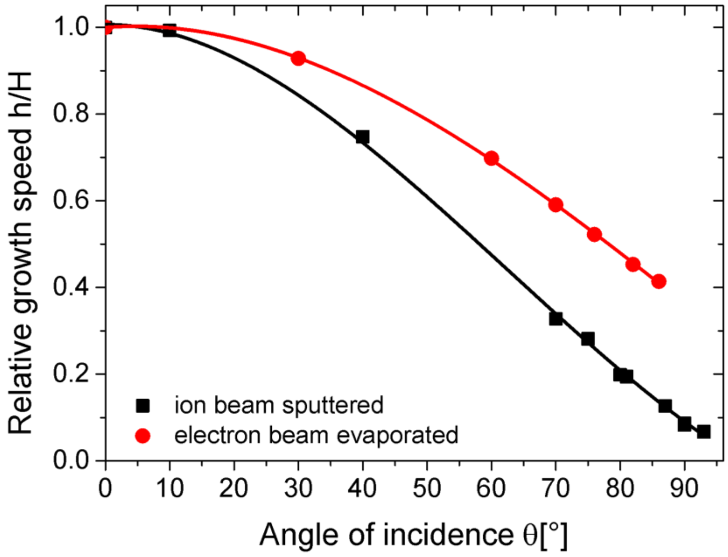

Figure 4.10: Relative growth speed of evaporated and sputter deposited silicon for varying angles of incidence.

Comparing the relative growth speeds for evaporated and sputtered silicon shows large differences (see Figure 4.10). The relative growth speed of the sputter deposited films drops faster, but extends into a range beyond $\theta = 90°$, which was not observed for evaporated films. This can be explained by the deposition geometry. The large ($d \approx 15$ cm) sputter target leads to a different behavior of the particle beam, when the substrate is tilted to oblique angles. When the substrate is tilted beyond a specific angle, a part of the target disappears below the horizon of the substrate plane. This angle can be calculated by $\theta_{div} = \arctan {}^{d}/_{2s}$, where d (= 15 cm) denotes the diameter of the target and s (= 15 cm) the distance from the target to the substrate. So, here $\theta_{\mathrm{div}} \approx 27°$, which is also the maximum geometric divergence of the particle beam, if viewed from the position of the substrate. For $\theta > \theta_{\mathrm{div}}$, the deposition geometry deviates remarkably from the evaporation case.

As a part of the target is not in direct line of sight to the substrate anymore, the amount of incoming material is reduced more and more. Furthermore, the medium angle of

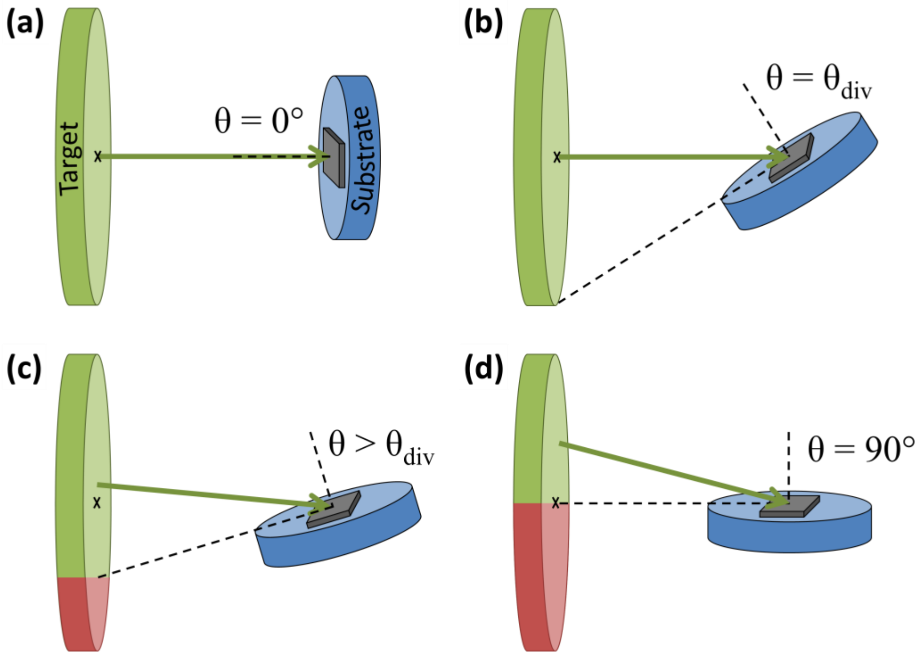

Figure 4.11: Schematic illustration of the relevant geometry of the sputter deposition experiments. (**a**) Normal deposition. (**b**) Oblique deposition, with the complete target visible. (**c**) Tilting further leads to a reduction of the visible area of the target and a shift in the medium flux direction (green arrow). Geometric and local angle of incidences are not the same anymore. (**d**) Even at $\theta = 90°$, the half of the total particle flux hits the target in an oblique manner.

incidence of the particles does not equal the geometric tilt of the substrate anymore. Both effects are illustrated in Figure 4.11. The exact dependency of the particle flux (amount and direction) at the position of the substrate is influence by a variety of parameters, especially if ion beam sputtering is used. These parameters are the primary ion beam shape and its energy, the angle with witch the ion beam hits the target, the position of the substrate relative to the target (distance and position relative to the target normal and the primary beam axis) as well as the atomic species of the primary ion beam and the target. Modelling this correctly would require tremendous numerical work and extensive use of empirical data for ion beam sputtering (e.g. from [9-11, 77]).

As a consequence, the relative growth speed of the sputter deposited films decreases faster with increasing deposition angle, compared to the evaporation case. The larger kinetic energy of the sputtered particles could also play a role, as it could reduce the porosity of the deposited film due to enhanced surface diffusion or a sticking coefficient less than one. A lower porosity would also lead to a lower growth speed (compare Equation (4.2.1)). Another consequence of the large beam divergence is that even at $\theta = 90°$ a significant amount of material reaches the substrate surface, leading to nanostructure growth in an angle range, that would be forbidden with an absolutely parallel flux.

Finally, the morphology of the sputter deposited films shall be compared to the evaporation deposited structures. Figure 4.12 **a** and **b** show columnar Si films, obliquely deposited by evaporation and sputter deposition, respectively. While the evaporated film consists of very thin needles with no visible broadening, the sputter deposited film shows an evolution from many thin nanostructures to much fewer broadened structures. The two main differences between the both utilized deposition techniques are the particle energy and the particle beam divergence, whose are both larger for sputter deposition. A larger particle energy would primary lead to enhanced adatom diffusion. This condition can also be realized by an increased substrate temperature during growth. As shown earlier, and once again presented in Figure 4.12 **c**, the morphology of films grown with enhanced surface diffusion deviates considerably from the one, observed for sputter deposition. The other possible consequences of an enlarged particle energy (as secondary sputtering, or defect formation) are not likely to cause the found structure broadening. Thus, the answer has to be searched in the enlarged beam divergence. To verify this, beam divergence was emulated artificially in the e-beam chamber. For this purpose, a sample was deposited with an angle of incidence periodically and rapidly varying between 90° and 60°. The result is shown in Figure 4.12 **d** and remarkably resembles the morphology of the sputter deposited Si film.

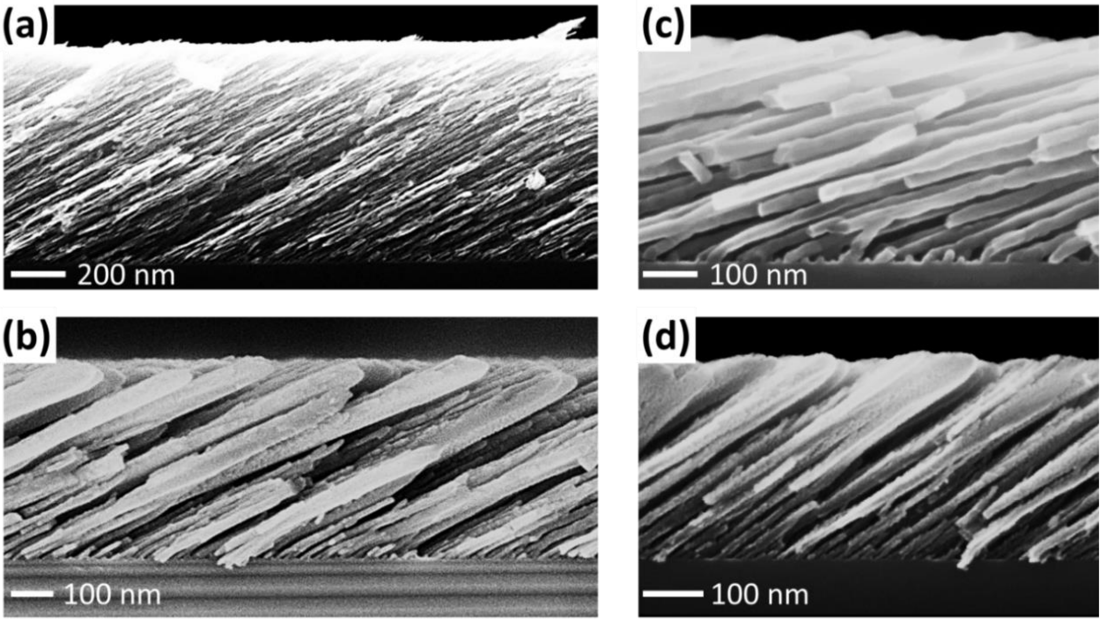

Figure 4.12: Obliquely deposited Si thin films. (**a**) E-beam evaporation. (**b**) Sputter deposition. (**c**) E-Beam evaporation at elevated temperature (500 °C). (**d**) E-beam evaporation with artificial beam divergence.

In an absolutely parallel particle beam, there are just two options. Either a dedicated point is shadowed or it is not. In a divergent beam, however, some structures can be partially shadowed. Structures that are not completely shadowed, but nevertheless do not have a direct line of sight to the complete target, only gather a fraction of the maximum possible flux. Therefore, these structures grow slower. Consequently, these structures become shadowed more and more, and finally stop to grow. This concept is illustrated in Figure 4.13. When growth of individual nanostructures stops, more material can reach the behind-standing columns, which then consequently grow broader.

The described influence of a distributed particle beam is also the cause for the well-known broadening of upright structures, grown by GLAD [78-80]. The substrate rotation distributes the incoming particles over the complete azimuthal angle range (compared to the polar divergence discussed above). Therefore, some structures may be shadowed at different rotation phases, leading to different growth rates and consequently to a broadening of the surviving nanostructures.

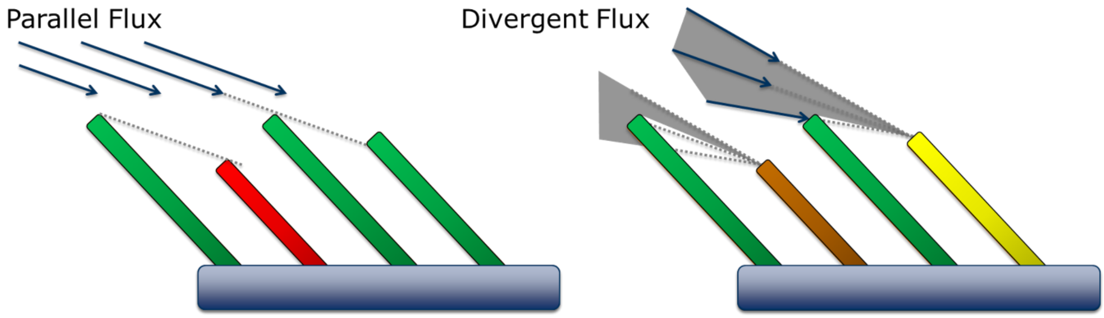

Figure 4.13: Schematic illustration of oblique deposition with a parallel, and a divergent beam. Green structures are not shadowed and proceed to grow. Red structures are fully shadowed and have stopped growth. Orange structures just see a fraction of the incoming particle flux and therefore grow slower, consequently becoming shadowed more and more with increasing deposition time.

4.5 Summary

In this chapter, experimental observations are presented, forming the base for the subsequent simulation and modelling chapters.

- It was demonstrated that films grown by electron beam evaporation show a columnar morphology for vertical and oblique deposition conditions. This is caused by the self-shadowing effect. For crystalline materials, an evolutionary selection of specific favored crystallite directions appears. This is the main reason for the different morphologies observed for amorphous (Si, Ge) and crystalline (Mo) thin films.
- Besides an enhanced crystallinity at elevated substrate temperatures, the main impact of an increased substrate temperature can be found in the enlarged diameter of the growing nanostructures. An explanation is the increased surface diffusion length, which permits the growth of larger nuclei before self-shadowing starts to dominate.

- Comparing the observed tilt angles with established models (cos- and tan-rules) shows a clear mismatch. The β-θ-relationship can be better approximated by a linear fit.
- The opening angles of fan structures (the 'fan angle') were measured for different materials and deposition conditions. It was observed that higher homologous temperatures lead to smaller fan angles. This indicates that surface diffusion plays a major role during the growth of fan structures and thereby also for the evolution of columnar thin films.
- This is supported by the fact that Si:H, where surface diffusion is reduced compared to pure Si, shows an significantly enlarged fan angle.
- The broadening of tilted nanostructures was attributed to beam divergence. Connected to this topic, some peculiarities of deposition processes that utilize a large particle source (e.g. sputtering from a large target) were illustrated. An important consequence is the fact that, at high incidence angles, the physical angle of particle incidence is not equal to the geometrical tilt angle of the substrate anymore.

5 Simulation

5.1 Introduction

The finally realized morphology of a grown thin film is the result of the interplay of a variety of different phenomena such as self-shadowing, surface diffusion, and the formation of a specific close-range order. Some of these effects can be studied theoretically (as the self-shadowing effect, see chapter 6), others may be the subject of computer simulations. While energy barriers are accessible from density functional theory (DFT), small-scale effects in thin film deposition on time scales up to microseconds can be investigated with molecular dynamics [81, 82] and Monte Carlo [83, 84] simulations. However, combining short-range effects (as diffusion) and long-range processes (as self-shadowing) into a single simulation is challenging. As an example, MD simulations work with amounts of $\sim 10^7$ particles on length scales in the range of a few tens of nanometers, at best. On the other hand, the self-shadowing effect may act over micrometers, thereby influencing the growth of billions or tens of billions of particles. To handle these dimensions, typically ballistic Monte Carlo simulations are utilized. The main task in such a simulation is to calculate which parts of the growing film are shadowed for the actual direction of the incoming particle flux. Other aspects, as surface diffusion, are afterwards modelled into such a simulation to fit experimental observations.

Due to the fractal nature of growing thin film surfaces, the surface area that is actually available for deposition processes may exceed the substrate area by orders of magnitude. Moreover, if the particle flux is not absolutely parallel (i.e. for substrate rotation or if particle divergence is taken into account), shadowing is not an absolute condition, as it may change as the deposition proceeds. Consequently, in order to model the shadowing effect correctly, the trajectory of each individual particle has to be calculated. Then the particle sticks at the collision position with the shortest path of the trajectory. Figure 5.1 **a** illustrates this concept, which is frequently called ‘collision detection’.

For both realized simulation approaches the language C++ was chosen, because it promises fast code execution. The complete code follows an object-oriented paradigm. Parallelization of ballistic algorithms is difficult due to the highly serial nature of this process. Where parallelization could be applied, it was done on loop-level, using the OpenMP [85] directives. All random numbers were created by a Xorshift pseudo random number generator [86]. For visualization an own code had to be developed, too (see section 5.5.1). The simulations were executed on a 6-core Intel® CPU in a Fedora Linux environment.

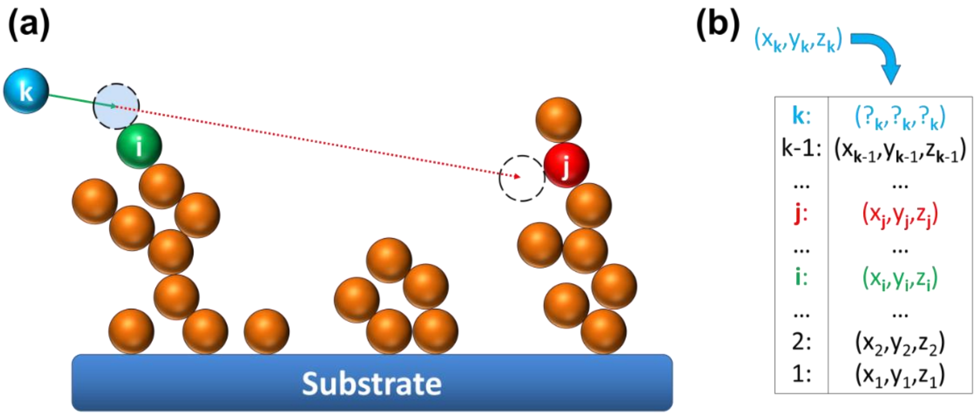

Figure 5.1: (**a**) Illustration of the 'collision detection' concept. On the trajectory of an incoming particle k, collisions could appear with the previously deposited particles i and j, for example. For the given trajectory, particle j is shadowed by particle i, so that the collision is realized with particle i. (**b**) Corresponding to the example in (a), a linear search in a list of all previously deposited particles would not necessarily find the closest collision candidate first. Thus, all particles must be checked.

5.2 Off-lattice approach

The mathematically correct way of modelling shadowing necessitates the use of spherical particles, which can reside at freely selectable floating-point coordinates, as already depicted in Figure 5.1 **a**. In such a case, the brute-force method would be a linear search in the list of all previously deposited particles. For each of these particles, the distance of the trajectory to the particles center has to be calculated. If this distance is smaller than the particles radius, it is a candidate for collision. In a final step, the candidate leading to the shortest trajectory is chosen, and the particle is stored at the corresponding collision position. Obviously, this approach is only suitable for very small 2-dimensional problems (see i.e. [87-89]). The necessary time for a single collision calculation grows linearly with the number of previously deposited particles. Consequently, the total number of necessary calculations scales with the square of the total number of particles to be deposited. This makes this approach unusable slow for larger systems, what is sometime metaphorically called 'combinatorial explosion'.

Common approaches to simplify many-particle simulations, like the division of the simulation volume into octrees, fail due to the fractal space filling behavior of the growing films. A simplification could only be found for the special case of an absolutely parallel particle beam. Even though the simulations are carried out in 3D, assume a 2-dimensional simulation cell for illustration as presented in Figure 5.1 **c**. Without loss of generality, let the coordinates in this cell be given in units of particle diameters and let the particle trajectories be aligned with the negative z-direction. At the beginning of the deposition of particle *i*, a random starting coordinate x_i is chosen (x_i and y_i in 3D). Due to the alignment of the trajectories, this initially chosen x_i-value cannot change during the flight of the particle. Then, collisions can only appear with particles having an x-coordinate that fulfills $(x_i - 1) < x < (x_i + 1)$. This fact is utilized to introduce a space partition. The simulation cell is divided into corridors with a width of one particle diameter, aligned to the negative z-direction. Each of these corridors is represented by a list of particle slots. The particles are assigned to the corridors by taking the integer part of their coordinates. For example, a particle with $x = 5.2$ is assigned to corridor 5. Inside these corridors, the particles are ordered by their z-position. So, the topmost particle with the largest z-value sits on slot 1, the next particle on slot 2 and so on. It is obvious that collisions can only appear with particles that are stored in adjacent corridors, significantly reducing the number of necessary calculations to find the candidates for collision. Moreover, the calculation itself is transferred to a lower dimension, because the z-coordinate is not needed for it. Finally, the collision candidate with the highest z-position is chosen and the corresponding z_i-value for the incoming particle is calculated.

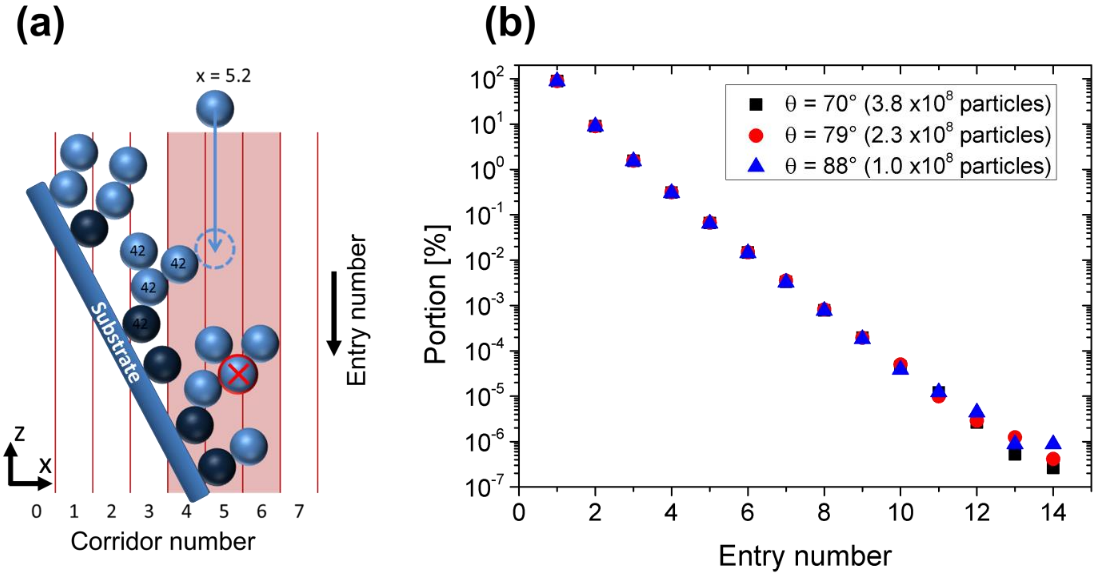

Figure 5.2: (**a**) For perfectly vertical deposition, collisions are only possible with particles within a small selection of coordinates. Illustrated is an example deposition in 2D, with N = 2 stored particles in each corridor. A new particle impinges with x = 5.2. Collisions can only appear with particles stored in the corridors 4, 5, and 6. After all six possible collisions (2 particles x 3 corridors) were checked, the particle is positioned at the highest found z-position. It is then assigned with the cluster number of the particle it has hit (here: 42). Finally, the particle with the lowest z-coordinate in corridor 5 is removed (crossed red). (**b**) Distribution of particle collisions for oblique deposition in 3D. The entry number describes the particle order inside a corridor. The probability of an impinging particle to collide with a particle of the given slot number is shown. Around 89 % of all collisions appear with the topmost particle of the deposition corridors.

The deciding improvement follows from the z-ordering inside of the corridors. If only the top *N* particles of each corridor are tested as collision candidates, the total number of necessary collision tests becomes a fixed value. In the 2D example, only 3 corridors can hold particles relevant for the collision calculation so that only $3 \cdot N$ calculations have to be performed. In the 3D simulations, 8 corridors are adjacent to a selected one (in the x-y-plane). Consequently, $9 \cdot N$ particles have to be checked. Figure 5.2 **a** illustrates a single 2D deposition event, with $N = 2$.

A statistical examination reveals that – in 3D – 89% of all particles collide with a particle stored in slot 1. The probability of colliding with deeper buried particles decreases nearly exponentially, as shown in Figure 5.2 **b**. Roughly, only 1 out of 10^9 particles collides with a particle stored in slot 14. Hence, if $N = 20$ slots would be used, 10^{10} particles could be deposited, without any deviation from the brute-force result, with near certainty. In all performed simulation runs, $N = 25$ was used. This means that for each deposited particle, the fixed number of 225 collision tests was carried out.

OAD was realized by introducing a tilted substrate into such a simulation cell. An additional parameter was assigned to each particle, allowing to identify connected clusters (compare Figure 5.2 **b**).

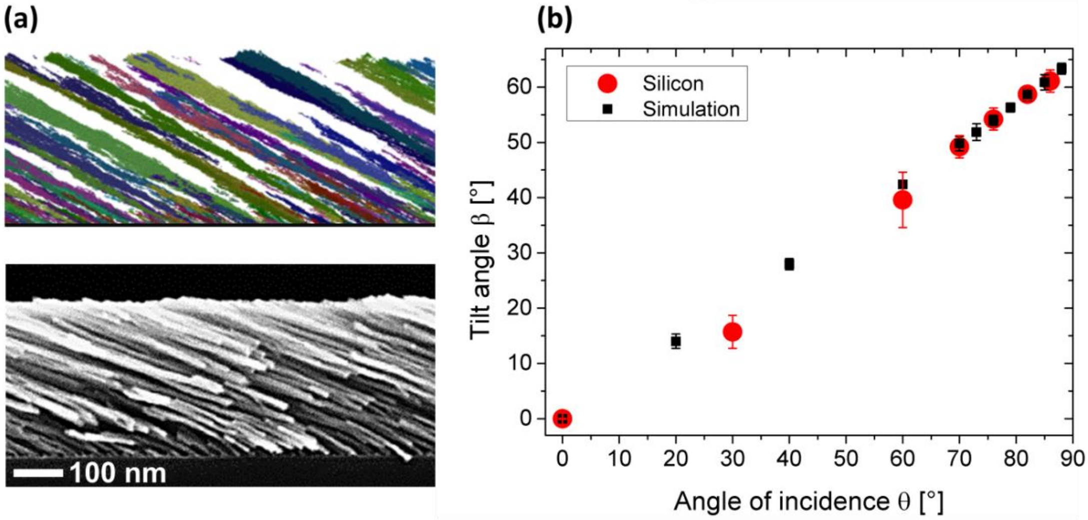

Figure 5.3: (**a**) Image of a simulated film and a side-view SEM image of an obliquely deposited Si film. The columnar morphology of OAD thin films can be reproduced with this simulation approach quite well. (**b**) Tilt angle depending on the angle of incidence for simulation and experimental results. The tilt angles observed from the simulation show the same trend as the observed ones for evaporated silicon. The nearly perfect match of the results is a coincidence.

With this simulation approach, the columnar morphology of the OAD films can be modelled. Figure 5.3 **a** shows a cut through a 3D simulation cell compared to an obliquely deposited silicon film. Different colors are assigned to different clusters for visual clarity. The tilt angles of the simulated nanostructures show a nearly linear dependency from the angle of incidence, fitting to the experimentally observed results for silicon, as presented in Figure 5.3 **b**. The exact match of the observed values with evaporated silicon films is a coincidence. The overall morphology of the simulated OAD films is in good agreement with the experimental observations.

Due to the restriction to an absolutely parallel particle flux, the presented simulation cannot be used to investigate GLAD or the influence of beam divergence. Nevertheless, it can be used to investigate some fundamental growth processes. As pointed out in section 4.3 overhang and fan structures play an important role in the understanding of OAD and GLAD. Such structures can be simulated with the off-lattice simulation by introducing special substrates into the simulation cell. The simplest substrate is a single, isolated particle at a fixed position. Figure 5.4 **a** shows the result of the deposition onto such a particle. The two different colors imply that two particles collided with the seed particle, leading to the formation of two clusters, as illustrated in **b**. Because point-like substrates are not achievable in real depositions, in a second simulation a large sphere was assumed as substrate. This approximates the case of a free-standing seed point, produced by lithography, exemplarily. In Figure 5.4 **c** and **d** a comparison of a simulated and a germanium fan structure is shown. Thin fibers can be observed on the sidewalls of both structures. The growth of an overhang structure on a sharp edge can also be modelled, as demonstrated in **e** and **f**. Two significant observations can be made from the simulated fan structures: 1. The simulated fan angle is always $\varphi = 24°$. This is coincidentally the same value as found for evaporated silicon, deposited at room temperature, explaining the above-mentioned match of the tilt angles. 2. The growth front (the cap of the fan) can be approximated as a half-sphere for all seed geometries.

Examining the inner structure of a simulated overhang gives insight into the density distribution. For normally deposited films on a flat substrate, an equilibrium density of 0.28 particles / diameter^3 was found, in good agreement with the observations of other groups [90]. On the edge of the overhang, the density gradually drops to zero (see Figure 5.5 **a**), which can be attributed to the locally oblique incidence on the outer part of the growth front.

Growth dynamics are available by the off-lattice simulation, too. In Figure 5.5 **b,** the tilt angles of all nanostructures in an OAD simulation are analyzed. Many structures stop to grow at the early stages of growth and that the tilt angle variation is large at the beginning. A height of around 100 particle diameters is necessary to achieve stable shadowing conditions, and thereby nearly constant tilt angles.

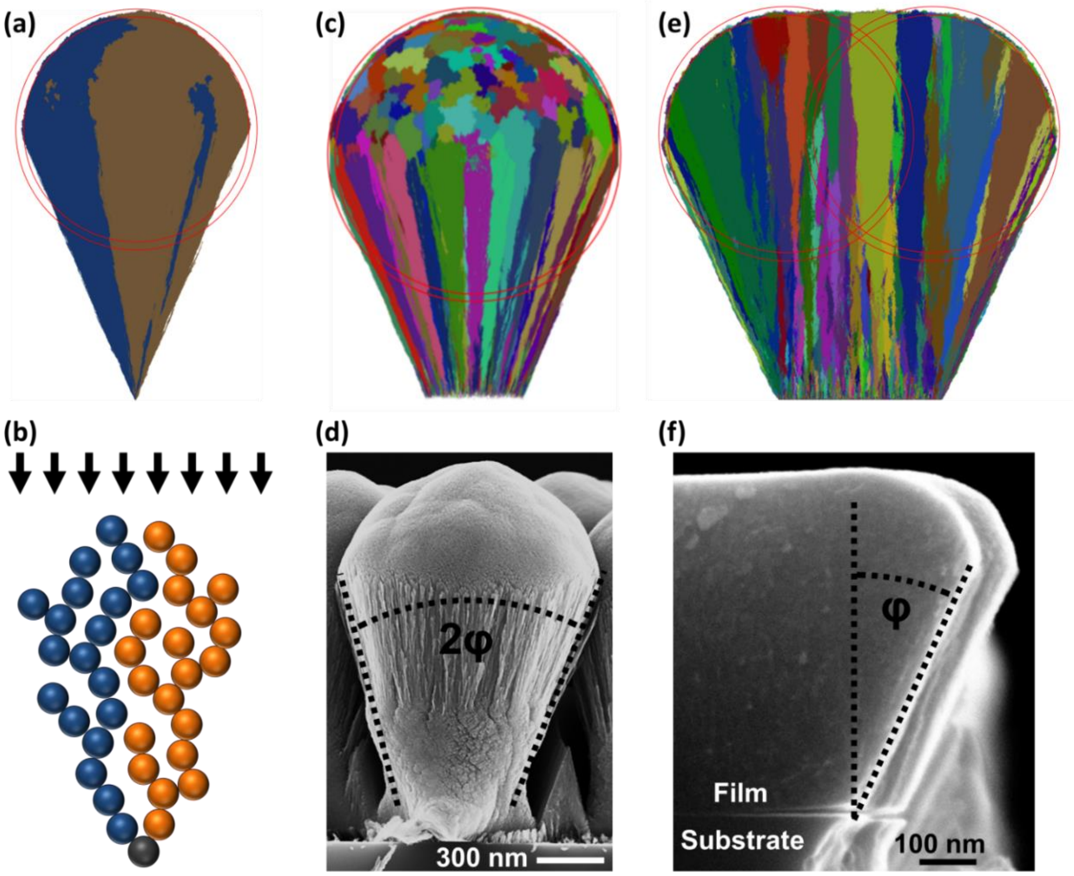

Figure 5.4: (**a**) Simulated fan structure on an isolated seed particle. (**b**) Sketch of the early-deposited particles, illustrating how two different clusters could arise. (**c**) and (**e**) show simulated fan structures on a large spherical seed and a plateau, respectively. (**d**) shows a Ge fan structure on a NSL seed and (**f**) illustrates a Si overhang structure deposited onto an edge. Concentric circles are added to the images of the simulations, to highlight the nearly spherical growth front.

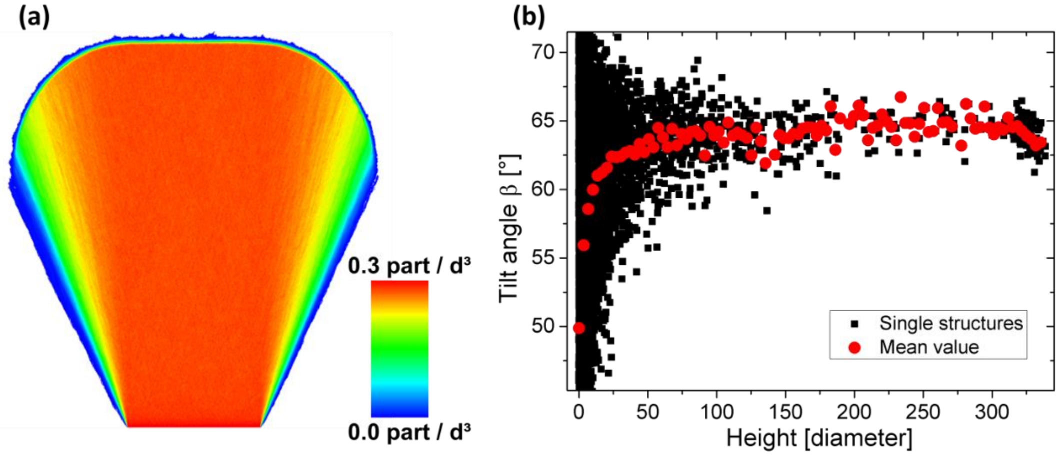

Figure 5.5: (**a**) Density distribution inside a simulated overhang structure. At the edge of the overhangs, the density continuously drops to zero. (**b**) Tilt angle distribution of nanostructures during the growth. With the increase of the height (film thickness), the average tilt angle increases up to a stable angle. This indicates the competitive character of the growth process under oblique incidence conditions. Many nanostructures stop growth during deposition.

5.3 On-lattice approach

The unavoidable restriction to an absolutely parallel particle flux limits the usability of the off-lattice simulation. In order to allow the usage of rotation or beam divergence, the calculation of the collision detection has to be simplified extremely. This can be done by restricting the particle positions to integer coordinates, meaning that the complete simulation cell is divided into a regular cubic lattice. Therefore, simulations using this approach are called 'on-lattice' simulations. All particles reside on this lattice and all possible interactions have to be modelled onto the lattice. Figure 5.6 **a** illustrates this concept. In such a simulation, the particles are moved stepwise through the simulation grid on their trajectory. After each step, the neighboring lattice points are checked. An occupation of one of those indicates that a collision has occurred. Since complex calculations are not required (just read-operations on memory), the process is quite fast. Moreover, only the lattice points adjacent to the particles trajectory have to be checked. With the increased speed-up of collision calculation, large amounts of particles can be simulated in reasonable time, so that this kind of simulation is used frequently to model GLAD [89, 91-93].

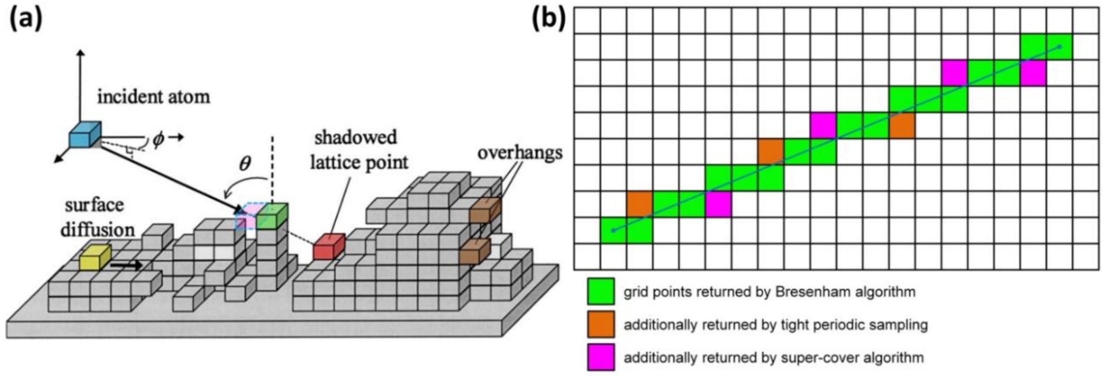

Figure 5.6: (**a**) Illustration of the on-lattice approach. All particles are tied to lattice points. In addition, the ballistic traversal of the particle through the simulation cell as well as surface diffusion has to be carried out on the simulation lattice. (Image taken from Karabacak *et al*. [61], colored by author.) (**b**) Different algorithms can be used to calculate the lattice points that are located on the trajectory of a particle. For the presented simulation, a super-cover algorithm was chosen.

The fact that this model is also used for demonstrating purposes of graphic libraries [94] reveals that it is used on a regular basis. Before showing major results of such simulations, the calculation of the particle trajectories through the simulation lattice shall be discussed. To the best knowledge of the author, in none of the existing publications the motion of the particles through the lattice is discussed. While this is a trivial question for movements aligned to the cell axes, it becomes more complex for random directions. Rasterization of line segments is a fundamental problem in computer graphics and the automation of machine tools (CNC), too. The probably most favorite rasterization algorithm was described by Bresenham [95] for the control of digital plotters. The Bresenham algorithm returns most lattice points, which are intersected by a line segment relatively fast (green points in Figure 5.6 **b**), but misses some lattice points whenever a jump into the next integer row takes place. A possible way to receive more points would be to divide the trajectory into small sub-segments and to sample each of the end points. If smaller segment lengths are chosen, the accuracy of this approach increases, as does the calculation time (orange points in Figure 5.6 **b**). Methods that return all intersected grid points directly are called ‘super-cover’ algorithms, and should be preferred for such simulations (purple points in Figure 5.6 **b**). For the simulations here, a 3D version of a “Digital Differential Analyzer” (DDA) algorithm was implemented [96], representing a fast realization of the super-cover approach.

For the simulations presented in the following, neither surface diffusion was included, nor were any other interactions of the incoming particles considered. Therefore, the resulting films show a pure amorphous structure, without any short- or long-range order.

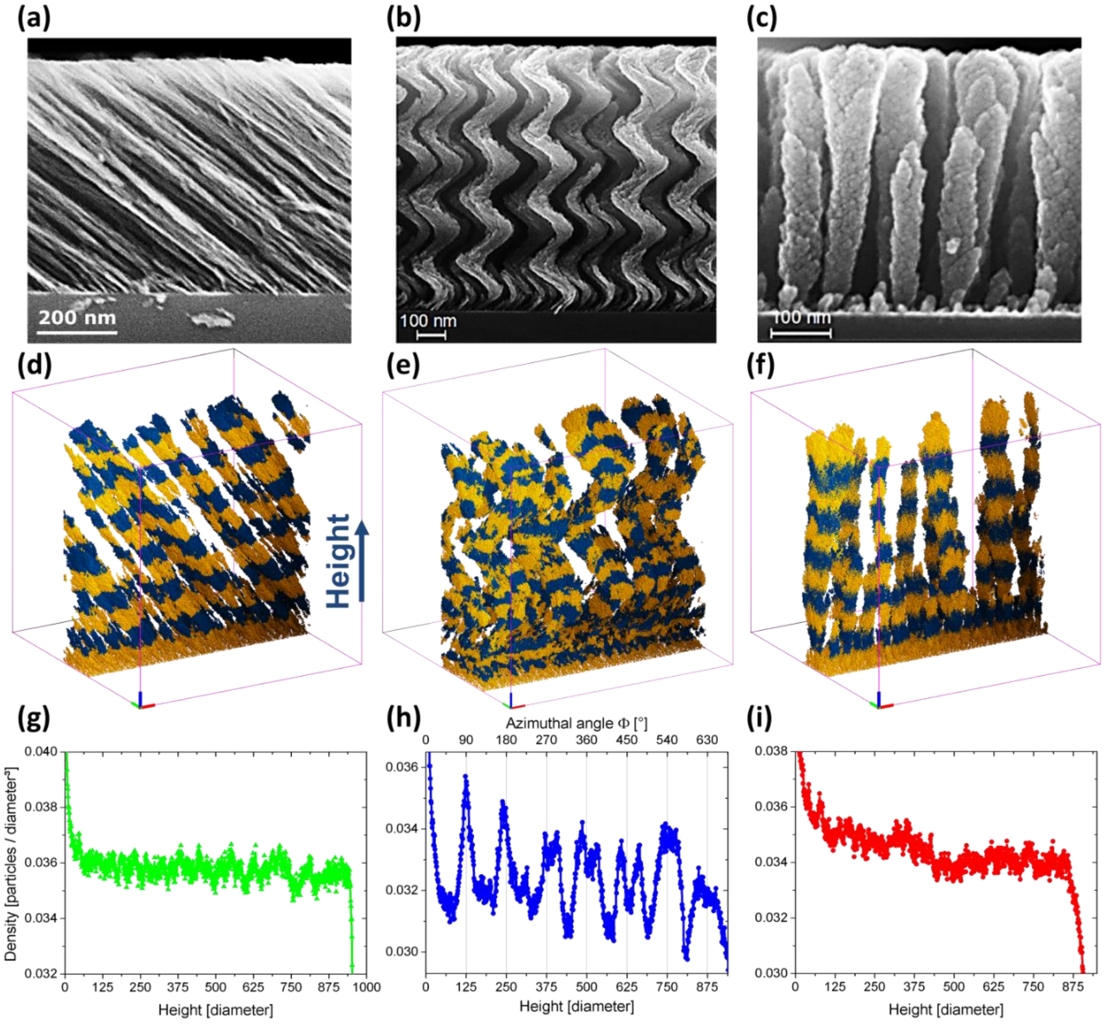

Figure 5.7: (**a**), (**b**), and (**c**) show SEM cross-section images of Si films grown obliquely without, with slow, and with fast rotation, respectively. (**d**), (**e**), and (**f**) illustrate the corresponding computer simulations. For all three cases, the angle of incidence was fixed to $\theta = 85°$ and the simulation cells had the dimensions 1000 x 1000 x 1000 lattice points. (**g**), (**h**), and (**i**) show the corresponding density profiles. The oscillations that are observed in the spiral case (**h**) can be attributed clearly to the actual direction of the incoming particle beam.

The off-lattice simulation can be applied to model most of the structure shapes, accessible by GLAD. Exemplarily, structure growth is simulated with increasing substrate rotation speed, leading to the growth of tilted, spiral, and upright columns. Figure 5.7 **a** - **f** show a comparison of SEM and simulation images for these cases. The overall morphology is reproduced well, the structures are separated, and the growth competition can be observed as well.

However, for optical applications, the height resolved density profile of GLAD films is an important parameter. In Figure 5.7 **g** - **i** this density profile is depicted for the three cases. For the OAD case (**g**) the density close to the substrate is large. This can be explained by the fact that the initial substrate is totally flat so that shadowing does not appear. The density drops until it remains nearly constant after a film thickness of approximately 100 lattice points is deposited. This correlates with the observation that the tilt angles also become stable after a thickness of around 100 particle diameters. For the case of fast rotation leading to upright structures (**i**), shadowing needs longer to become stable and larger variations of the density can be observed, which can probably be attributed to the higher roughness of this film compared to the OAD film.

For the film grown with slow substrate rotation, a monotonic behavior is expected similar to the other two cases. Instead, an oscillation of the density is found. A more detailed view reveals that the maxima of the oscillations appear, whenever the particle flux was aligned to the simulation cell axes. This observation contradicts the physical expectation completely, as in the experimental realization, absolute isotropy for the in-plane rotation is evident. Consequently, this artificial anisotropy is an artefact of the simulation lattice. As the density varies more than 15% in the observed film, it can clearly not be neglected.

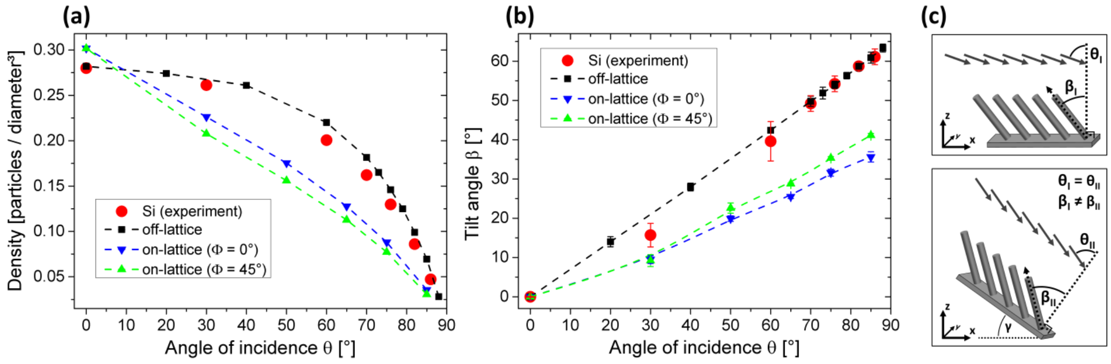

Figure 5.8: Density (**a**) and tilt angle (**b**) dependency for obliquely deposited silicon films, off-lattice simulations and on-lattice simulations, with the incidence direction aligned to the lattice x-axis (Φ = 0°) and in-plane-rotated to Φ = 45°. While the off-lattice simulation fits well to the experimental observations, both on-lattice cases show a different behavior. Moreover, there is a deviation between both on-lattice runs, which influences all on-lattice simulations that include a substrate rotation. (**c**) Schematic illustration of the "grid effect" found by Tanto *et al.* [93]. The angle of incidence θ is the same in both cases, but different tilt angles β are observed.

To quantify this effect, nanostructure growth was simulated without rotation, but in a first run with the particle trajectories aligned to the lattice x-axis (Φ = 0°) and in a second run in-plane-rotated to Φ = 45°. This was carried out for various incidence angles θ and the results were compared to the off-lattice simulation and the experimental values of Si OAD films. In Figure 5.8 **a** and **b** the results for the observed densities and tilt angles, respectively, are presented. Obviously, the observations from the on-lattice simulations deviate strongly from the values obtained by the other methods. The difference between the Φ = 0° and the Φ = 45° runs is smaller, yet clearly visible, thus explaining the density oscillations found in the spiral nanostructures. Indeed this effect influences all simulations including substrate rotation.

Tanto *et al.* [93] found a similar anisotropy. As illustrated in Figure 5.8 **c**, the tilt angle of nanostructures does not only depend on the angle of incidence in on-lattice simulations, but rather on the orientation of the entire assembly with respect to the simulation lattice, as well. Tanto *et al.* named the influence of the simulation lattice “grid effect”.

As a consequence of this observation, it has to be stated that all on-lattice simulations using substrate rotation are influenced by the grid effect, as well as are all observed β-θ-relations based on this approach. In other words, due to the lack of spatial isotropy, simple on-lattice simulations neither can be used to investigate realistic deposition cases nor describe the idealized mathematical ballistic deposition process (represented by the off-lattice simulation). A strong influence of the grid effect can be found on the growth of fan structures, too. As illustrated in Figure 5.9 and also found previously by Tanto *et al.* [93], the value of the fan angle φ depends strongly on the direction of the incoming particles and is largest when the particles arrive along a grid axis and smallest when the trajectories are tilted by 45°. Since the fan angle is an important parameter to describe oblique deposition, its stability can serve as a measure for the strength of the grid effect.

Within their investigation, Tanto *et al.* noticed that the grid effect can be reduced by the usage of 7-cube cluster particle [93]. Compared to the ‘normal’ particles of on-lattice simulations, which can be interpreted as cubes (see Figure 5.10 **a**), such a cluster particle is a combination of seven cubes, as illustrated in Figure 5.10 **b**.

In Figure 5.9 **b**, the reduction of the grid effect by using such cluster particles (“R = 1” curve) can be seen. The variance of the fan angle φ with the angle of incidence θ is already significantly reduced, but still observable. Furthermore, the fan angles in the on-lattice simulations with the cluster particles are larger than the value of 24°, which is found in off-lattice simulations. To reduce the grid effect further, the obvious approach would be to use even larger cluster particles. These particles can be defined as all lattice points that have a distance not larger than a radius R from the center of the cluster. Figure 5.10 **c**, **d** and **e** illustrate particles constructed like this with radii of two, three, and four lattice points, respectively. Thus, the cluster particle constructed

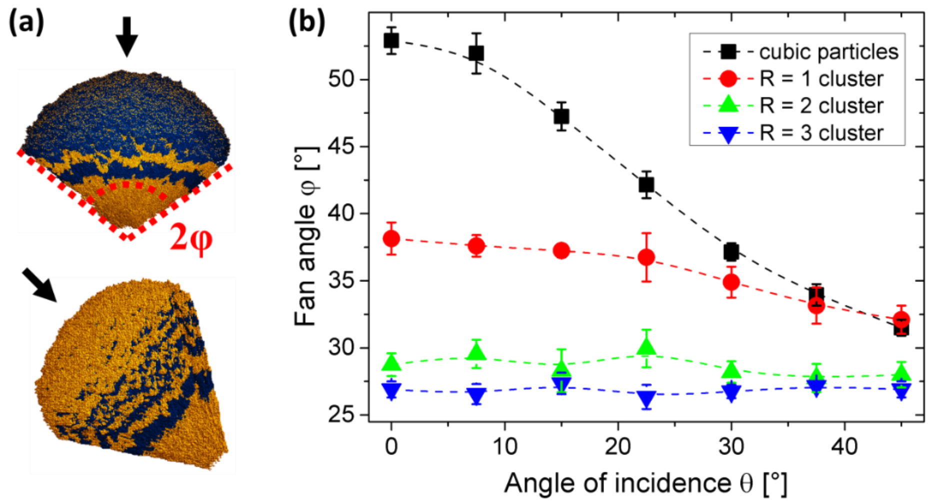

Figure 5.9: (**a**) Two fan structures, deposited onto an isolated seed point, with different angles of incidence. Both show different fan angles φ. (**b**) Dependence of the fan angle φ from the angle of incidence θ for different particle sizes. With increasing cluster particle radius, the influence of the angle of incidence vanishes increasingly. The fan angle found in off-lattice simulations is φ = 24°.

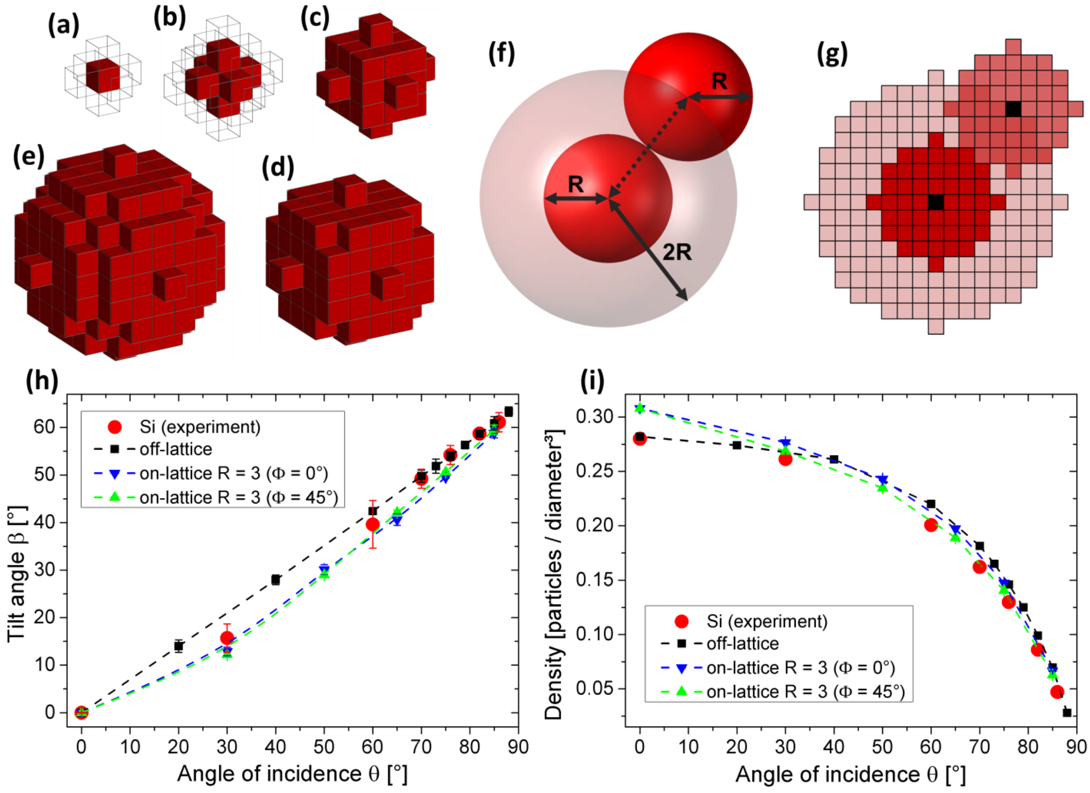

Figure 5.10: (**a**) A cubic particle, with six indicated sticking points on its faces. (**b**) The R = 1 cluster particle provides 18 sticking points. (**c**), (**d**) and (**e**) show cluster particles with R = 2, R = 3, and R = 4, respectively. (**f**) The centers of two spheres, touching each other have always a distance of 2R. Consequently, around each particle exists a 'forbidden' volume that cannot be penetrated by the center of other spheres. (**g**) shows this concept transferred to a simulation lattice. Instead of the actual volume of the deposited spheres (dark red), the 'forbidden' volume is marked (bright red). Then, collision detection can be performed by checking if the center of the incoming particle has entered this zone. (**h**) and (**i**) show, respectively, the dependencies of the tilt angles and the densities on the angle of incidence for R = 3 cluster particles.

with seven cubes would correspond to R = 1. To test this approach, the fan angles are determined for cluster particles with radii of two and three. In these both cases, the fan angle remains nearly constant, independent of the angle of incidence, and with increasing R seems to trend toward the off-lattice value. To verify that the use of cluster particles improves the simulation of GLAD films, the tilt angle and density dependencies were evaluated again, using R = 3 cluster particles. As shown in Figure 5.10 **h**, the simulated tilt angles with the cluster particles show nearly no dependence on the azimuthal deposition angle Φ and approach the off-lattice values. For the densities, the dependence from Φ is reduced and the dependence on the angle of incidence θ converges to the off-lattice case too, as depicted in Figure 5.10 **i**.

The reason for the cluster particles to reduce the grid effect is the enlarged number of possible sticking points with an increasing radius, so that the clusters act as particles that are more spherical. However, this is a drawback of this approach as well. Obviously, to store the same amount of particles, the required volume of the simulation cell scales with R^3. Furthermore, not only that the number of sticking points to be checked after each particle movement step scales with the surface area of the particle (~R^2), but also more steps are necessary for the particle to travel the distance of its own diameter (~R). Thus, the total time needed for collision detection calculation scales with R^3, too.

An approach to overcome this drawback is to utilize the fact that with increasing R the particles resemble more and more spheres. The centers of two spheres with radius R that touch each other have a distance of 2R, as depicted in Figure 5.10 **f**. Consequently, around each sphere a 'forbidden volume' exists that cannot be entered by the center of other spheres. This allows a remarkable simplification of the collision detection. Instead of saving a deposited particle directly inside the simulation cell, its 'forbidden volume' is marked. So, all lattice points within a radius of 2R are set to true, as indicated in Figure 5.10 **g**. For collision detection of an arriving particle, it has to be checked if its center point has moved onto an already marked lattice point. That means that checking a single lattice point of the simulation cell after each movement step is sufficient. With this approach, the time for collision detection just scales with R (due to the still longer trajectory of the particles), facilitating the use of larger cluster particles.

5.4 Further applications of the on-lattice simulation

The ability to give insights into complex deposition problems is the strength of the presented on-lattice simulation. A selection of example cases is presented in this section to demonstrate this. All the shown simulations utilize cluster particles with R = 3.

5.4.1 Shape evolution of ordered structures

On flat, non-patterned substrates, OAD and GLAD lead to the growth of randomly arranged nanostructures, which show varying shapes and diameters. This is caused by the fact that each individual nanostructure is influenced by different shadowing conditions, arising from the random nucleation at the early stages of growth In contrast, the arrangement of the initial highest seed points and consequently the position of the growing nanostructures becomes controllable with lithography techniques [48, 97-103]. Especially the honeycomb pattern that can be prepared by nanosphere lithography (NSL, see section 3.1.4) shows some interesting features.

As illustrated in the top image of Figure 5.11 **a**, three characteristic lengths exist, which are relevant for shadowing. These different lengths originate from the manufacturing process of this kind of template, which utilizes a close packed layer of polystyrene spheres with a diameter D. Consequently, the distances to the neighboring seeds are D/√3, D, 2D/√3, as illustrated in Figure 5.11 **a** in the colors green, red, and blue, respectively. Bauer *et al*. have investigated, how these different lengths influence the cross-sectional shape evolution during growth [103]. Growing vertical nanostructures

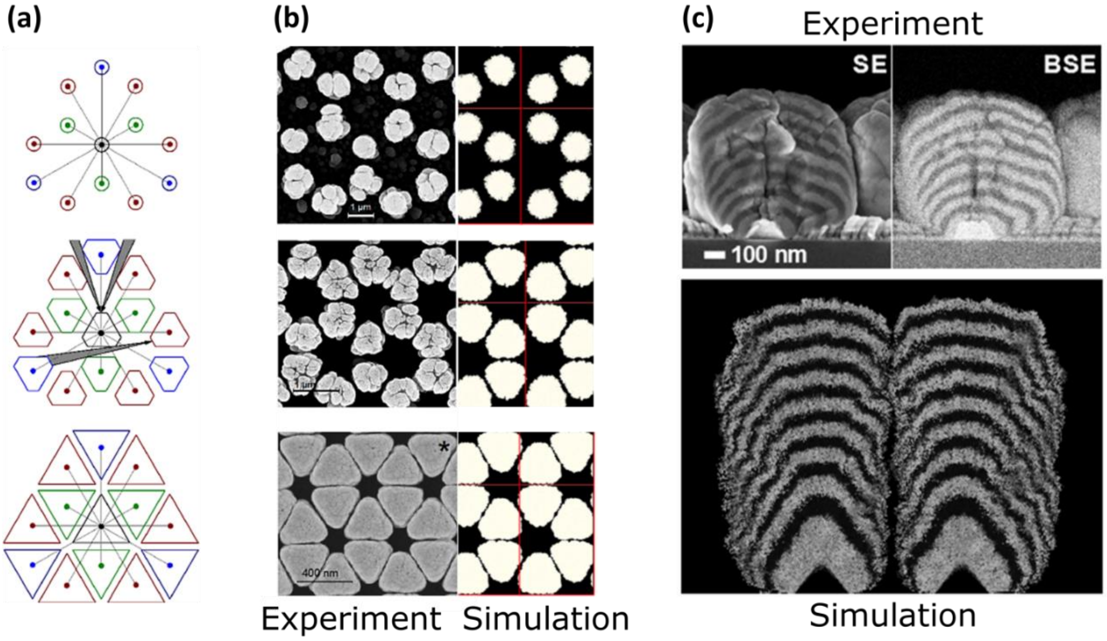

Figure 5.11: (**a**) Schematic illustration of the shape evolution during GLAD on a honeycomb seed array. The in-plane shape evolves from round over hexagonal to triangular. Long free allays allow material to be transported into deeper zones of the growing film. (**b**) Corresponding comparison of top-view images of experimentally deposited and simulated nanostructures. (**c**) Comparison of the inner structures of Si/Ge heterostructures (taken from [103]) and a corresponding simulation. At the beginning, the inner interfaces mimic the geometric shape of the seed point. Later, the interface is quite flat in the center axes of the structures, but strongly bends at the edges, which is caused by material that penetrates deeply into the porous film.

onto such a pattern leads to a characteristic shape evolution. At the beginning shadowing between the seeds does not occur so that the nanostructures show a circular in-plane shape. When the diameter of the structures has raised far enough, shadowing starts to act in various directions at different points in time. Therefore, the in-plane cross-sectional shape of the nanostructures alters from circular, over hexagonal, to reach a triangular shape, finally. As indicated in the middle image of Figure 5.11 **a**, long free alleys exist, allowing material to be transported deeper into the growing film, condensing on lower parts of the nanostructures surfaces. Figure 5.11 **b** shows selected examples of upright nanostructures in different growth stages, compared to on-lattice computer simulations. For these simulations, cone-shaped seed points are arranged in a honeycomb pattern and subsequently GLAD was carried out. As can be seen, the simulated time evolution of the nanostructures cross-sectional in-plane shape reproduces the observed shapes quite well.

The inner structures of such deposited upright nanostructures might be an important property for some applications. An example is the deposition of semiconductor pn- or pin-junctions. Direct observation of this inner structure is difficult. One way to reach this is to produce, e.g., Si/Ge heterostructures, which are subsequently cut by a focused ion beam (FIB), to be finally imaged by SEM. This challenging approach, carried out by Bauer *et al.* [103], allows to observe the shape of interfaces inside the structure. The simulation makes the investigation of this property more easily accessible. In Figure 5.11 **c** the experimental and the simulation result are compared with each other. The simulation reveals that at the beginning of growth, the interface shape mimics the shape of the seed point. At later growth stages, it is quite flat in the middle, but shows a large curvature at the edge, which can be explained by particles traveling in the mentioned alleys onto deeper located nanostructure sidewalls. As a consequence of this observation, defining well-defined and flat interfaces inside of honeycomb structures might be a challenging task.

5.4.2 Influence of beam divergence on shadow nanosphere lithography

As demonstrated in the previous section, NSL is a practical tool to produce periodical patterns on substrates. Evaporation techniques are usually used for this method, whereas typically a honeycomb pattern consisting of triangular pyramids is formed. Figure 5.12 **a** shows a tilted SEM view of such a pattern. To gain access to more and to compound materials for the seed formation, one NSL sample was deposited by ion-beam sputtering. Instead of the expected seed pattern, a smooth thin film with hexagonal holes was obtained. In Figure 5.12 **b** a SEM image of this film is presented. As not all PS spheres were removed after the deposition process, it can be seen that the hexagonal holes are located at the positions, which were shielded by the spheres during deposition. The question arises, why pronounced seed points fail to appear. With the on-lattice deposition,

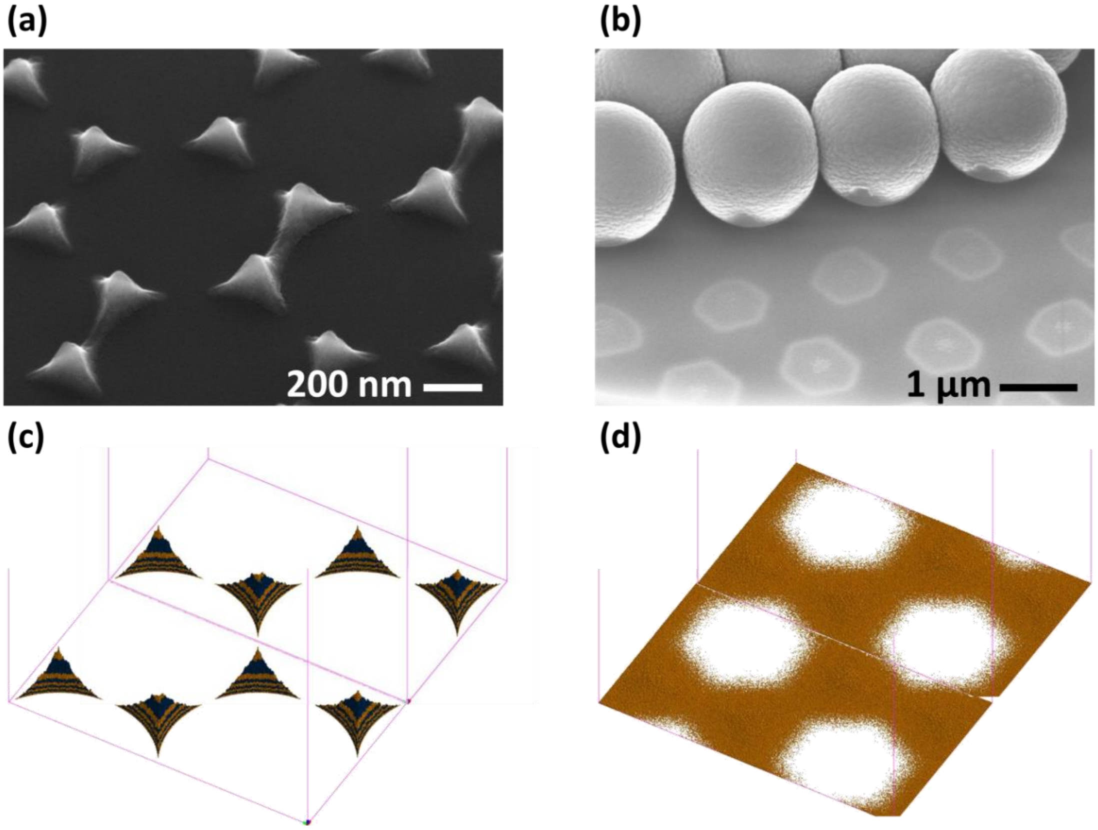

Figure 5.12: Tilted SEM view of (**a**) e-beam deposited and (**b**) ion beam sputtered Si seeds. In (**b**) not all of the PS spheres (PSS) were removed after deposition. (**c**), (**d**) simulated deposition with beam divergence $\Psi = 0°$ and $\Psi = 90°$, respectively. The simulation cell is shown doubled for better orientation.

it becomes possible to prove that the larger beam divergence in the sputtering case inhibits the formation of isolated, exalted seed points.

Beam divergence was introduced to the on-lattice simulation by randomly choosing the angle of incidence θ in the interval [0°; $\theta_{\max}$] and the azimuthal angle Φ in the interval [0°, 360°], after each deposition event. Then, the beam divergence Ψ can be defined to be equal to $2\theta_{\max}$, as this is the maximum angle between the incoming particles. Notice that in real deposition applications, the material flux would not be equally distributed, but rather would show a method dependent distribution. To mimic the monolayer of PS spheres on the substrate, large spherical volumes with a diameter of d_{PSS} atop a flat substrate layer were declared as additional substrate so that material can stick on it. After the simulated deposition, the particles sticking on these spherical volumes were removed, yielding only the particles that are attached to the flat substrate. Figure 5.12 **c** and **d** demonstrate the results of this approach for a beam divergence of 0° and 90°, respectively. The morphology of the simulated films fits quite well to the experimental findings.

An important value of pre-patterned substrates is the seed height h, as it defines – together with the seed spacing – the minimum angle of incidence θ_{GLAD} to avoid inter-

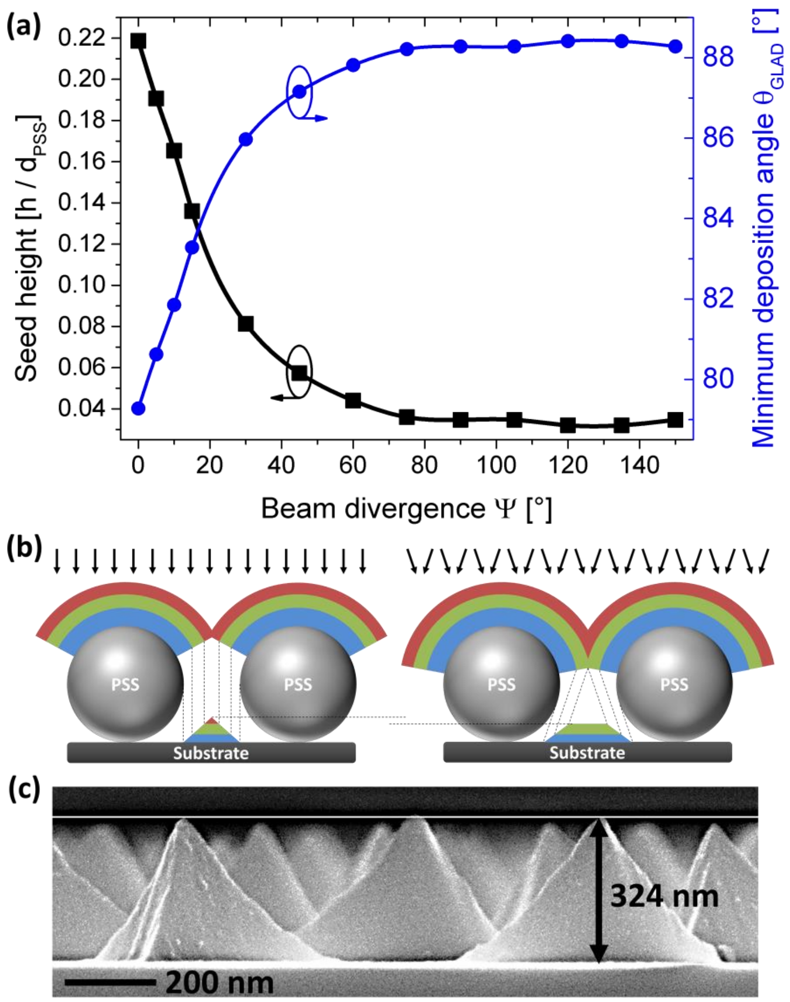

Figure 5.13: (**a**) Dependency of the relative seed heights on the beam divergence. The corresponding minimum deposition angle for GLAD on such seeds is given by $\theta_{GLAD} = \arctan(2d_{PSS}/\sqrt{3}h)$. (**b**) Schematic illustration of the influence of beam divergence on the seed height and width. (**c**) High-magnification SEM image of e-beam deposited Si seeds. The sharp tips on the seeds imply a relatively small beam divergence.

seed growth. In Figure 5.13 **a**, the maximum reachable seed height h for different beam divergence values Ψ, as well as the minimum GLAD deposition angle θ_{GLAD} are presented. These values are obtained from the on-lattice simulation, where the fan angle φ was 27°. For an absolutely parallel particle beam ($\Psi = 0°$), the maximum reachable seed height is 0.219 times the diameter of the used spheres. It drops rapidly with increasing beam divergence, reaching values lower than $0.1 \cdot d_{PSS}$ at $\Psi \approx 23°$, thereby ruling out the possibility to use many sputtering techniques for NSL. This is not only caused by the decreasing seed height with respect to the substrate level, but also by the broadening of the seed structures, leading to the loss of the pronounced point-like hillocks that are necessary for controllable GLAD growth. Figure 5.13 **b** illustrates the influence of a broader incidence angle distribution on the evolution of the seeds during growth. Figure 5.13 **c** depicts a higher magnification of e-beam evaporated Si seeds. The measured height

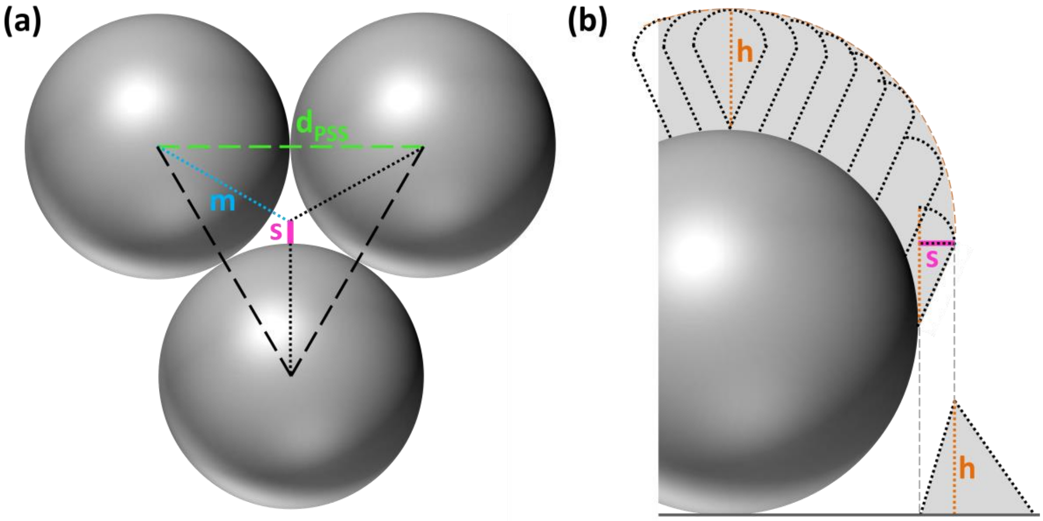

Figure 5.14: Schematic top-view (**a**) and side-view (**b**) on the geometry of the close-packed sphere layer. As soon as the in-plane radius of the sphere has risen by a certain value of *s*, the growth of the seed stops.

of the seed points is $h \approx 324$ nm and the used sphere diameter was $d_{PSS} = 1.59$ µm, corresponding to a ratio of 0.204.

To verify the simulation results, the maximum reachable seed height h for $\Psi = 0°$ is calculated. The growth of the seeds stops, when the space between the spheres is filled, so that no further material can pass. Using the notation from Figure 5.14, this happens when the in-plane radius of the spheres $d_{PSS}/2$ is enlarged by an amount s. With $s = m - d_{PSS}/2$ and the evident relation

$$m = \frac{d_{PSS}}{2\cos 30°}, \tag{5.4.1}$$

one finds

$$s = \frac{d_{PSS}}{2}\left(\frac{1}{\cos 30°} - 1\right). \tag{5.4.2}$$

From the earlier made observation, that the growth front of the fan structures can be approximated by a half sphere, the following relation for its height h and its lateral extension s (see Figure 5.14 **b**) is given:

$$h = s\left(\frac{1}{\tan\varphi} + 1\right), \tag{5.4.3}$$

where φ denotes the fan angle. That means that if a thickness of h is deposited onto a sphere, the in-plane radius of it is increased by s. Finally, combining both equations yields the searched relation:

$$\frac{h}{d_{PSS}} = \frac{1}{2}\left(\frac{1}{\cos 30°} - 1\right)\left(\frac{1}{\tan\varphi} + 1\right) \tag{5.4.4}$$

Taking the fan angle from the on-lattice simulation $\varphi = 27°$, the maximum seed height would be $h\,/\,d_{PSS} = 0.229$, which is close to the value of 0.219, as found in the simulation (see Figure 5.13 **a**). Taking $\varphi = 24°$ – the fan angle of Si – the maximum seed height would be 0.251, which becomes 399 nm for $d_{PSS} = 1.59$ µm. The fact that the actual value is just 324 nm demonstrates the impact of even small beam divergences. Moreover, an additional conclusion is that the increased particle energy in sputter deposition seems to have only minor influence, since the observed results can be explained completely as a consequence of beam divergence.

5.4.3 Influence of beam divergence on oblique deposition

The previous observations point out the importance of taking the effects caused by beam divergence into account. To do this for OAD, at first the influence on fan structures shall be investigated. For this purpose, fan structures were deposited at various beam divergences and the corresponding fan angles were measured. With larger divergences, this becomes increasingly inaccurate, since defining a straight perimeter of the fan structures becomes difficult. Whereas for small divergences, the sidewalls of the fan structures are shadowed by the higher parts of the fan, at enlarged divergence values, material can reach these areas and cause a significant roughening. This leads to an enlarged measurement error.

The change of the obtained fan angles is presented in Figure 5.15 **a**. As long as the beam divergence is smaller than two times the fan angle ($\Psi < 2\varphi$), exclusively the top growth front is hit by the incident particles, leading to a minor increase of the fan angle. For larger divergences, broadening of the fan structures is caused by direct deposition of material onto the sidewall, hence leading to a strong increase of the fan angle.

As indicated in section 4.4, beam divergence has also a strong impact on the OAD thin film morphology. To study this, two simulations were carried out. One with a beam divergence of $\Psi = 40°$ (so $50° < \theta < 90°$) and a second one without beam divergence and $\theta = 80°$ (to yield a comparable structure tilt angle). Figure 5.15 represents the complete

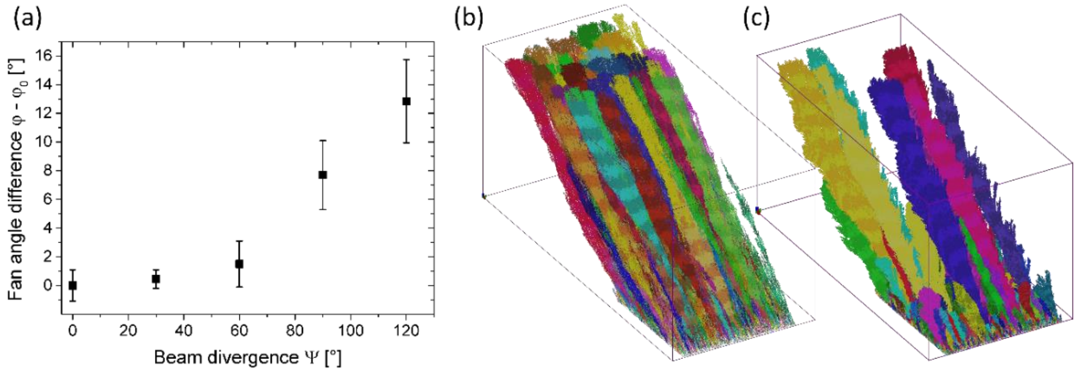

Figure 5.15: (**a**) Dependency of the fan angle from the beam divergence. (**b, c**) Simulations of OAD without and with beam divergence, respectively. The simulation cell had the dimensions 3000 × 3000 × 4000 lattice points, and R = 3 cluster particles were used. After the simulation, the boundary conditions were removed mathematically.

simulations cells for both cases. Each nanostructure is associated with a certain color. The effects of the periodic boundary conditions are removed, to observe the structures as in the real deposition. With beam divergence, the surface consists of fewer structures than in the parallel flux case. For a more detailed investigation thin slices of the simulation cell are compared to experimentally observed SEM images in Figure 5.16. Both films mimic their real counterparts. Without beam divergence, thin nanostructures grow that show little broadening. With beam divergence, most of the structures stop growing, so that only a few structures survive the competition process. The mechanism causing this is already discussed in section 4.4 and can be observed in the simulation as well.

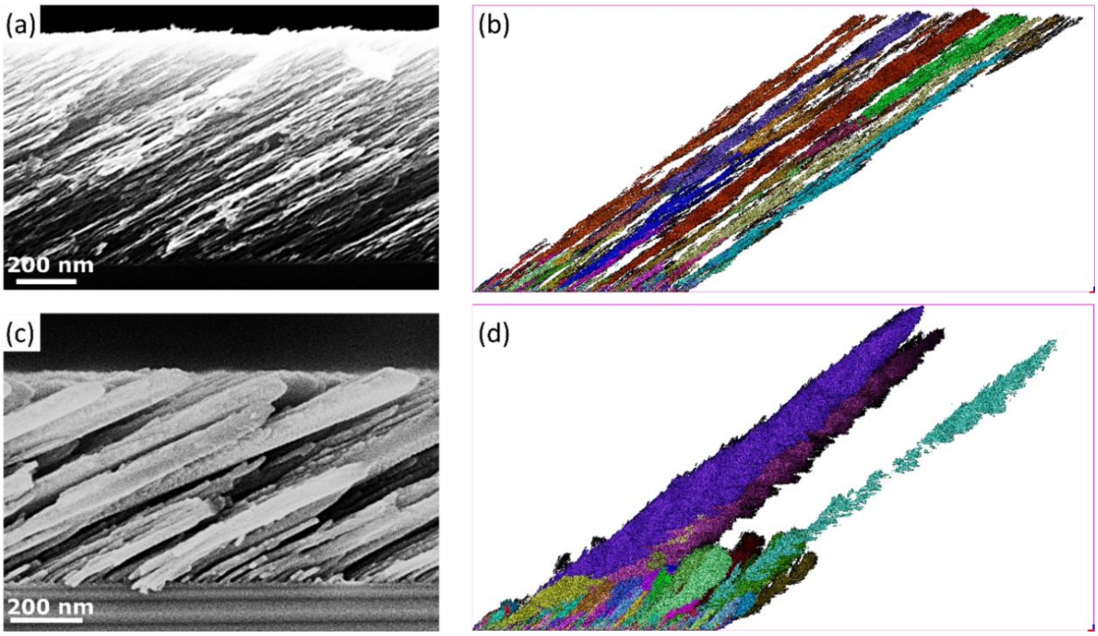

Figure 5.16: (**a**) and (**c**) show side-view SEM images of obliquely deposited thin films, without and with beam divergence, respectively. (Same images as in Figure 4.12.) (**b**) and (**d**) depict slices of the corresponding simulations, revealing a comparable morphology.

5.5 Other aspects

Many of the code details of the simulation shall not be discussed here, as they are mainly of technical nature. This includes trivial tasks, like the extraction of densities, the insertion of different substrate geometries, writing, and reading of data- and info-files and so on. More complex mechanisms in the simulation code, like the utilization of a wrapper class to allow parallel write access to the simulation cell (which is not possible for the standard container *std::vector<bool>*, for example) are not novel. Nevertheless, two aspects are worth to be discussed. These are the algorithms of visualization and diffusion.

5.5.1 Visualization

Investigating the morphology of the simulated GLAD films requires a way to create a visual impression of the particles in the simulation cell. Usual render software (as the ray tracer POV-Ray [104]) is often more focused on realistic image generation and lacks of the ability to work with more than ~10^6 objects in a single scene [105]. The probably most popular visualization tool for simulation data, Ovito [106], is limited to render ~10^9 objects in a single scene and allows working with larger amounts of particles just as recently as May 1st 2018 (development version). As it is the aim of the developed simulations to work with 10^{10} particles and more, visualization had to be implemented in an extra software module.

Rendering, and especially shading, in computer graphics is done typically by iterating over all pixels of an image. That means that for each individual pixel (or ray in ray tracing) all objects are queried. If an object lies on that specific pixel (or is intersected by the ray), the distance to the screen (or camera) is calculated. Finally, for the object that is closest to the screen, the illumination is calculated, and it is then assigned to that pixel.

This procedure is unnecessary slow for large amounts of particles. As the file with the particle coordinates is typically exceeding the capacity of the available fast RAM, it has to be stored on the much slower HDD. Consequently, with the usual approach the complete file has to be slowly read millions of times (= number of pixels), to create the complete image. To avoid this, the used visualization module reverses this process. The large file that contains the particles is accessed only once here. For each extracted particle coordinate, the position on the screen is calculated – which is trivial for spherical particles and an orthographic perspective. Then, on the found positions, the distance to the screen is calculated, and if this distance is smaller than the already saved one, the particle is inserted at this pixel similar to a classic z-buffer approach. To provide a more ‘realistic’ image, for each pixel the surface normal (as two angles) of the spherical particle at the position of the pixel is saved. After this is done for all particles, each pixel of the image contains three values: the distance to the screen and two angles. Utilizing the Phong reflection model [105], the brightness of each pixel is calculated from these two angles.

This process allows the creation of images in quite a short time on the one hand, but also shows realistic spheres, if the image is magnified strongly.

The color of each sphere can be assigned by selected properties, e.g. the distance to a specific point or plane, the corresponding cluster or simply represent the time evolution (as usually done in this work). To create the illusion of depth, particles that have a larger distance to the screen can be drawn darker, as for example in Figure 5.7 **d** - **f**. The abilities to create image sequences (Figure 5.17 **a** - **c**), cut out defined slices (**d**), and to magnify specific regions (**e**) completes the palette of visualization tools.

Another advantage of that approach is that many images (views, slices…) can be generated in parallel during one iteration run over the data file. Furthermore, this permits the simple realization of animations. The disadvantage – and the reason why this way is not chosen in normal image rendering – is that global illumination (e.g. shadows) cannot be computed in a single run, as the spatial relation between all objects – also the not drawn ones - had to be known.

5.5.2 Surface diffusion

As it influences the fan angles, tilt angles, densities and the local crystallinity, surface diffusion plays an outstanding role for the formation of GLAD and OAD films. A realistic reproduction of surface diffusion requires complex mechanisms and is usually handled with molecular dynamics or monte-carlo methods. Imitating surface diffusion in a ballistic simulation requires a simplification. In on-lattice simulations, for instance, diffusion is often mimicked by the following procedure: after a particle has reached the surface of the growing film, other particles in the vicinity of the collision point are allowed to jump into other positions, if this increases their coordination number (used, e.g., by Tanto *et al.* [93]). While this procedure leads to a massive compactification of the simulated film and is easy to implement, it has two major disadvantages. The first one is that, depending on the exact realization of this algorithm, opposite results can be obtained. Tanto *et al.* observed a reduction of the fan angle with increasing diffusion, whereas Saito *et al.* [107] found the fan angle to increase with stronger diffusion. The second disadvantage of this algorithm is that the positions of the previously deposited particles have to be known, which is not the case in the presented simulation (as only the forbidden volume is saved).

Consequently, it is only possible to let the actually incoming particle move to a more favorable position. To realize that, the simplest approach would be to move the particle to the position with the highest coordination number in the neighborhood of the collision point. This position can be found by counting the number of forbidden grid points in a

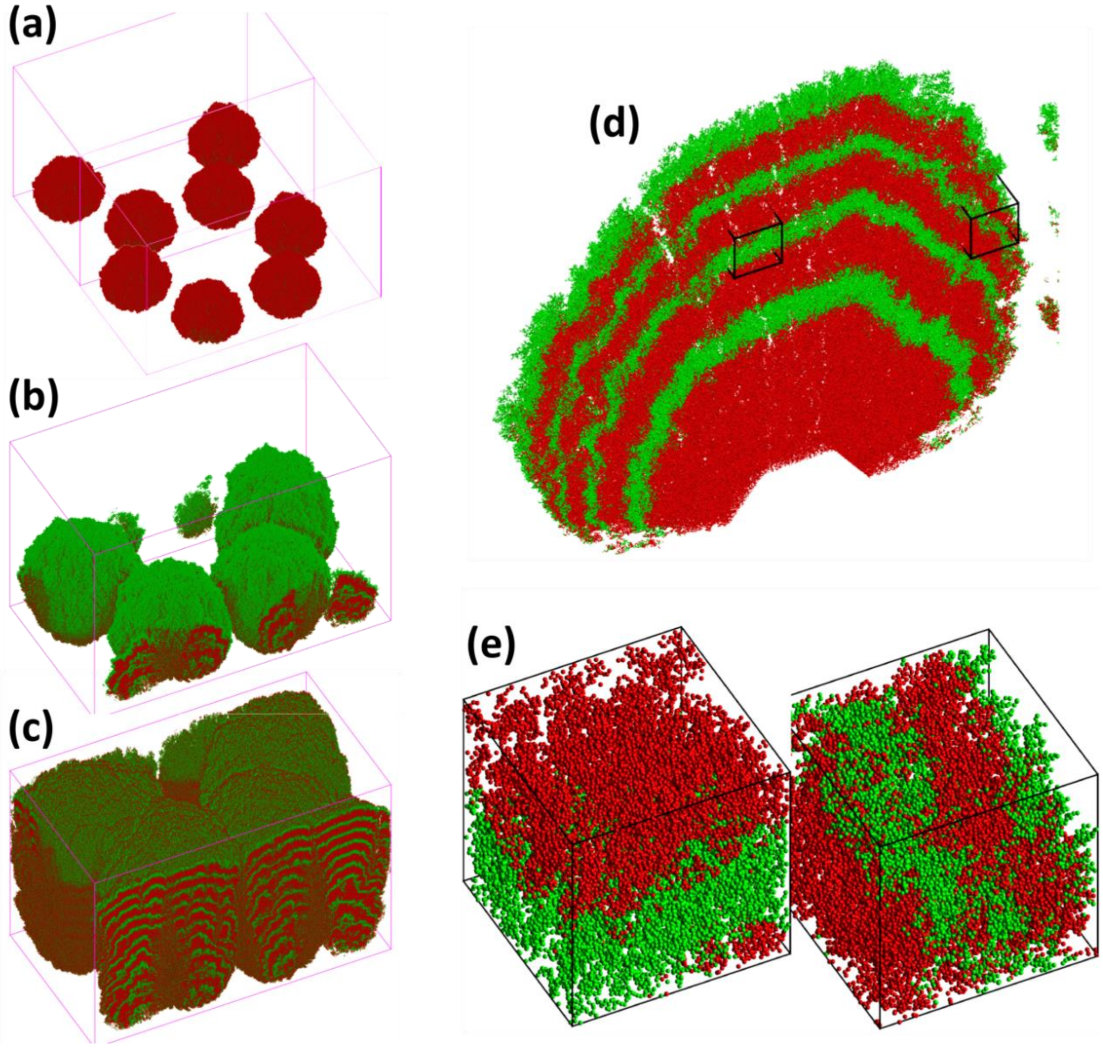

Figure 5.17: Illustration of temporal and spatial selection during visualization. (**a**), (**b**), and (**c**) demonstrate the growth of upright nanostructures on a honeycomb pattern at different times. (**d**) Thin slice, cut out of image (**b**). (**e**) Magnification of the two areas, marked in (**d**).

defined volume around the position. Parameters to adjust the strength and character of the diffusion are the maximum allowed jump distance, the jump probability, the size of the volume used for coordination calculation and the maximum number of subsequent jumps for each particle.

This procedure was implemented and studied for some selected examples. It was found that the fan angle decreases with increasing strength of the diffusion, which is the same behavior as observed in the experiments. For OAD with diffusion, the following film morphology was found: At the beginning, a closed layer forms on top of the substrate.

The roughness of this layer increases until shadowing becomes strong enough to separate individual structures. Comparable to the experimental observations, the structures are well separated along the incidence direction, but are interconnected perpendicular to this (compare Figure 5.18).

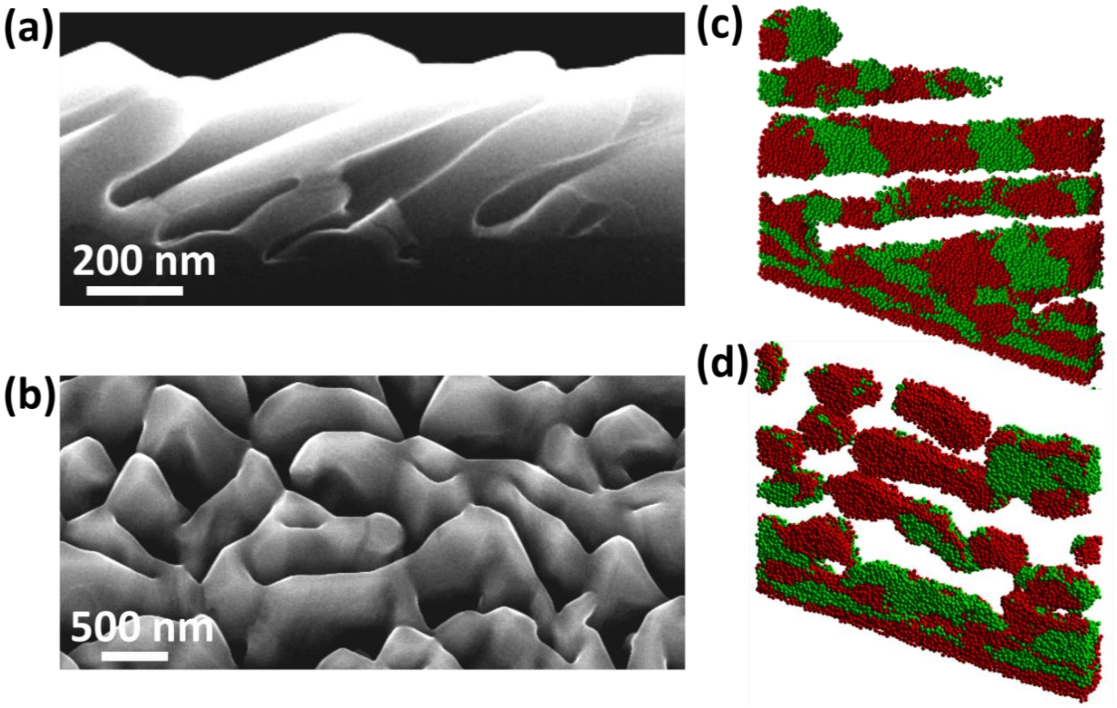

Figure 5.18: SEM cross-section (**a**) and top view (**b**) image of Germanium, obliquely deposited onto a Si substrate at 300 °C. The structures are well separated along the incidence direction of the particles, but merge in perpendicular direction. A cut through a simulated OAD film, deposited with surface diffusion, along the incidence direction (**c**) and perpendicular to this (**d**), shows a similar morphology.

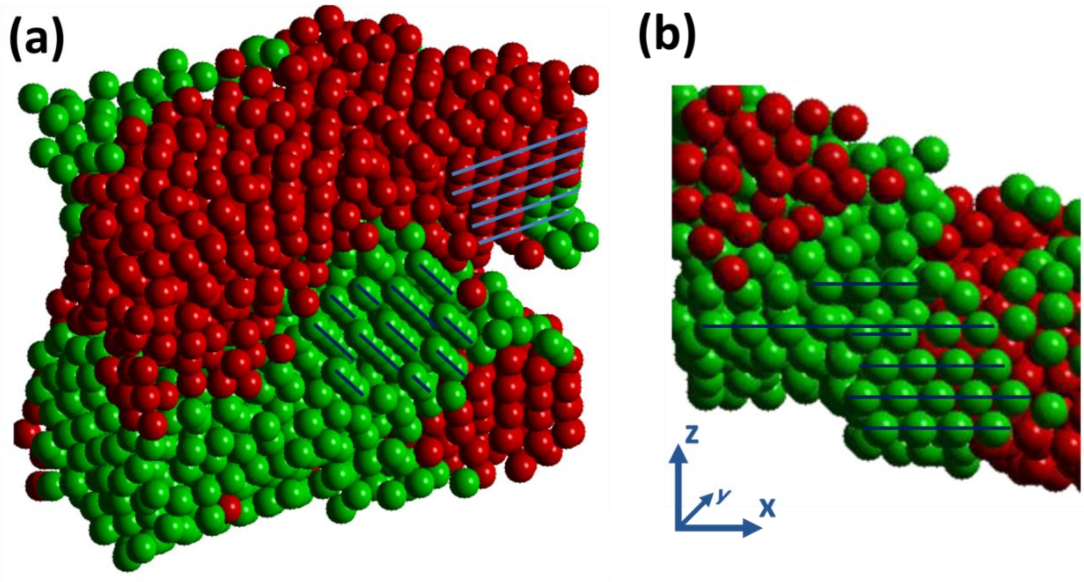

Figure 5.19: (**a**) Hexagonally close packed particle assemblies can be found in simulated films, deposited with strong surface diffusion. (**b**) The symmetry axes of these assemblies are always oriented along the cell axes, representing another kind of the 'grid effect'.

For strong diffusion settings, highly ordered, hexagonally close packed, crystal-like regions can be found in the deposited material, as illustrated in Figure 5.19 **a**. However, a closer inspection of these ordered regions reveals a major problem, which led to the decision to discard this approach. As demonstrated in Figure 5.19 **b**, the particles organize themselves in a way that the crystal axes are aligned with the cell axes. Due to the selection of the positions with the highest coordination, the discrete nature of the simulation cell favors certain spatial particle-particle relations. This can be interpreted as another kind of 'grid effect'. No parameter set that avoids this behavior was found.

Finding and characterizing a completely isotropic surface diffusion algorithm appears to be quite challenging and lies beyond the scope of this thesis. As starting point for future research, the following approach could serve: Instead of finding the position with the maximum number of neighboring forbidden points, one could try to classify the local surrounding of a selected point, to decide if it is in the vicinity of one, two, three, or more other particles. This classification has to be independent from the exact angular relation with respect to the cell axes. A robust testing scheme to characterize the resulting films should also be established, as the grid effect may not be as obvious as in the presented example.

5.6 Summary

In this chapter, modelling of OAD and GLAD growth by computer simulations was investigated.

- An off-lattice simulation was used to investigate the growth of fan structures and oblique deposition. The general morphology of the experimental findings can be reproduced. This type of simulation is limited to deposition cases with a fixed incidence direction.
- On-lattice simulations allow to change the direction of the incoming particles during deposition, enabling the simulation of GLAD and beam divergence. For simple cubic particles, an artificial anisotropy – the grid effect – exists, influencing the simulated tilt angles and densities. The use of cluster particles reduces this effect and makes the simulations nearly isotropic. Using a geometric optimization, utilizing the forbidden volume approach, allows simulating quite large systems.
- The growth of upright nanostructures on a honeycomb pattern, as well as the influence of beam divergence in different deposition cases was studied.
- If surface diffusion is to be implemented, care has to be taken to avoid the introduction of a new grid effect.

The results, presented in this chapter, were previously published in [108].

6 Oblique Angle Deposition Model

6.1 Semi-Empirical models

The observation that the columns are tilted into the direction of the incoming particle flux is not surprising, but the fact that this column tilt angle β is always smaller than the vapor incidence angle θ lead to the development of numerous models in the past decades. In early models, a fixed relation for the angles β and θ is assumed. This means that neither material properties nor deposition parameters are taken into account. The most popular models are the tangent rule [28] and the cosine rule [18] (also known as Tait's Rule). The tangent rule

$$\tan\beta = \frac{1}{2}\tan\theta \tag{6.1.1}$$

estimates the tilt angles more appropriate for small vapor incidence angles, whereas the cosine rule

$$\beta = \theta - \arcsin\frac{1-\cos\theta}{2} \tag{6.1.2}$$

gives better estimations for the highly oblique deposition regime. In Figure 6.1 the predictions of the tangent and the cosine rules are illustrated, together with the results measured for the oblique deposition of silicon. As shown earlier (chapter 4), material, substrate temperature, and particle flux divergence, for instance, influence the actual tilt angle. Hence, at least one mathematical parameter has to be included into the β-θ-relation. For this purpose, Hodgkinson *et al.* [109] used a parametric version of the tangent rule:

$$\tan\beta = E\tan\theta \tag{6.1.3}$$

In this equation, E is a fitting parameter that cannot be connected to physical properties directly. In a continuum approach Lichter and Chen [110] found the following relation:

$$\beta = \frac{2}{3}\frac{\tan\theta}{1+\chi\tan\theta\sin\theta} \tag{6.1.4}$$

Hereby, the parameter χ depends on the deposition rate J, the adatom diffusion coefficient D and the height of the initial shadowing features h_i in the following manner:

$$\chi = \frac{4}{27}\frac{h_i J}{D} \tag{6.1.5}$$

A drawback of this approach is that the surface diffusion coefficient is difficult to determine and that it depends on various other parameters, as the actual crystal plane or the surrounding gas pressure. A similar ansatz is used by Alvarez *et al.* [111]. In their model, the particle beam divergence and a sticking coefficient are considered. Especially this sticking coefficient is a quite uncertain parameter, as it cannot be measured directly. Similar approaches exist for other film properties. Poxson *et al.* [68] derived a model for the film porosity P using a fitting parameter c that cannot be linked with observable quantities:

$$P = \frac{\theta \tan\theta}{c + \theta \tan\theta} \tag{6.1.6}$$

In summary, the mentioned models introduce at least one parameter that has to be obtained by fitting the model on measured properties of obliquely deposited films over a wide range of vapor incidence angles. The obtained parameters are difficult to correlate with material properties or deposition conditions.

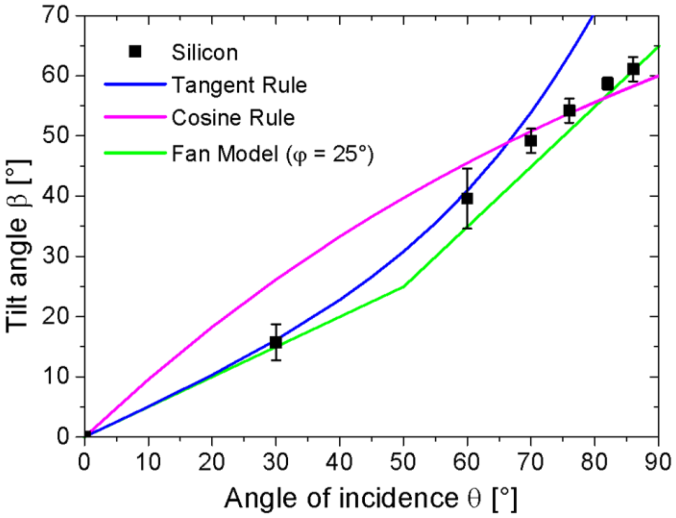

Figure 6.1: Tilt angle β vs. angle of incidence θ. The tangent and the cosine rules as well as the prediction of Tanto's fan model are shown. For comparison the here experimentally observed values for silicon are displayed, too.

6.2 Tanto's fan model

The growth mechanics in oblique angle deposition can be separated into two different processes. The first process is the long range self-shadowing effect that determines the overall morphology of the growing thin film, e.g. the formation of columns. The second process is more localized at the vicinity of the point where the particles hit the substrate and determines the microstructure. It is essentially similar to normal deposition. The idea of separating these two processes serves as starting point for the development of the fan model. In such a fan model, the ballistic shadowing effect is seen as a purely geometrical, material independent process, whereas the properties of the material and the influence of the deposition conditions are combined into a single parameter: the fan angle.

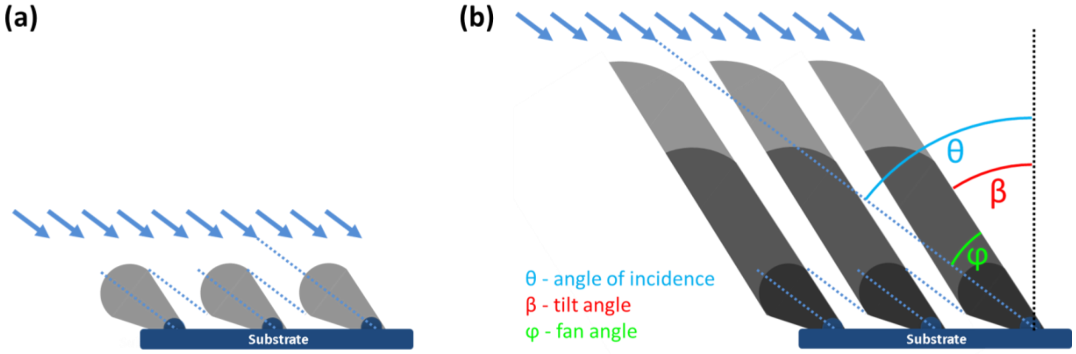

Figure 6.2: Sketch of Tanto's fan model. The substrate is idealized as a row of seed points in an oblique, parallel particle flux (blue arrows). (**a**) First growth stage, before shadowing starts. (**b**) Fully developed nanostructures, whose tilt angles are defined by the upper edges of each fan.

If material is deposited onto sharp edges, overhang structures grow (see section 4.3). Due to the visual similarity to a fan, overhang structures grown on isolated seed points are called fan structures. The reason for this overhang growth is the non-central sticking of the particles. The center axis of a fan structure points always against the direction of the incoming particle flux. The angle by which the edge of such a freestanding overhang structure grows away from the direction of the incoming particle flux is called fan angle φ. Notice, that Tanto defines the 'fan-out angle' Φ, as the opening angle of the compete fan [70], whereas here the half of this value $\varphi = ½\Phi$ is used for simplicity. Van der Drift [22] was the first to point out the significance of the competitive selection of such fan structures for the morphology evolution of growing thin films. Ramanlal and Sander [88] investigated the growth of isolated fan structures by a 2D computer simulation and a continuum model, concluding, that the shape of the growth front of fan structures does not change if the distance to the starting point has become large enough. However, linking fan structures to the growth of OAD nanostructures was done as recently as 2010 by Tanto *et al.* [70] – more than 40 years after the tangent rule was proposed. Tanto's original fan model should shortly be presented in the following.

In this model (see Figure 6.2), the substrate is defined as a row of isolated seed points in a parallel flux of material. If material is deposited onto this substrate from a non-perpendicular direction, individual fan structures start to form on each seed point, growing against the direction of the incoming material. After a specific point in time, the upper edges of the fan structures start to cast shadows on the lower edges of the behind standing fans. Therefore, no further material can reach the lower parts of the fan structures, which consequently stop to grow. The shadow casted by the upper, non-shadowed edge of the fan structures forces the lower edges to grow parallel with the upper edges. Because the angle by which this upper edge grows away from the direction of the incident particle flux is the fan angle φ, the tilt angle β of the finally arising nanostructure is defined by the following simple equation:

$$\beta = \theta - \varphi \ , \tag{6.2.1}$$

which is stated to be valid for $\theta > 2\varphi$. For smaller incidence angles the obliquely growing fans are assumed to merge (for the detailed calculation see ref. [70]), leading to the relation:

$$\beta = \theta - \arctan \frac{\sin(2\varphi) - \sin(2\varphi - 2\theta)}{\cos(2\varphi - 2\theta) + \cos(2\varphi) + 2} \tag{6.2.2}$$

Comparing the results from this equation with the experimental observations shows that the calculated tilt angles are in the correct order of magnitude, but that the exact dependency does not fit the experimental findings (see Figure 6.1). Another unsatisfying result of this model is the occurrence of an odd kink in the β-θ-relation at $\theta = 2\varphi$.

6.3 Development of the Competition Model

A closer look on the interaction of neighboring fan structures reveals that some of Tanto's assumptions are too simple. Such a fan structure is not only defined by the fan angle, but also by the curved shape of its growth front. From section 4.3 and 5.2, it is known that the growth front can be approximated spherically in good agreement with the findings from experiment and simulation. The shape of the growth front defines an 'isochrone' surface for each point in time of the fan growth. If surface diffusion is limited, shadowed parts of the fan structures will stop to grow, while the non-shadowed parts further follow the near spherical behavior. Taking a more detailed view on the time evolution of interacting fan structures shows that the shadowing of a fan's lower part does not force its lower edge to grow parallel with the upper edge that casts the shadow. Therefore, after some time, the shadowed lower edge of each fan encounters the shadow-casting upper corner of the front-standing fan. The growth competition between these both edges defines the long-time behavior of the growing film. Consequently, the growth process on a tilted row of isolated seed points can be divided into three stages, as depicted in Figure 6.3.

As in the original fan model, in the **initial stage (I)** fan growth starts on each seed point, whereas the fans are tilted into the direction of the incoming material flux. The local tilt angle of the nanostructures is therefore $\beta_I = \theta$. This stage lasts, until the upper edges of the fan structures start to cast shadows onto the structures located behind them.

When this happens, the shadowed lower parts of the fan structures become shadowed continuously and consequently stop to grow. The upper part is not shadowed during this **transition stage (II)** and thus grows away from the direction of the material flux with the fan angle. Hence, taking this angle as the local tilt angle during this stage, Tanto's relation $\beta_{II} = \theta - \varphi$ is found. As the growth continues, and accordingly the shadowing progresses, the evolving shape of the lower parts of the fans depends tightly on the shape of the growth front. From the assumption of a spherical growth front, it can be concluded that for all possible incidence angles, the fan structures eventually will start to merge. That means that the shadowed, lower part of each structure approaches the upper corner of the front standing fan. This behavior can also commonly be found in experiments for thin films that were obliquely deposited onto a periodic pre-pattern.

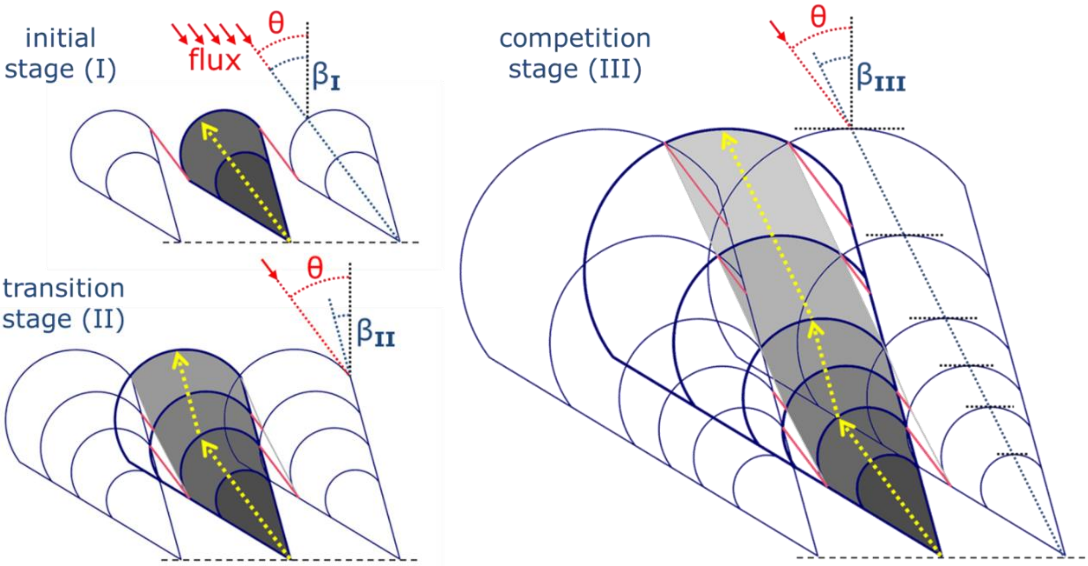

Figure 6.3: Scheme of the three growth stages in the competition model. The yellow arrows represent the local growth direction of each stage. In the **initial stage (I)** the fan structures start to grow into the direction of the incoming particle flux on each individual seed. When shadowing starts to inhibit the growth of the lower parts of the fan structures, a **transition stage (II)** begins. During this stage, the shadowed lower corner grows progressively into the direction of the corner that casts the shadow. At the end of this stage, shadowing is reversed so that the rear-standing column starts to partly shadow the top edge of the front standing one: the **competition stage (III)** has begun. Both corners of each structure therefore grow parallel then, and therewith define the final growth direction of the whole nanostructure. As only the point with the highest distance to the substrate never becomes shadowed, it can be used to calculate the tilt angle of the complete structure.

When both, the upper and the lower, corners have merged, they start to compete with each other. As a consequence, the behind standing fan can start to shadow a part of the front standing one, in this **competition stage (III)**. This seems unlikely but can be explained by the oblique arrangement of the seed points, and by this of the fan structures. Due to the fact that the more central parts of the fan structures grow faster than their outer parts (which is evident for the assumed fan shape), the initial separation between the seed points is bridged eventually. That both corners touch each other now is equivalent to the statement that they grow parallel in this stage. The direction of these corners defines the growth direction of the entire column. Instead of calculating the tilt angle of these corners from the dynamics of the interacting growth fronts, a simpler approach is chosen. Obviously, the point of the fan structure that has the largest distance to the substrate can never be shadowed by other structures. Therefore, the connection of this point and of the fan's starting point must be parallel to the corners and therefore shows the same tilt angle as the whole column.

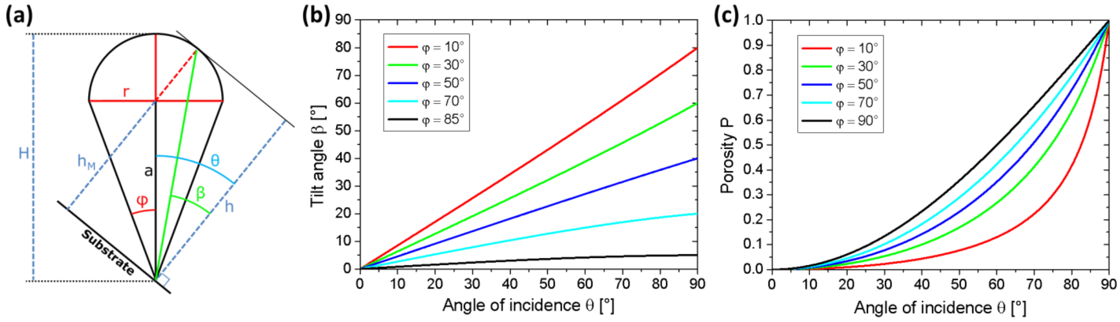

Figure 6.4: (**a**) Sketch of the angles and lengths used in the calculations. For the shown orientation of the fan structure, the incoming particles arrive from the top side. The substrate is tilted by an angle θ and all of the red line segments have the same length r. The green line represents the connection of the fan's origin with its highest point, and thereby the tilt angle β of the final nanostructure. (**b**) and (**c**) illustrate the influence of the parameter φ on the calculated tilt angle β and on the porosity P, respectively.

In order to calculate the morphological properties of the oblique fan structures, the angles and lengths as shown in Figure 6.4 **a** are used. Note that all red lines have the same length, due to the approximation of the spherical growth front. The green line connects the origin of the fan with the point that has the largest distance to the substrate, which is equal to the tilt angle of the whole developing column as derived above. With the given notation, the fan angle φ is given by

$$\tan\varphi = \frac{r}{a} \tag{6.3.1}$$

and the tilt angle follows from the sine law to

$$\frac{\sin\beta}{a} = \frac{\sin(\theta-\beta)}{r} \ . \tag{6.3.2}$$

Combining both equations yields

$$\tan\beta = \frac{\sin\theta}{\cos\theta + \tan\varphi} \ , \tag{6.3.3}$$

which can approximately be linearized to

$$\beta = \left(1 - \frac{\varphi}{90°}\right)\theta \quad \text{for } \varphi \text{ in } [°]. \tag{6.3.4}$$

The equations (6.3.3) and (6.3.4) describe the column tilt angle for the complete range of vapor incidence angles $0° \leq \theta \leq 90°$. The influence of the parameter φ on the tilt angles β is illustrated in Figure 6.4 **b.**

In order to describe the growth rate of the obliquely deposited film (with respect to the growth rate of a film normally deposited under the same conditions), the thickness of the film for an arbitrarily chosen time is calculated. The OAD film thickness here is denoted as h, whereas the thickness of the corresponding normally deposited film is expressed as H (equal to the VTE). This is obvious, as the normally deposited film would be a superposition of vertically standing fan structures so that $h = H$. From Figure 6.4 **a** one finds

$$h = h_M + r = a\ \cos\theta + r \tag{6.3.5}$$

and

$$H = \ a + r \tag{6.3.6}$$

easily. Using equation (6.3.1), the relative growth rate h/H then is given by

$$\frac{h}{H} = \frac{a\ \cos\theta + r}{a + r} = \frac{\cos\theta + \tan\varphi}{1 + \tan\varphi} \ . \tag{6.3.7}$$

Finally, the porosity and therewith the density of an obliquely deposited film shall be calculated. Poxson *et al.* [68] have derived that the porosity and the growth rate of such an obliquely deposited film are linked with each other, under the assumption that the sticking coefficient of the arriving material is equal to one. At least for evaporation onto a non-heated substrate neither sputtering nor reflection nor desorption are expected so that this assumption is sound. Following Poxson, the porosity of the film can be expressed as

$$P \equiv 1 - \frac{\rho_{film}}{\rho_{bulk}} = 1 - \frac{V_{mat}}{V_{film}} \ . \tag{6.3.8}$$

Hereby, V_{film} denotes the total volume of the porous film (film thickness · substrate area) and V_{mat} represents the fraction of the film actually filled with material. The amount of material reaching a tilted substrate is reduced geometrically by a factor of cos θ, compared to normal deposition onto a substrate with the same surface area. Thus, with $V_{mat} = V_{norm} \cdot \cos\theta$, one finds

$$P = 1 - \frac{V_{norm}}{V_{film}} \cos\theta \ . \tag{6.3.9}$$

As for both volumes the same substrate area was assumed, this can be reduced to the film thicknesses. Therefore, the porosity of the film is given by the growth rate h/H and

$$P = 1 - \frac{H}{h} \cos\theta \ . \tag{6.3.10}$$

The influence of the parameter φ on the porosity P is illustrated in Figure 6.4 **c.** Bringing equations (6.3.7) and (6.3.10) together results in the film density

$$\rho_{film} = \rho_{bulk} \frac{\cos\theta + \tan\varphi \cos\theta}{\cos\theta + \tan\varphi} \ . \tag{6.3.11}$$

To conclude, relations for the column tilt angle β (eq. (6.3.4)), the growth rate h/H (eq. (6.3.7)) and the film density ρ (eq. (6.3.11)) are derived. In each of these expressions only one parameter, the fan angle φ is used. In addition, a 'backward shadowing' is proposed that has fundamental impact on the growth competition of the nanostructures.

6.4 Verification of the model

The presented model divides the evolution of the nanostructures into three growth stages. It is not surprising that these stages were not observed by experiments of other researchers before, as they can only be distinguished at the used, idealized substrate geometry of isolated seed points. It is obvious that in the initial stage (I) the lower edge of the non-shadowed fan would grow into the substrate when $\theta + \varphi > 90°$. Furthermore, on a flat and solid substrate nucleation appears equally distributed, so that shadowing acts directly from the start of growth. For the same reason, the transition stage (II) cannot be observed on flat substrates, because also the proposed 'backward shadowing' acts directly from the beginning of growth. Therefore, on flat substrates the tilted columns start directly to compete so that consequently stages (I) and (II) are not observed. However, the transition stage (II) can be observed on pre-patterned substrates. Figure 6.5 **a** shows silicon, deposited obliquely onto a NSL substrate. It can be seen that the structures broaden with increasing height, thereby reducing the space in-between them. This behavior is usually found for the oblique deposition on pre-patterned substrates, see for example also Tanto *et al.* [93].

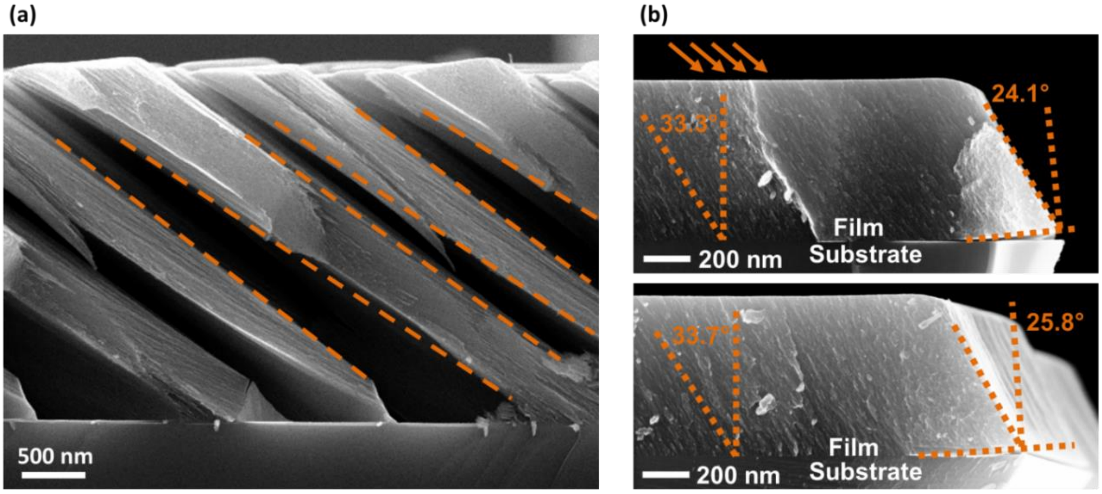

Figure 6.5: (**a**) SEM image of silicon nanostructures, obliquely deposited ($\theta = 80°$) onto a patterned substrate. The dotted orange indicators highlight the converging corners of the nanostructures observed in the transition stage (II). (**b**) SEM images of the rear edge of a substrate at different positions with an obliquely deposited Si film ($\theta = 50°$, $\varphi_{Si} = 24°$). The films slightly peel off from the substrate. Away from the edge, the tilt angle is close to the value predicted by the proposed model for the competition stage (III) ($\beta_{III} = 35.1°$). Directly at the edge, there is no behind-standing partner for the backward shadowing, consequently the outmost structure remains at the transition stage (II) and therefore shows an angle close to $\beta_{II} = \theta - \varphi = 26.0°$.

Another counterintuitive prediction of the model is the 'backward shadowing' – the fact that a behind-standing column can influence a front-standing one. That this really happens can be proven on the rear-edge of a substrate, by investigating the 'last' tilted nanostructure on the substrate. As there is no behind-standing partner, this structure should always remain in the transition stage (II). Hence, it should show the tilt angle β_{II} predicted for this stage, what is exactly what is found in experiment, as shown in Figure 6.5 **b**.

As has already been pointed out above, the three proposed growth stages can hardly be obtained and hence distinguished experimentally. However, a suitable substrate can easily be created in a computer simulation. Figure 6.6 shows an off-lattice simulation of OAD onto four seed points, as they were assumed for the model development.

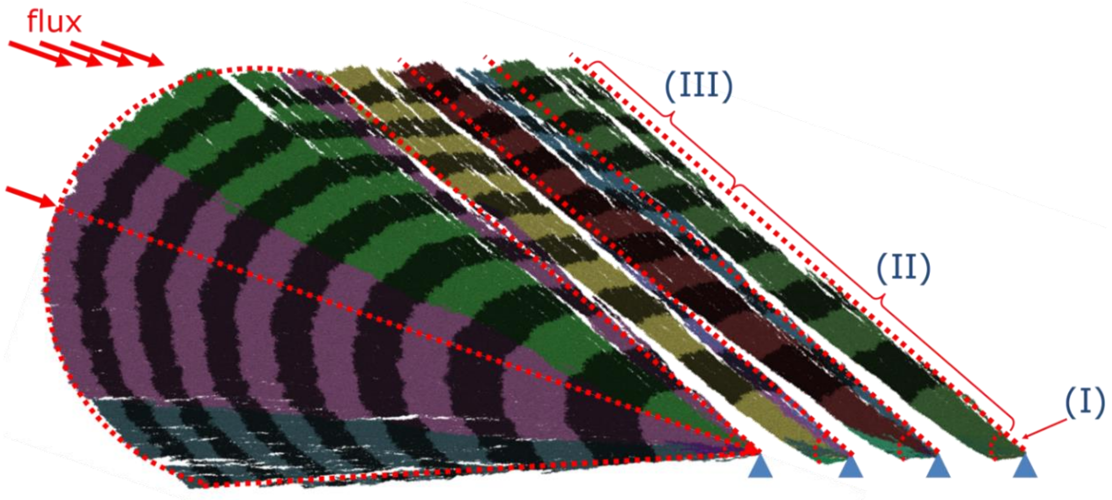

Figure 6.6: Ballistic off-lattice simulation of OAD onto a row of four seed points (located at the top of the blue triangles). The growth stages are indicated. The leftmost seed remains un-shadowed, resulting in the development of a full fan structure. The indicated dotted lines depict the position of the top corners of non-shadowed fans. In the competition stage (III), rear-standing columns overgrow this line. Because the rightmost structure has no partner for backward shadowing, it continues to grow along the hypothetical fan perimeter with β_{II}. Furthermore, it can be seen that the porosity of the outer parts of the fan structure is the origin of the porosity of the final film, after the initially defined space between the structures has vanished.

The depth of the simulation cell was chosen to be small so that a nearly 2D result was obtained. In a full 3D simulation, the in-plane broadening impedes the creation of a clear image of the stages. Notice that the 2D fan angle is smaller than the 3D fan angle. In fact, the simulations indicate that the fan angle approaches continuously the 3D value as the depth of the simulation cell is increased. This observation could bring deeper insights into the growth of ballistic fan structures but was not investigated in detail here.

In the shown simulation, the three growth stages can clearly be distinguished. The above made observations for real depositions can be noticed here, too. In the transition stage (II), the space between the nanostructures decreases. Furthermore, the right-most structure has no partner behind it so that it encounters no 'backward shadowing'. Consequently, it remains in growth stage (II) and therefore continues to grow with β_{II}. Another possibly upcoming question can be answered from the simulation. In the model, the fan structures coalesce so that in the simple model drawing, the OAD film seems to be dense and closed in the competition stage (III), which contradicts the experimental observations. From the image of the simulation, it can be concluded that the porosity in the final growth stage arises from the inner porosity of the outer parts of the fan structures. So even after the initial spacing – defined by the arrangement of the seeds – has vanished, the film still is highly porous.

In addition, numerical predictions for the column tilt angle β (eq. (6.3.4)), the growth rate h/H (eq. (6.3.7)) and the film density ρ (eq. (6.3.11)) can be deduced from the presented model. For this only a single parameter, the fan angle φ is used. To verify the model, these predictions are tested for Si, Ge and Mo, which were obliquely deposited by e-beam evaporation onto substrates held at room temperature. These materials were chosen to cover a wide range of melting points: Ge ($T_M \approx 940$ °C), Si ($T_M \approx 1410$ °C), and Mo ($T_M \approx 2620$ °C). The melting point is assumed to be connected to the value of the fan angle [71]. Furthermore, Si and Ge grow amorphous at room temperature, while Mo shows the formation of single crystalline nanostructures, which form a biaxially textured film [39, 62]. Additionally, the model predictions are tested for the results of the off-lattice simulation.

The results of these depositions, as well as the fitted model curves are presented in Figure 6.7. Shown are the individually fitted values (black and blue) and the model predictions, where the measured fan angles were used as input (red). The overall dependency of the tilt angles as well as the film thicknesses (derived from the growth rate) and the film densities is described very well by the model. The difference of the fitted and the predicted fan angles is rather small and can easily be attributed to measurement uncertainties. The predicted densities fit quite well, too. A small deviation can be found for the predicted growth speeds at highly oblique incidence angles. An explanation could be that in this incidence angle region, the nanostructures are formed by the outer parts of the fan structures. As these structures carry an inherent porosity at their perimeter (see above), the nanostructures inherit this property. The structures (especially for the amorphous Si and Ge) therefore are expected to show this internal porosity as well. If this were the case, the same amount of material would need more space to be stored. Consequently, the realized film thickness is slightly higher than predicted by the model.

Finally, the model is tested for various compound materials, taken from literature. For example, tilt angles of MgF_2 nanostructures for the complete angle of incidence range have been reported by Tait *et al.* [18] and Messier *et al.* [65], as shown in Figure 6.8 **a**. The values of these two groups fit quite well and confirm the predicted quasi-linear behavior. Alvarez *et al.* [111] provide tilt angles for Ta_2O_5, SiO_2 and indium-tin-oxide (ITO) at highly oblique incidence angles. These values do also follow the linear behavior quite well (Figure 6.8 **b)**. Porosity data were, e.g., measured by Poxson *et al.* [68] for SiO_2 and ITO with optical methods. These data can be described properly with the model (see Figure 6.8 **c** and **d**). As none of these authors has measured the fan angle directly it

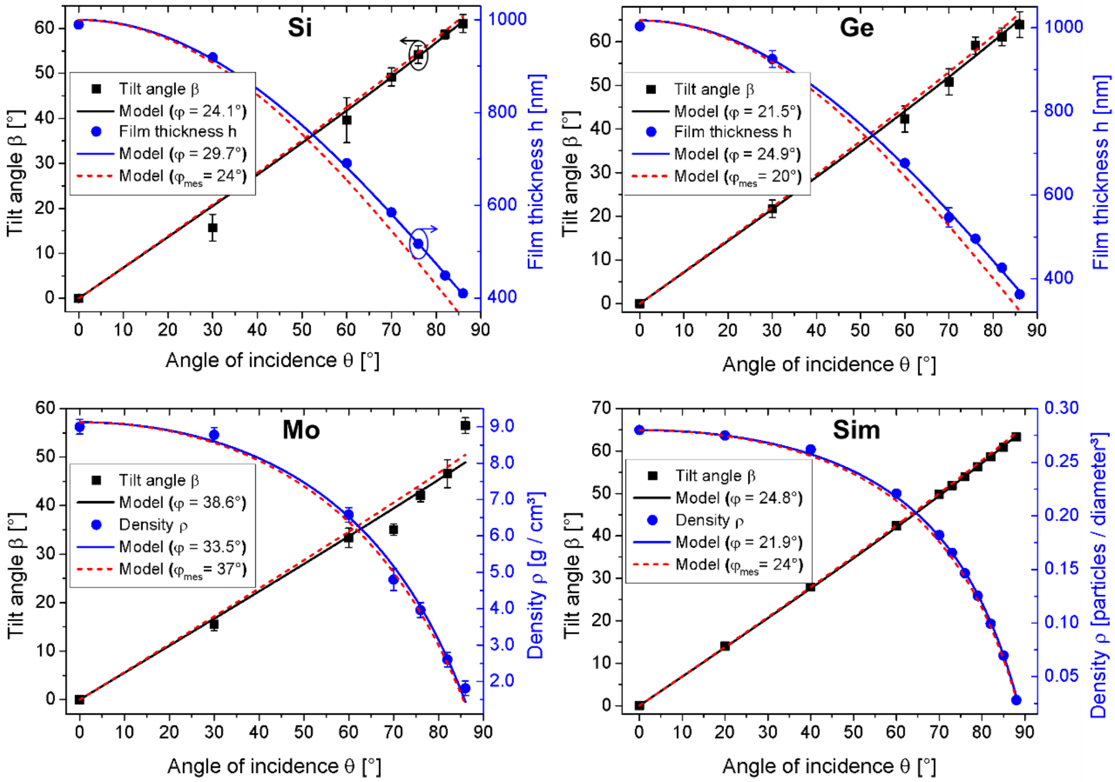

Figure 6.7: Measured and fitted tilt angles for varying angles of incidence for Si, Ge, Mo and an off-lattice simulation. The prediction of a linear behavior can be confirmed in all cases. Further, the fitted fan angles φ are close to the measured fan angles φ_{mes}. Therefore, the model with φ_{mes} as input describes the observed values quite well (red dotted plots). The same applies for the film thicknesses and the densities. The small deviation at very oblique incidence angles is discussed in the text.

had to be used as fitting parameter. Nevertheless, comparing the fitted fan angles for SiO_2 obtained by the tilt angle and the porosity measurements shows a good match. The same applies for the ITO films. Taking the fan angle, obtained from the tilt angle fit, as input for the porosity prediction emphasizes the model applicability (also illustrated in Figure 6.8 **c** and **d**).

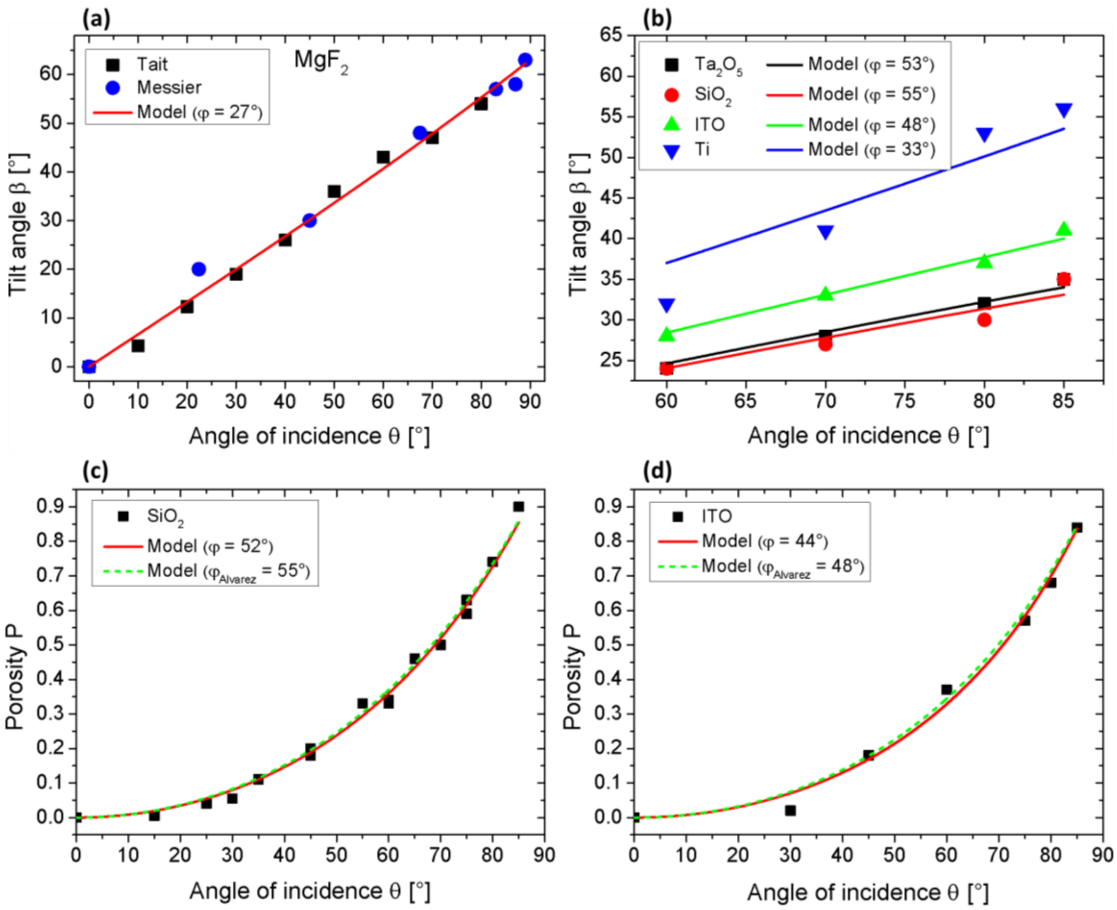

Figure 6.8: (**a**) Column tilt angles for MgF_2 taken from Tait *et al.* [18] and Messier *et al.* [65]. (**b**) Column tilt angles for selected materials from Alvarez *et al.* [111]. The linear behavior of the tilt angles is found for these materials, too. (**c**) and (**d**) show porosity data for SiO_2 and ITO, respectively (obtained by Poxson *et al.* [68]). The curves can be fitted with the model quite well. Furthermore, taking the fan angles obtained from fitting the tilt angles from Alvarez (b), allows a good prediction of the porosities over the complete angle of incidence range.

6.5 Summary

In this chapter a model to describe various morphological parameters of OAD thin films was developed.

- It was shown that the established semi-empirical models allow only a rough estimation of the influence of the incidence angle on the properties of obliquely grown films.
- Based on the observation that Tanto's fan model does not consider the important mechanism of growth competition, a new model was developed. This new model is able to describe the dependency of the tilt angle for the complete incidence angle range and for a variety of materials, and thereby solves a problem that is under discussion since the 1960's. Furthermore, the density and the growth rate are predicted quite well, too.

- The model was checked for various data from literature and own measurements. A good agreement with the experimental observations could be found. The fitted fan angles give a consistent image and can be confirmed by direct measurements.

The results, presented in this chapter, were previously published in [112].

7 Film optimization for applications

7.1 Boron doped Si nanostructures

Nanostructured thin films are a promising candidate for various electrical applications. The high optical absorbance of such films makes them useful as solar absorbers [113-118]. Furthermore, due to phonon confinement and scattering effects, nanostructures exhibit a low thermal conductivity [119-122] and are therefore interesting for thermo-electric energy harvesting applications as well. Finally, electro-mechanic devices, as pressure sensors [123] are under discussion, utilizing the possibility of OAD and GLAD to control the morphology of the grown nanostructures.

A way to control the electrical properties of the material itself is required for these applications. Doping of crystalline silicon is a well-known standard in nowadays technology. As shown in section 4.1, silicon nanostructures are crystalline if grown at substrate temperatures above ~ 500 °C. While tilted nanostructures just exhibit an enlarged diameter at this growth temperature, realization of other structures shapes (upright, spirals) may be impeded due to the intensified surface diffusion [124, 125]. Deposition at lower temperatures allows more control over the structure shape, but leads to the formation of amorphous material.

Usually, amorphous silicon (a-Si) is grown with chemical techniques (e.g. CVD [126-129]) from the precursor silane (SiH_4), and often used for solar cells. CVD-grown a-Si can be doped by addition of boranes (as B_2H_6) or stibanes (as SbH_5) during the synthetization process. In contrast, PVD-grown a-Si cannot be directly doped with boron or antimony. This is caused by unsaturated silicon bonds (called ‘dangling bonds’), existing in the amorphous material [130-132]. These dangling bonds force the dopants into inactive atomic configurations, and therewith inhibit the creation of shallow defect states in the band gap [133]. A method to overcome this is to passivate the dangling bonds by hydrogen [129, 132, 134, 135]. If prepared by PVD, hydrogenated amorphous silicon (a-Si:H) is deposited commonly by sputtering techniques, where the molecular hydrogen is dissociated in a plasma source and brought to its reactive atomic state. As the best structural control for GLAD growth is obtained when the energy input stays low (minimizing surface diffusion), molecular hydrogen is dissociated thermally in a hot tungsten capillary for the here shown results. Since this technique is, to the best of the author’s knowledge, not used in literature for doping purposes, it has to be investigated deeper. The aim is to find a parameter window, in which the material remains amorphous, but exhibits a controllable conductivity.

In order to measure the conductivity of the deposited material, silicon was deposited at normal incidence onto fused silica slides with dimensions 10 mm x 20 mm. On top of the obtained films, three metal stripes were deposited using a polyimide shadowing mask.

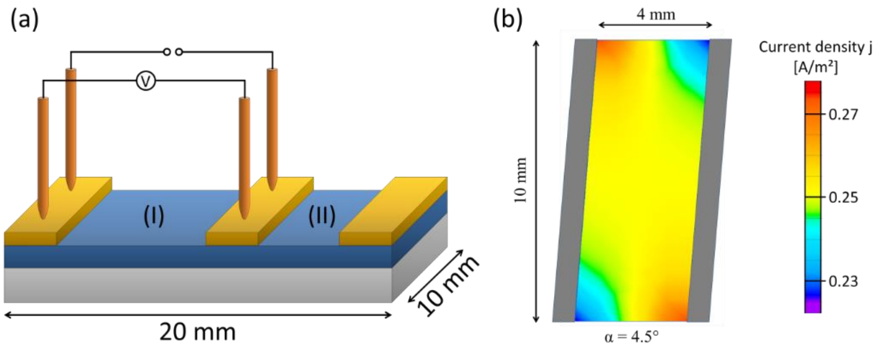

Figure 7.1: (**a**) Schematic illustration of the measurement geometry. The fused silica substrate (grey) is coated with the doped a-Si film (blue), on which metal contacts (yellow) are evaporated by shadowing lithography. The 4-point geometry eliminates the wire and tip resistances, while the two differently spaced test areas (l = 8 mm and 4 mm) allow to estimate the contact resistance. (**b**) Current density distribution, obtained by a FEM simulation of test area (II) and a 4.5° twisted contact. Less than 0.5 % difference to the non-twisted case can be measured.

The spacing between the stripes was 4 mm and 8 mm. Measurements were conducted by pressing a pair of two gold needles on each adjacent stripes and performing a 4-point measurement. A schematic illustration of the measurement geometry can be found in Figure 7.1 **a**.

The use of a 4-point technique eliminates the resistive influence of wires and the contact from the gold tips to the evaporated metal electrodes. The contact resistance between the semiconductor and the metal electrode can be estimated by comparing the measurement results from the areas marked with (I) and (II) in Figure 7.1 **a**. For none of the investigated films, a serious influence of the contact resistance could be found, as the resistances from (I) were always nearly exactly twice as large as from area (II) and the I-U-curves were linear. This may be attributed to the high defect density in the amorphous material (despite the hydrogen passivation) that suppresses the formation of wide depletion zones in the a-Si [136-139], therefore allowing tunneling currents to appear. In addition, the Poole-Frenkel effect may play a role, as the strong field close to the contacts may drastically increase the conductivity of the a-Si. Al and Ti contacts were tested, both working well without any notable difference.

As the shadowing masks were applied manually onto the glass slides, a slight twist of the mask against the film cannot be ruled out. To test if this could be a problem a finite-element simulation (FEM), using the software package QuickField [140], was conducted. For an assumed film thickness of 1 µm with a resistivity ρ of 10^5 Ωcm, a voltage of 1V was applied on test field (II). This would lead to a current flow of 2.5 nA. The simulation gives the same result. To test the influence of a twist, the geometry was tilted by 4.5° (see Figure 7.1 **b**). While the current density shows some differences, the total current flowing through the semiconductor film was simulated to be 2.5133 nA. Thus, the error is less than 0.5 %. As larger tilts are easily visible, the influence of mask tilting can be ruled out.

All tested films had a thickness of 1 µm and were deposited with the maximum achievable hydrogen flux of 0.4 sccm and a gas cracker temperature of 1800 °C. In a first experimental series, thin films with a boron concentration of 3×10^{20} cm^{-3} were prepared at different deposition temperatures T_S, to find the parameters of best defect passivation. It is expected that with less active defects, the doping should become more efficient, thereby lowering the film resistivity. Indeed, a drop of the resistivity with increasing temperature to a minimum of 780 Ωcm at a deposition temperature of 300 °C could be found, while the resistivity rises again above a temperature of 350 °C, as shown in Figure 7.2 **a**.

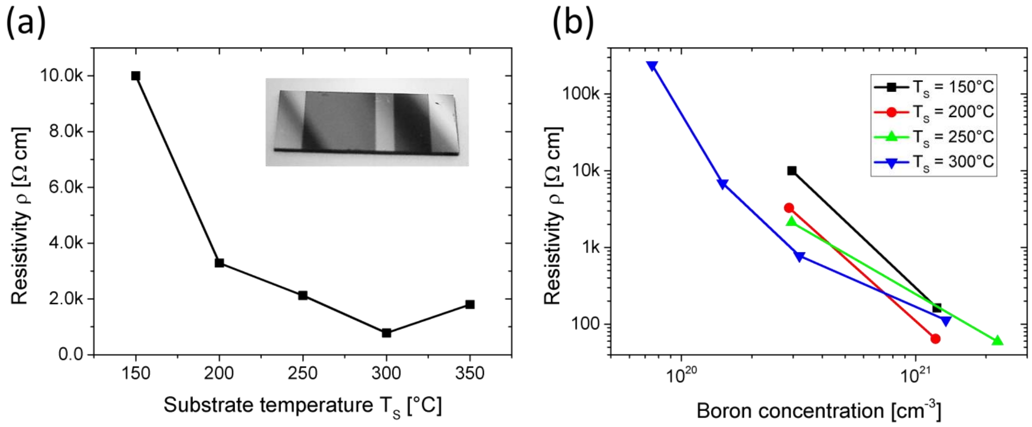

Figure 7.2: (**a**) Influence of the substrate temperature on the resistivity for a fixed boron concentration. The inset shows a photo of a sample. (**b**) Influence of the boron concentration on the resistivity for various substrate temperatures.

An explanation of this minimum can be found in the strength of the B-H and Si-H bonds, which are stated to dissociate at around 300 °C and 500 °C, respectively [135, 141, 142]. This means that at low temperatures, the boron itself is passivated by hydrogen and hence not electrically active (e.g. [143-146]). At temperatures higher than 300 °C, the Si-H bonds start to break, leading to a less effective defect passivation and therewith an increased resistivity. Varying the boron concentration in the films influences the resistivity. For films deposited at 300 °C, the resistivity can be reduced down to around 100 Ωcm, if the boron concentration is increased to 1.5×10^{21} cm^{-3}, as illustrated in Figure 7.2 **b**. Notice that the equilibrium solubility limit of boron in silicon lies around 2×10^{20} cm^{-3} [147-149]. While no boron inclusions were seen by SEM, and all selected films were tested to be semiconducting (e.g. by measuring the resistivity vs. the temperature), at higher concentrations this may become important.

These experiments prove that it is possible to vary the electrical properties of silicon in a temperature range, in which a good structure control by GLAD is still possible. Electrical measurements directly on OAD and GLAD nanostructures are challenging, due to the difficulty to create a reliable top contact. This top contact is needed, because an in-plane measurement obviously cannot be used to investigate films consisting upstanding nanostructures. Different problems can occur during contact deposition:

I. If the bottom surface is non-flat (e.g. at the rim of a bottom electrode), the nanostructures could have a strongly reduced thickness at this point, so that the deposition of a metal onto this region may give a short-circuit to the bottom electrode (see Figure 7.3 **a**).

II. Another source of error may arise due to the presence of dust particles (or particle ejected from the evaporation source) that produce large shadows during OAD and therefore leave the bottom contact uncoated. Therefore, subsequent top-contact deposition would produce a large-area electrical bypass (Figure 7.3 **b**).

III. Finally, bundling effects can locally reduce the distance between top and bottom contact (Figure 7.3 **c**).

In all of these cases, an electrical measurement would rather measure the morphological defect density instead of nanostructure properties, as the test current would follow the electrical favorable defects.

To overcome this, a plane back-contact, a very clean substrate surface as well as precisely controlled deposition parameters are necessary. Another approach could be found in testing individual structures, either after removing the structures from the substrate (as demonstrated, e.g., by Hochbaum *et al.* [122] or Boukai *et al.* [150]), or by *in situ* testing with a conductive AFM tip (as by Wang *et al.* [151] or Tan *et al.* [152]). Nevertheless, realization of these approaches would be quite time-consuming, but the fact that the material can be doped at typical GLAD and OAD conditions gives strong indication that this is possible with the nanostructures as well. Finally, it should be noticed that at oblique tilt angles, the relative incidence angle of the effusion cells changes, which could lead to strong variances in the passivation and doping efficiencies.

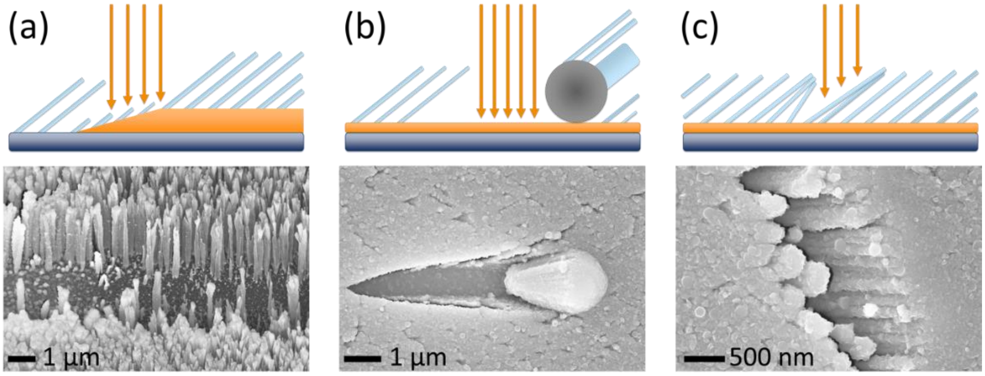

Figure 7.3: Schematics and SEM images of different contact error mechanisms. (**a**) Reduced deposition at the edge of a structured bottom electrode. (**b**) Shadowing at a dust particle. (**c**) Bundling effect. In all of these cases, the bottom electrode is not covered completely, so that deposition of the top-electrode leads to a short-circuit.

7.2 Surface functionalization for biosensors

Plasmon based thin film biosensors have been developed in various configurations for sensing a variety of target samples, like pesticides, pollutants, viruses, and diseased tissue [153, 154]. Utilizing effects, such as surface enhanced Raman scattering (SERS), surface enhanced fluorescence (SEF) and surface enhanced infrared absorption (SEIRA) enables the detection of tiniest amounts of these agents. Sculptured thin films are preferable as well for biochip applications in which a 2D array of small pixels (< 0.1 mm²) on a substrate is used to sense a large number of analytes in parallel (lab-on-a-chip systems).

Compared to normal Raman scattering, the signal of Raman active molecules is increased by many orders of magnitude, if these molecules are brought close (< few nm) to metal surfaces [155, 156]. This effect is typically assigned to the strong electric field enhancement in the vicinity of light induced surface plasmons and can be quantified by Surface Enhanced Raman Spectroscopy [157, 158]. While the exact mechanisms and the maximum enhancement are still under discussion, this effect is widely used to detect and measure a variety of different specimen, like DNA [159], bisphenol-A-polycarbonate [160], hemoglobin [161], viruses [162] and so on (for an overview see, for example, [153]). The magnitude of the enhancement is influenced by a couple of properties of the metal surface. One important parameter is the surface area. The larger it is, the more molecules can adsorb and consequently more molecules contribute to the signal. However, if the film thickness becomes too large, the excitation light does not reach deeper adsorbed molecules, which are therefore not active anymore. Another important parameter is the spacing of adjacent nanostructures [163]. The smaller the distance between the nanostructures becomes, the higher is the field intensity between them, down until a certain distance when hybridization effects start [164]. Shape and curvature of the nanostructures also play an important role, as higher curvatures lead to higher field strengths [163]. Finally, the material of the nanostructures surface has an influence – not only for Raman signal enhancement, but also for the chemical stability and the behavior of the material during film growth [165].

A widely used material for SERS based sensors in general [166-170] and for GLAD particularly [171-173] is silver. It can be passivated with a thin layer to become stable against oxidation and provides high enhancement factors [174]. Furthermore, it is not as expensive as gold. As a drawback, silver shows very strong surface self-diffusion, impeding the exact shape control during GLAD growth [175].

A film thickness of around 350 nm has shown to be a good compromise between signal intensity and sensor deposition time [46]. Thicker samples do not improve signal enhancement significantly. Figure 7.4 **a** shows such an Ag film deposited by ion beam sputter GLAD.

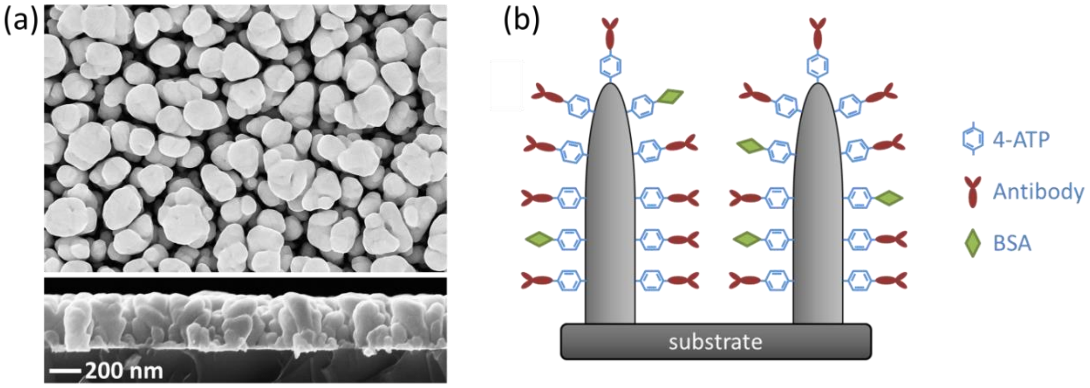

Figure 7.4: (**a**) Top and cross-section view of Ag GLAD structures, with 350 nm thickness and 50% porosity. (**b**) Principle of the used sensor devices. The Ag nanostructures are covered with 4-aminothiophenol (4-ATP) first. Antibodies provide the selectivity and bovine serum albumin (BSA) blocks the non-specific sites.

Most Raman spectra of organic compounds are rather complex, with oscillation modes spreading over a large energy shift range and with various optimal excitation wavelengths. In contrast, some materials are not Raman active at all, and therefore cannot be measured directly. Moreover, molecules in solutions do not necessarily bind to or even remain for long enough times near the surface. To overcome this, the base metal surface is usually functionalized to provide the sensor with specificity, enhance the sensitivity and to simplify measurements (see e.g. [176] and Figure 7.4 **b**). For these demands, two different functionalization steps are performed. In the first step, a Raman active agent is allowed to react with the nanostructure surface. For silver, 4-aminothiophenol (4-ATP) is a good choice for two reasons. On the one hand it binds to the metal due to the formation of a thiol binding, on the other hand the $-NH_2$ group on its opposite terminal provides the ability to bind to enzymes, antibodies or bacteriophages. Additionally, 4-ATP is Raman active and can be used for measurement. Recently it was shown that in some cases the metal surface can directly provide the necessary Raman or fluorescence activity (e.g. carboxidized silver at the silver surface [177]). This auto-fluorescence can be used instead of the activity of the 4-ATP. Regardless which active compound is finally used, the excitation can then be done with a known, fixed wavelength and measurement can be taken at a known spectral shift range. The second functionalization step makes the sensor selective to the targeted molecules. This can be done utilizing antibodies that only bind to the molecules of interest [178, 179]. These antibodies are attached to the 4-ATP, which typically does not influence the Raman behavior of the surface directly. Additionally, oligopeptides [180], aptamers [181] or bacteriophages [182] can be utilized. To guarantee that unrequested molecules cannot later bind to the surface, the remaining unspecific sites, not reached by the antibodies, are blocked with bovine serum albumin (BSA). BSA has the additional advantage that it acts as non-fouling agent. After this functionalization, the sensor is ready for use and can be stored until needed.

The process of measurement runs as follows: Firstly, the Raman or fluorescence spectrum of the virgin sensor is measured. Then, the target solution is applied. If there are molecules inside, which can bind to the antibodies on the surface, they will do so. This reduces the intensity of the originally seen Raman scattering / fluorescence bands due to three possible reasons. The first one is that the now bound molecules absorb a part of the incident and of the scattered light as well. Secondly, these molecules bind spatially close to the Raman active sites, and therefore may cause a slight shift of the energies of their vibration modes, and consequently of the position of the Raman bands. Finally, the additional molecules may weaken the electric fields, especially between the nanostructures, and thus the enhancement of the scattering signals, too. Altogether, a reduction of the measured intensities indicates the existence of the targeted molecules. The higher the concentration of these molecules in the solution is, the more the signal is reduced. The concentration of the target molecules in the test solution can be determined, if the sensor is calibrated with solutions of known concentrations. This approach does not only enable the detection of molecules, it also allows one to detect entire bacteria, if the appropriate antibodies are used. Notice, that larger molecules or bacteria will not penetrate deeply into the porous thin film.

As an alternative to antibodies, bacteriophages can be utilized to provide the sensor with specificity. Antibodies bind exclusively to single molecules or molecule groups, which is a drawback if it is not known which molecules reside inside the solution (e.g. which molecules are expressed by pathogenic bacteria). By applying bacteriophages, access to more complex interactions is provided. A bacteriophage, for example, can be used to distinguish between living and dead bacteria, which cannot be done with antibodies, because they would also bind to the hulls of dead bacteria. Generally, indirect detection of potentially harmful or poisonous substances is often more efficient than their direct measurement. Therefore, the measurement of biomarkers represents an important field of applications.

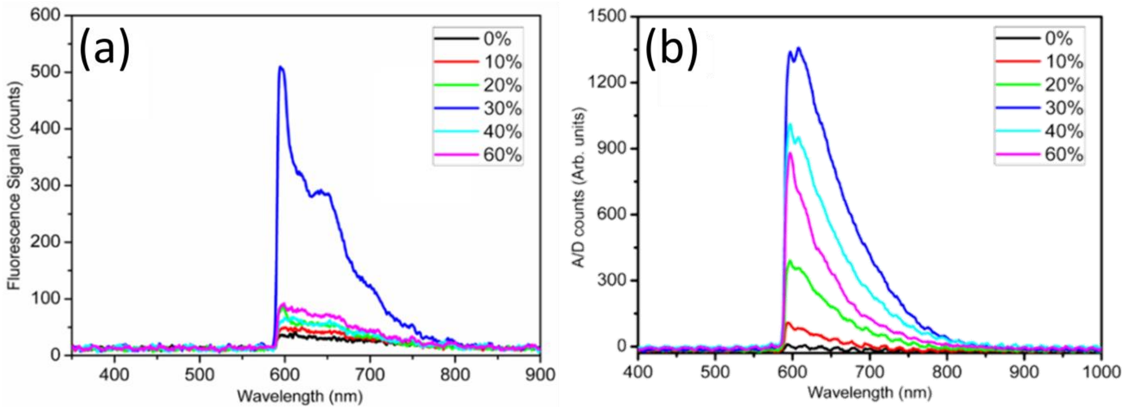

Figure 7.5: Dependency of the SEF signal strength from the porosity of the GLAD films for the (**a**) auto-fluorescence of the carboxidized surface and (**b**) spin-coated rhodamine-123.

To find the optimum porosity of the Ag films for bio-sensor use, at first, SEF of the carboxidized silver surface as well as of rhodamine-123 was measured. For this purpose, structures were deposited with ion beam sputtering at different incidence angles, as presented in Figure 7.5. An optimum at around 30% porosity was found, which could be explained by the interplay of surface area and distance between adjacent structures. Therefore, all other studies were conducted with Ag films of 350 nm thickness and with a porosity of 30%.

7.2.1 Example: Quantification of glycated hemoglobin

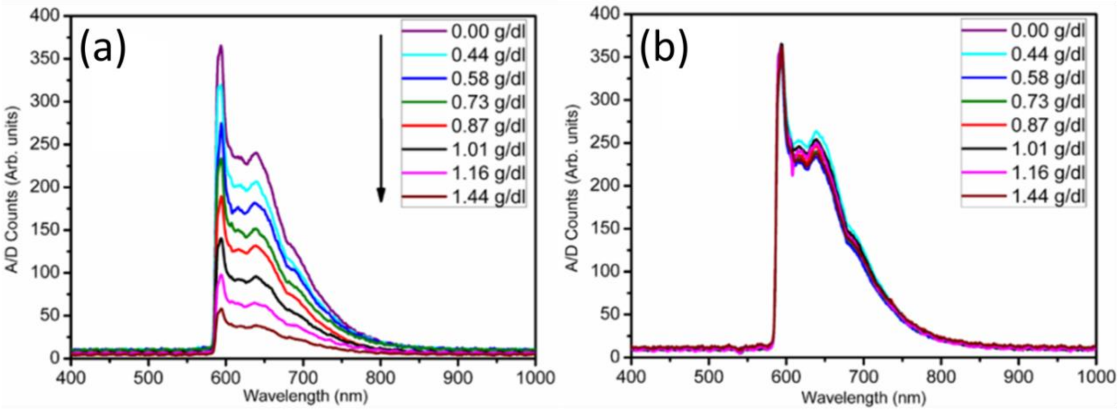

Figure 7.6: SEF signal intensity of different (**a**) glycated (HbA1c) and (**b**) normal hemoglobin (Hb) concentrations.

As a first example, the specific quantification of glycated hemoglobin (HbA1c) from normal hemoglobin (Hb) (for details see [177]) is presented. HbA1c is produced in the human body by an Amadori rearrangement of normal Hb, with a rate that is proportional to the actual blood glucose level. So, the total fraction of glycated hemoglobin is a measure of the average blood glucose concentration for the last eight to twelve weeks – the average lifetime of erythrocytes. This is a clinically more relevant value than the actual blood glucose concentration, which varies strongly over the day and also with recent supply of carbohydrates [183]. Usually, the concentration of HbA1c is measured by immunoassay or chromatography techniques, which are slow, inaccurate and require expensive equipment [184]. Using a GLAD based SEF sensor, an accurate determination of this value within minutes becomes possible. Even though this sensor utilizes the mentioned auto-fluorescence, a monolayer of 4-ATP is deposited firstly onto the silver, to act as linker for the next process steps. Following this, an EDC-NHS modified anti-HbA1c antibody is immobilized on the 4-ATP layer. This provides the sensor with its selectivity, since this antibody does not bind to normal Hb. Finally, the sensor is incubated in a BSA solution to block the non-specific sites on the metal surface. Then the sensor can be stored at 4°C until use. The measurement is carried out as follows: At first, the intensity of the auto-fluorescence is measured. Then the solution of interest (in a clinic environment: blood) is applied to the sensor surface and allowed to interact with it for a fixed time (~ 2 minutes). During this time, HbA1c molecules can bind to a part of the antibodies, proportional to the actual HbA1c concentration. After the time span, the sensor is washed to stop the reaction. Finally, the fluorescence spectrum is measured again. The decrease of the intensity of selected fluorescence bands is now proportional to the concentration of HbA1c in the solution, while non-glycated Hb does not interact with the surface and by this does not change the measurement, as shown in Figure 7.6. Notice that the sensor can be used for a few times, if it is regenerated by a glycine buffer and subsequently properly washed.

7.2.2 Example: Detection of biomarkers

As a second example, the detection of a biomarker is demonstrated (for details see [185]). A biomarker for the existence of endocrine disrupting compounds is chosen. While in the first example the quantification is of primary interest, here the detection of tiniest amounts is the important feature. Endocrine disruptors are agents that interfere with the hormone system of higher lifeforms, and by this disturb the natural regulation of body functions. Since these compounds can accumulate in organisms over time, even the existence of traces of these substances in the environment is hazardous. Direct detection of them is difficult, not only due to their small concentration, but also because their spatial and time distribution is typically unknown. Thus, the negative test of a sample taken at a specific place and time does not necessarily mean that organisms living there are not exposed to the searched substances. In this case, a better choice is to utilize the accumulation of the endocrine disruptors in organisms and to check directly if they are affected. A common choice for this is the protein vitellogenin (Vg) [186, 187], which is an egg yolk precursor and synthesized exclusively by the female individuals of vertebrates, but not by their male counterparts. If Vg is found in male individuals, it is direct evidence that they are affected by an estrogenic endocrine disrupting compound. The sensor is prepared in a similar way as in the first example, but now with an anti-Vg antibody [188]. The reduction of the intensity of the Raman signal of 4-ATP at a shift of 1077 cm^{-1} is taken as a measure of the Vg concentration in the test solution. Even a concentration as low as 5 pg/ml leads to a change of the signal intensity of approx. 10%, which can be detected easily (see Figure 7.7 **a**). To prove the selectivity of the sensor, different concentrations of another protein (fetuin) were applied to it. No change in the Raman signal intensity could be found in this case. Sensors prepared as described can be stored for at least three months, without loss of response efficiency.

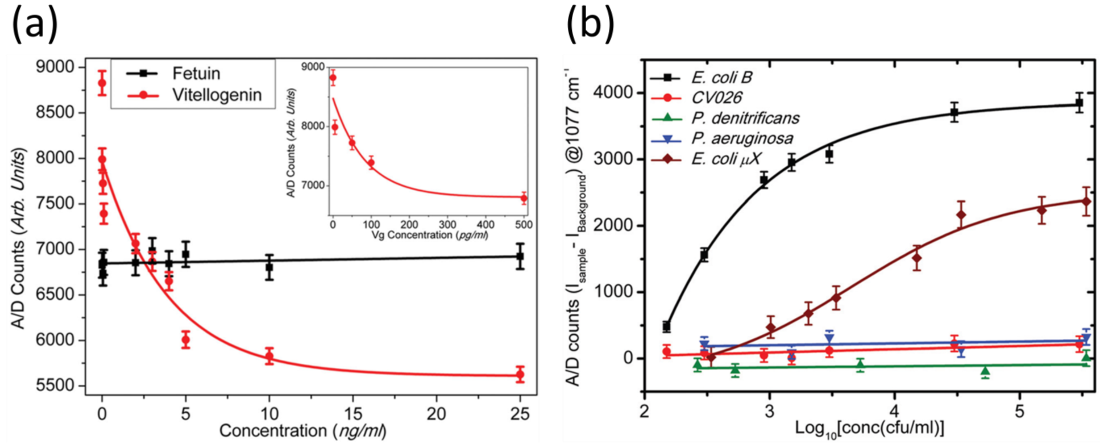

Figure 7.7: (**a**) Comparison of the change of the SERS signal intensity of the 1077 cm^{-1} peak for different concentrations of vitellogenin and fetuin. (**b**) Comparison of the same peak intensities of the E. coli sensor for varying concentrations of different bacteria strains.

7.2.3 Example: Selective measurement of bacteria concentrations

A final example is the use of a bacteriophage functionalized sensor for the detection of bacteria concentrations down to one bacterium per 10 µl (details in [189]). Bacteria can also be detected with antibody functionalized sensors [190, 191], but the use of bacteriophages enables to distinguish between living and dead bacteria [192]. Since bacteriophages are typically larger than antibodies, and bacteria are much larger than the previously targeted agents, the enhancement and sensing mechanisms are slightly different in this case. The bacteriophages can just enter the porous thin Ag film partially, whereas the bacteria can only interact with the top tips of the nanostructures. However, sensor preparation remains the same in principle. After the formation of the 4-ATP layer a glutaraldehyde cross-linking layer is added, serving as substrate for the bacteriophages. BSA is applied to block unspecific sites. If living bacteria come close to the bacteriophages, DNA will be injected into them, forcing the bacteria to produce more phages. During this process the intensity of the observed Raman signals is increased. This process permits the selective detection of, for example, E. coli bacteria down to a concentration of 150 cfu ml^{-1} (cfu - colony forming units). Since just approximately 10 µl of the test medium are necessary for the measurement, this corresponds to a single bacterium in the test volume. Again, specificity was tested. Different bacteria strains (chromobacterium violaceum, paracoccus denitrificans, pseudomonas aeruginosa) were applied to the sensor, whereas no change in the Raman signal intensity was found, as depicted in Figure 7.7 **b**. Therefore, this type of sensor allows the detection of the existence of a single bacterium in a mixture with different strains, as it would be usually found in clinical or environmental cultures.

The optical measurements as well as the surface functionalization, presented in this section, were performed in cooperation with an Israeli partner group and led to a variety of journal publications [177, 185, 189] and an invited encyclopedia article [193].

7.3 Core-shell structures by pulsed electrodeposition

As seen in the previous section, the surface of the nanostructures determines their properties to a great extend. Providing nanostructures with specially tailored surface coatings may open new fields of applications. Such coatings could protect the core material, change the chemical behavior, or serve for the production of controllable nanostructure shapes of materials, which are difficult to grow by GLAD directly.

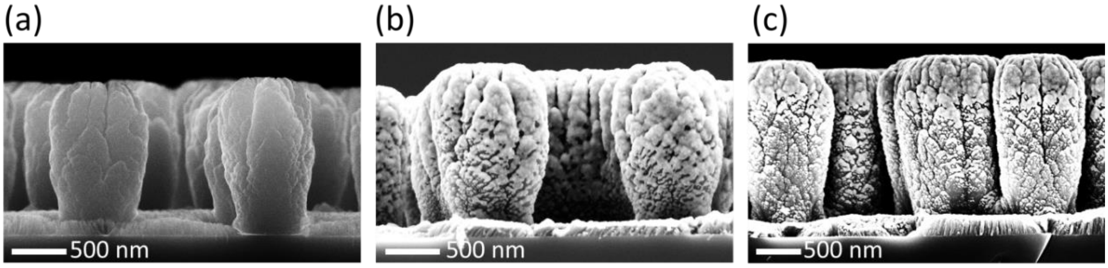

Figure 7.8: SEM side-view images. (**a**) Periodically arranged Si structures. Onto these structures, silver is deposited by (**b**) sputtering and (**c**) evaporation at room temperature. A closed shell could not be obtained.

Due to the fractal nature of the GLAD and OAD films, physical deposition of such coatings is impossible. As shown in Figure 7.8, deeper located regions of previously deposited GLAD nanostructures cannot be reached by further incoming material, leading to an incomplete coverage of the core structures. Due to the upright morphology of the nanostructures, material that is deposited subsequently can hit the wall of these columns just with a locally highly oblique incidence angle, leading to the formation of a porous, incomplete coating.

With the aim to coat complex shaped nanostructures with different materials, various techniques such as electroless chemical deposition [194], atomic layer deposition (ALD) [195] or electroplating [196], have been developed. Electroless deposition is a purely chemical process, driven by the kinetics of the involved reactions. The thereby obtained diffusion limited growth is typically not capable of producing conformal coatings on complex shaped substrates. ALD was developed specially for this purpose, but is a rather complex process and not suitable for all material combination (core / shell). Electroplating has some similar features as ALD, as the need for an external driving force (electrical current) provides a possibility to control the electro-chemical reaction. The main advantage of this technique, compared to electroless deposition (or conventional CVD), is that the deposition reaction can be interrupted by stopping the external current. This allows an exact control of the amount of deposited materials (that is proportional to the total transferred charge) and opens the possibility to pause the deposition for a defined period of time. Periodic interruption of the deposition process is known as pulsed electrodeposition [197], which is suited especially for coating of high aspect-ratio holes or porous thin films [198].

To study the electrodeposition approach, firstly Ni and NiFe nanostructures were grown by GLAD ($\theta = 86°$, 5 rpm) on NSL pre-structured substrates as well as on flat substrates. All substrates were provided with a roughly 100 nm thick Ni or NiFe film before GLAD, to ensure electrical conductivity over the complete surface. Afterwards, the GLAD coated samples were cleaved into pieces of approximately 0.5 cm^2 size. For the electrodeposition, a commercially available gold electrolyte containing chloroauric acid and potassium ferrocyanide was used. The concentration of pure gold was 3 g/l. The galvanic cell consisted of a 10 ml glass beaker, a steel anode and a conductive clamp for the samples. An electric circuit created the current pulses, as illustrated in Figure 7.9. A microcontroller controlled pulse number and timing. While the microcontroller was embedded in an Arduino Uno board, direct port register programming had to be used, as the standard Arduino commands do not allow a fast and precise switching. Rise and fall times of less than 200 ns and a time resolution of 125 ns were achieved with this assembly. The actual surface area of nanostructured thin films is not accessible experimentally and therefore remains unquantified. However, the macroscopic area of the substrate on which the nanostructures are grown is known. Hence, the given current densities refer to the substrates area. Notice that the substrate area is smaller than the area of the nanostructured thin films, resulting in an overestimation of the real current densities. After the Au deposition, the samples were removed from the galvanic bath and rinsed with water.

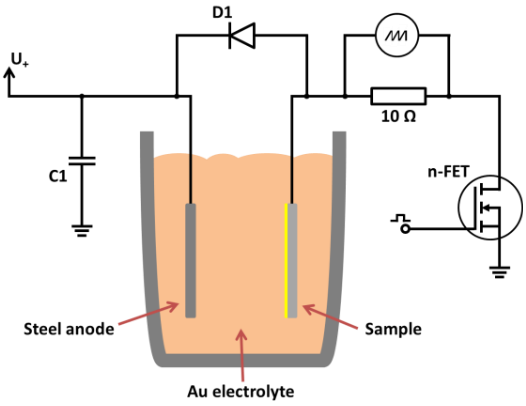

Figure 7.9: Schematic illustration of the pulsed electrodeposition setup. The capacitor C1 is realized as parallel connection of a 4.7 mF electrolyte and a 100 nF ceramic capacitor. Diode D1 is of Schottky type. The pulse shape and current are controlled by an oscilloscope over a 10 Ω resistor.

In all experimental approaches applying non-pulsed DC currents, the films peeled off rapidly from the substrate, and gold condensation was observed only on top of the nanostructures. In these cases, the continuous reaction leads to a diffusion driven coating, where exposed parts of the sample show a faster coating process than deeper located parts, leading to a non-equal final film thickness. Thus, the reaction must be stopped before the concentration of the gold ions in the solution between the nanostructures drops too low. During the reaction break, new ions diffuse into the depleted regions, so that in the next reaction interval a uniform deposition can be realized again. As a rough estimation, a cylindrical hole with a depth of 1000 nm and a diameter of 100 nm is depleted completely in around 100 µs, if typical values for the current density of 100 mA/cm^2 and an initial concentration of 3 g/l of Au(III) ions are assumed. This would correspond to a gold thickness of about 0.004 nm per current pulse on the walls of the hole. To assure a homogenous coating, the on-time t_{on} of a pulsed deposition has to be much smaller than this, while the off-time t_{off} has to be sufficiently long to allow new ions to diffuse into the hole. Figure 7.10 illustrates the deposition and diffusion of the Au ions in-between the nanostructures for DC and pulsed electroplating.

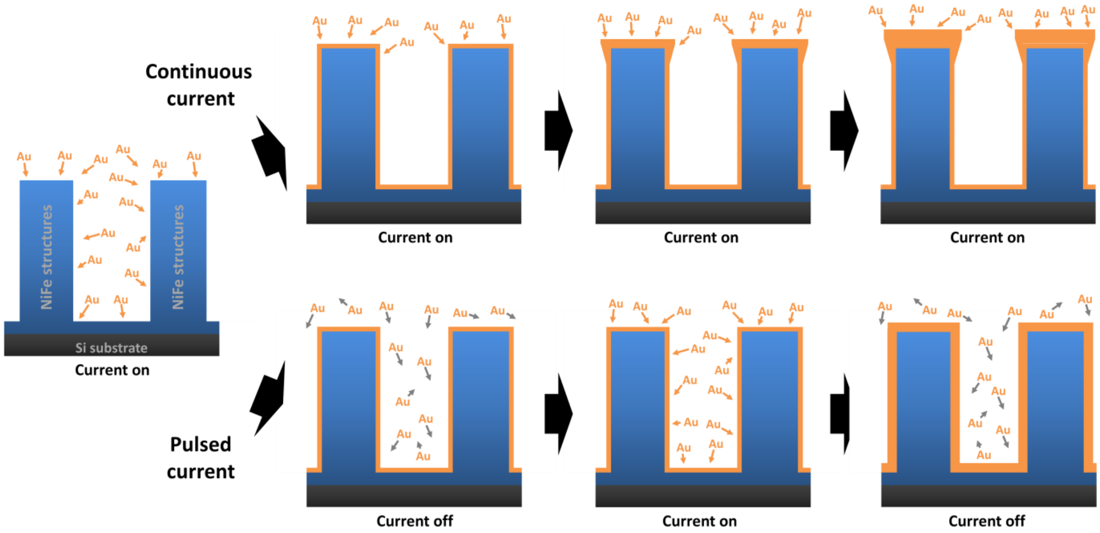

Figure 7.10: Schematic representation of DC and pulsed electroplating. In the continuous current (DC) case, the space between the structures rapidly de-saturates. Consequently, further deposition can only take place at the tips of the nanostructures. During pulsed deposition, gold ions have the chance to diffuse into the space between the structures during the off-times, enabling a more conformal coating.

For all following deposition experiments, an on-time t_{on} = 1 µs and an off-time t_{off} = 9 µs was chosen. Figure 7.11 **a** shows a NiFe nanostructure grown on a NSL substrate. Interseed growth is not obtained and the structures are well separated. Figure 7.11 **b**, **c,** and **d** demonstrate the development of the gold coating on NiFe nanostructures with increasing pulse number. The current density during the pulses was 89, 88 and 97 mA/cm^2, respectively. At the beginning of the coating process, small isolated gold crystals can be obtained on the nanostructure surface and the substrate layer that interconnect with increasing deposition time. Finally, a rough closed layer was observed after a charge transfer of approximately 1.45 C/cm², and a total deposition time of 150 s. In Figure 7.12 **a**, NiFe nanostructures grown on planar substrates are presented. These well-separated structures have diameters between 30 nm and 150 nm. Some of the nanocolumns broaden with increasing height, which is typical for non-patterned growth [24]. From Figure 7.12 **b**, **c** and **d** can be observed that the development of the gold coating undergoes the same evolution as on the pre-patterned samples. The current densities were 115, 97 and 98 mA/cm², respectively. The closing of the layer is obtained after a charge transfer of approximately 2.9 C/cm², which is approximately twice as much as in the patterned case. This is caused by the fact that the surface area for un-patterned GLAD growth is higher than for growth on pre-patterned substrates. After a total charge transfer of around 3.7 C/cm², the growing gold crystals start to bridge neighboring nanostructures and form a very rough layer on top of the underlying film.

In comparative experiments, Au was electrodeposited onto a flat, closed NiFe layer. A growth speed of 95 (nm cm²)/C was obtained. A charge transfer of 2.9 C/cm² would therefore lead to a film thickness of approximately 275 nm on a flat substrate. That this amount of charge is just enough to form a closed layer on the nanostructures emphasizes the enormous surface area of the sculptured thin GLAD films.

The experiments are repeated for pure Ni nanostructures on non-patterned substrates. Differences on the morphology of the nanostructures or the Au coatings, compared to the NiFe structures, are not found. In all cases, the gold layers are closed before the films lose their open pore structure during electrodeposition. Notice that the used combination of the electrolyte and the substrate material leads to the formation of cubic crystals at the beginning of the electrodeposition process, as can be seen in Figure 7.11 **b** and Figure 7.12 **b**. The crystals could not be removed by rinsing the samples with DI water, and an

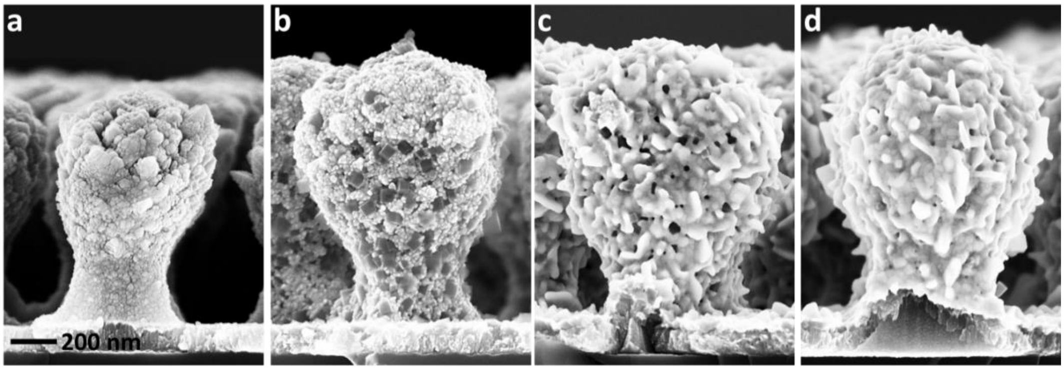

Figure 7.11: SEM images of periodically arranged NiFe nanostructures that were coated by electrodeposition. All samples were deposited with $t_{on}/t_{off} = 1$ µs / 9 µs and a pulse current density of about (92 ± 5) mA/cm². (**a**) uncoated NiFe structures. (**b**), (**c**) and (**d**) Au coated structures after $5 \cdot 10^6$, $1 \cdot 10^7$ and $1.5 \cdot 10^7$ pulses, respectively. In (**b**), the formation of gold crystallites can be observed, while in (**d**) a nearly closed gold layer is achieved.

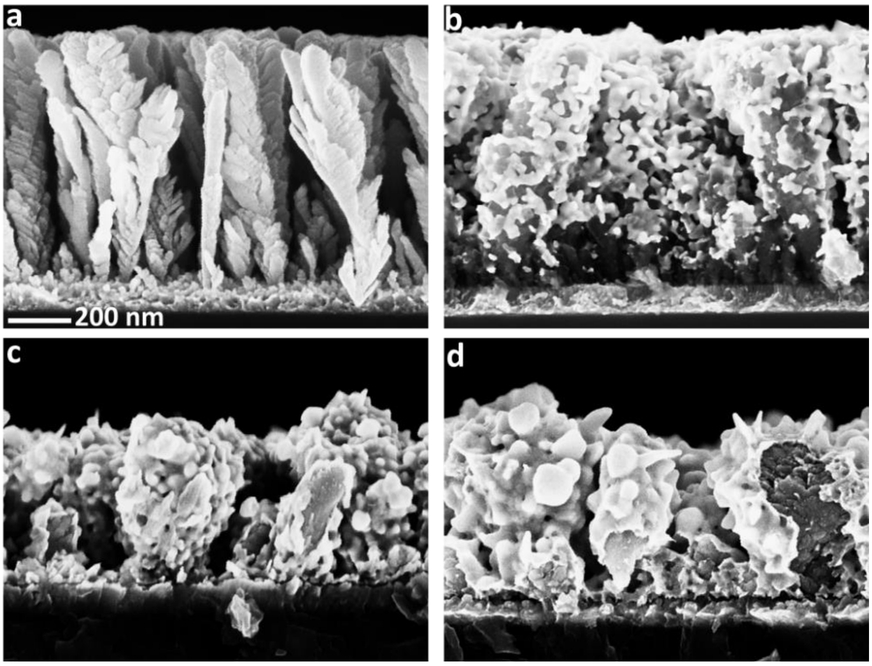

Figure 7.12: SEM images of randomly arranged NiFe nanostructures on non-pattered substrates and coated by electrodeposition of Au. All samples are deposited with $t_{on}/t_{off} = 1$ µs / 9 µs and a pulse current density of about (105 ± 15) mA/cm². (**a**) uncoated NiFe structures. (**b**), (**c**) and (**d**) Au coated structures after $1.5 \cdot 10^7$, $2 \cdot 10^7$ and $3 \cdot 10^7$ pulses, respectively. In (**b**) the initial forming gold crystallites start to coalesce. In (**d**) the nanostructures are completely coated. On the right side of this image, the gold coating was cut open after cleaving the sample for SEM imaging, thus revealing the (darker) NiFe core.

analysis of these contaminations by nano-beam EDX in the TEM revealed large concentrations of potassium inside the cubic crystals. Those crystals become overgrown completely with gold, as the electrodeposition progresses.

The results, presented in this section, were previously published in [199].

7.4 Summary

In this chapter, tailoring of the GLAD and OAD nanostructures beyond the pure shaping was presented.

- It was shown that silicon, even if amorphous, can be controllable doped at process conditions, which allow GLAD growth. Furthermore, different contact failure-mechanisms are presented. Doped Si structures can be applied for energy harvesting and sensor applications.

- Surface functionalization was demonstrated and the optimal film parameters for maximum signal intensity of SERS and SEF measurements were found. Highly selective bio-sensors were prepared based on the produced Ag films that allow detecting biomarkers, bacteria and blood components.
  Related author publications: [177, 185, 189, 193]
- An easy to handle and cost-effective method to coat Ni and NiFe structures with gold layers was demonstrated. A closed gold shell was obtained before the open-pore structure of the GLAD films vanished. Such Au shells could function as protection layer on the NiFe core-nanostructures or serve as substrate for surface enhanced Raman sensors. The demonstrated method can be applied for various core-shell combinations.
  Related author publication: [199]

8 Summary

In the first part of this thesis, it was shown that deposition at oblique incidence angles leads to thin films with a morphology, which strongly deviates from the one obtained at normal incidence. The influence of substrate temperature, beam divergence, and growth competition on the formation of OAD thin films has been investigated qualitatively. Moreover, in an experimental study on Si, Ge and Mo, quantitative results for the thin film porosity as well as the columnar tilt angles are gathered.

In addition to the experimental results, computer simulations are performed. It was demonstrated that an off-lattice simulation provides spatial isotropy but cannot be carried out quickly for realistic deposition cases, e.g. including substrate rotation or beam divergence. Typical off-lattice simulations show a higher performance in simulation speed but introduce a spatial anisotropy, which has influence on simulated thin film parameters such as the tilt angle and the film porosity. By utilizing cluster particles and a geometric simplification ('forbidden volume method'), the anisotropy could be minimized, while a fast simulation algorithm is maintained. The ability of computer simulations to prepare mathematically idealized substrates as well as the ability to track individual nanostructure / columns during growth was used to study the influence of growth competition. Although seeming unlikely at first glance, it could be shown, that rear-standing columns can influence the growth of front-standing ones ('backward-shadowing').

Combining the observations from experiments and simulations, with a study of commonly used models for oblique angle deposition, lead to the development of a new model. In this approach, the shadowing effect as well as the growth competition is considered. The model is based on Tanto's fan model, hence similarly separating the shadowing and the material properties. However, including growth competition leads to quite accurate predictions of the tilt angles, porosities, and growth speeds. Furthermore, the 'backward-shadowing' can be explained by a geometric consideration of the growth zone. The predictions of the developed model fit the experimental observations and simulation results quite well. Further verification is carried out on literature data, where a good match could be found also.

The single parameter of the model, the fan angle, was investigated for a variety of materials and at different deposition temperatures, ranging from -196 °C to 700 °C. This was carried out by either direct measurement of the fan angle on fan structures or by fitting the model onto experimental data of the columnar tilt angles. Both methods delivered results that were in good agreement. Furthermore was observed that materials with lower melting points show a smaller fan angle. A similar behavior is obtained if higher substrate temperatures are used during growth. This leads to the assumption that surface diffusion has a major influence on this parameter, causing smaller fan angles. That is verified by the addition of atomic hydrogen during the growth of silicon nanostructures. In this case, surface hydrides form, that enlarge the activation energy of adatom diffusion, consequently suppressing surface diffusion. Thus, an increase of the fan angle is expected, which is exactly what was observed in the experiment.

The last part of this thesis is addressed to provide a selected film geometry with the necessary surface and material properties for specific applications. This requires considering the self-organized nature of OAD and GLAD growth. To overcome this, the material must either be tuned during deposition or the structures have to be altered afterwards. The first approach is demonstrated by effective doping of silicon in a parameter range that allows to grow OAD and GLAD nanostructures with a considerable control of morphology, namely at quite low temperatures. Because the silicon in the required temperature range is amorphous, and therefore contains dangling bonds, atomic hydrogen had to be added during growth. Secondly, the preparation of core-shell structures was presented. As core served Ni and NiFe GLAD nanostructures, which were provided with a closed Au shell by pulsed electrodeposition. Such a shell could serve either as protection layer for the core, or as functionalization layer for chemical applications. Finally, utilizing a bio-chemical surface functionalization, the ability of GLAD structures was shown to be used in bio-sensors. Therefore, it was taken advantage of the strong surface plasmon resonance of Ag GLAD nanostructures. Utilizing the selectivity of special antibodies, highly sensitive sensing devices could be prepared. This was demonstrated on the specific detection of selected bacteria species and of tiniest traces of bio-markers, as well as on the selective quantification of glycated hemoglobin.

To conclude, this work on the one hand covers theoretical and numerical modeling, giving an answer on the decades-old question about the relation between the angle of incidence and the columnar tilt angle. And, on the other hand, provides routes to functionalize the bare GLAD structures for specific applications.

9 Bibliography

1. Bendavid, A. and P. Martin, *Review of thin film materials deposition by the filtered cathodic vacuum arc process at CSIRO*. Journal of the Australian Ceramics Society, 2014. **50**(1): p. 86.
2. Meschede, D., *Gerthsen physik*. 2015: Springer-Verlag.
3. Knudsen, M., *Die Gesetze der Molekularströmung und der inneren Reibungsströmung der Gase durch Röhren.* Annalen der Physik, 1909. **333**(1): p. 75-130.
4. Greenwood, J., *The correct and incorrect generation of a cosine distribution of scattered particles for Monte-Carlo modelling of vacuum systems.* Vacuum, 2002. **67**(2): p. 217-222.
5. Suetsugu, Y., *Application of the Monte Carlo method to pressure calculation.* Journal of Vacuum Science & Technology A, 1996. **14**(1): p. 245-250.
6. Nishimura, A., H. Kaburaki, H. Ohba, and T. Shibata, *Angular Distribution of Gadolinium Vapor Produced by Electron Beam Heating.* Journal of Nuclear Science and Technology, 1993. **30**(3): p. 270-273.
7. Sigmund, P., *Theory of Sputtering. I. Sputtering Yield of Amorphous and Polycrystalline Targets.* Physical Review, 1969. **184**(2): p. 383-416.
8. Thompson, M., *II. The energy spectrum of ejected atoms during the high energy sputtering of gold.* Philosophical Magazine, 1968. **18**(152): p. 377-414.
9. Feder, R., F. Frost, H. Neumann, C. Bundesmann, and B. Rauschenbach, *Systematic investigations of low energy Ar ion beam sputtering of Si and Ag.* Nuclear Instruments and Methods in Physics Research Section B: Beam Interactions with Materials and Atoms, 2013. **317**: p. 137-142.
10. Feder, R., C. Bundesmann, H. Neumann, and B. Rauschenbach, *Ion beam sputtering of germanium–Energy and angular distribution of sputtered and scattered particles.* Nuclear Instruments and Methods in Physics Research Section B: Beam Interactions with Materials and Atoms, 2014. **334**: p. 88-95.
11. Lautenschläger, T., R. Feder, H. Neumann, C. Rice, M. Schubert, and C. Bundesmann, *Ion beam sputtering of Ti: Influence of process parameters on angular and energy distribution of sputtered and backscattered particles.* Nuclear Instruments and Methods in Physics Research Section B: Beam Interactions with Materials and Atoms, 2016. **385**: p. 30-39.
12. O'Hanlon, J.F., *A user's guide to vacuum technology*. 2005: John Wiley & Sons.
13. Kelton, K. and A.L. Greer, *Nucleation in condensed matter: applications in materials and biology*. Vol. 15. 2010: Elsevier.
14. Pimpinelli, A. and J. Villain, *Physics of crystal growth*. Vol. 19. 1998: Cambridge university press, Cambridge.
15. Barna, P.B. and M. Adamik, *Growth Mechanisms of Polycrystalline Thin Films*, in *Science and Technology of Thin Films*, F.C. Matacotta and G. Ottaviani, Editors. 1995. p. 1-28.
16. Srolovitz, D.J., A. Mazor, and B.G. Bukiet, *Analytical and numerical modeling of columnar evolution in thin films.* Journal of Vacuum Science & Technology A: Vacuum, Surfaces, and Films, 1988. **6**(4): p. 2371-2380.
17. Bales, G.S. and A. Zangwill, *Macroscopic model for columnar growth of amorphous films by sputter deposition.* Journal of Vacuum Science & Technology A: Vacuum, Surfaces, and Films, 1991. **9**(1): p. 145-149.

18. Tait, R.N., T. Smy, and M.J. Brett, *Modelling and characterization of columnar growth in evaporated films.* Thin Solid Films, 1993. **226**(2): p. 196-201.
19. Okamoto, K. and K. Itoh, *Incidence Angle Dependences of Columnar Grain Structure and Texture in Obliquely Deposited Iron Films.* Japanese Journal of Applied Physics, 2005. **44**(3): p. 1382-1388.
20. Enomoto, Y. and M. Taguchi, *Modelling of columnar growth in continuum ballistic deposition.* Applied Surface Science, 2005. **244**(1-4): p. 213-216.
21. Steele, J.J. and M.J. Brett, *Nanostructure engineering in porous columnar thin films: recent advances.* Journal of Materials Science: Materials in Electronics, 2006. **18**(4): p. 367-379.
22. Van der Drift, A., *Evolutionary selection, a principle governing growth orientation in vapour-deposited layers.* Philips Res. Rep, 1967. **22**(3): p. 267-88.
23. Kardar, M., G. Parisi, and Y.-C. Zhang, *Dynamic Scaling of Growing Interfaces.* Physical Review Letters, 1986. **56**(9): p. 889-892.
24. Robbie, K. and M.J. Brett, *Sculptured thin films and glancing angle deposition: growth mechanics and applications.* J. Vac. Sci. Technol. A, 1997. **15**: p. 1460-1465.
25. Kennedy, S.R. and M.J. Brett, *Porous broadband antireflection coating by glancing angle deposition.* Applied Optics, 2003. **42**(22): p. 4573-4579.
26. Kundt, A., *Ueber Doppelbrechung des Lichtes in Metallschichten, welche durch Zerstäuben einer Kathode hergestellt sind.* Annalen der Physik und Chemie, 1886. **263**(1): p. 59-71.
27. König, H. and G. Helwig, *Über Die Struktur Schräg Aufgedampfter Schichten Und Ihr Einfluss Auf Die Entwicklung Submikroskopischer Oberflächenrauhigkeiten.* Optik, 1950. **6**(2): p. 111-124.
28. Nieuwenhuizen, J.M. and H.B. Haanstra, *Microfractography of thin films.* Phillips Tech. Rev., 1966. **27**: p. 4.
29. Hawkeye, M.M., M.T. Taschuk, and M.J. Brett, *Glancing Angle Deposition of Thin Films: Engineering the Nanoscale*. 2014: Wiley
30. Young, N.O. and J. Kowal, *Optically active fluorite films.* Nature, 1959. **183**: p. 104-105.
31. Summers, M.A. and M.J. Brett, *Optimization of periodic column growth in glancing angle deposition for photonic crystal fabrication.* Nanotechnology, 2008. **19**(41): p. 415203.
32. Summers, M.A., K. Tabunshchyk, A. Kovalenko, and M.J. Brett, *Fabrication of 2D–3D photonic crystal heterostructures by glancing angle deposition.* Photonics and Nanostructures - Fundamentals and Applications, 2009. **7**(2): p. 76-84.
33. Ye, D.X., T. Karabacak, B.K. Lim, G.C. Wang, and T.M. Lu, *Growth of uniformly aligned nanorod arrays by oblique angle deposition with two-phase substrate rotation.* Nanotechnology, 2004. **15**(7): p. 817-821.
34. Lakhtakia, A. and R. Messier, *Sculptured thin films : nanoengineered morphology and optics*. Press monograph series. 2005, Bellingham, Wash.: SPIE Press. xxv, 299 p.
35. Mizutani, T., *Correct substrate temperature monitoring with infrared optical pyrometer for molecular-beam epitaxy of III–V semiconductors.* Journal of Vacuum Science & Technology B: Microelectronics Processing and Phenomena, 1988. **6**(6): p. 1671-1677.
36. Murray, J. and A. McAlister, *The Al-Si (aluminum-silicon) system.* Bulletin of alloy phase diagrams, 1984. **5**(1): p. 74.

37. Mouser, *MAX31855 Datasheet Rev 5*, 2015, *https://www.mouser.de/datasheet/2/256/MAX31855-73339.pdf*
38. NIST, *NIST Data Homepage*, 1995, *https://srdata.nist.gov/its90/type_k/kcoefficients_inverse.html*
39. Liedtke, S., C. Grüner, J.W. Gerlach, and B. Rauschenbach, *Comparative study of sculptured metallic thin films deposited by oblique angle deposition at different temperatures.* Beilstein journal of nanotechnology, 2018. **9**: p. 954.
40. Álvarez, R., J.M. García-Martín, M. Macías-Montero, L. González-García, J.C. González, V. Rico, J. Perlich, J. Cotrino, A. González-Elipe, and A. Palmero, *Growth regimes of porous gold thin films deposited by magnetron sputtering at oblique incidence: from compact to columnar microstructures.* Nanotechnology, 2013. **24**(4): p. 045604.
41. Alvarez, R., J.M. Garcia-Martin, M.C. Lopez-Santos, V. Rico, F.J. Ferrer, J. Cotrino, A.R. Gonzalez-Elipe, and A. Palmero, *On the deposition rates of magnetron sputtered thin films at oblique angles.* Plasma Processes and Polymers, 2014. **11**(6): p. 571-576.
42. Zeuner, M., F. Scholze, B. Dathe, and H. Neumann, *Optimisation and characterisation of a TCP type RF broad beam ion source.* Surface and Coatings Technology, 2001. **142**: p. 39-48.
43. Kennedy, S.R., M.J. Brett, O. Toader, and S. John, *Fabrication of tetragonal square spiral photonic crystals.* Nano letters, 2002. **2**(1): p. 59-62.
44. Chang, T.-W., M.R. Gartia, S. Seo, A. Hsiao, and G.L. Liu, *A wafer-scale backplane-assisted resonating nanoantenna array SERS device created by tunable thermal dewetting nanofabrication.* Nanotechnology, 2014. **25**(14): p. 145304.
45. Krishnamoorthy, S., C. Hinderling, and H. Heinzelmann, *Nanoscale patterning with block copolymers.* Materials Today, 2006. **9**(9): p. 40-47.
46. Hulteen, J.C. and R.P. Van Duyne, *Nanosphere lithography: A materials general fabrication process for periodic particle array surfaces.* Journal of Vacuum Science & Technology A: Vacuum, Surfaces, and Films, 1995. **13**(3): p. 1553-1558.
47. Winzer, M., M. Kleiber, N. Dix, and R. Wiesendanger, *Fabrication of nano-dot- and nano-ring-arrays by nanosphere lithography.* Applied Physics A, 1996. **63**(6): p. 617-619.
48. Martín-Palma, R.J., M. Manso-Silván, A. Lakhtakia, and C.G. Pantano, *Ordered arrays of nanocolumns grown by the oblique angle deposition technique on a self-assembled layer of polystyrene spheres.* Materials Letters, 2009. **63**(2): p. 197-199.
49. Kumnorkaew, P., Y.-K. Ee, N. Tansu, and J.F. Gilchrist, *Investigation of the deposition of microsphere monolayers for fabrication of microlens arrays.* Langmuir, 2008. **24**(21): p. 12150-12157.
50. Ye, X. and L. Qi, *Recent advances in fabrication of monolayer colloidal crystals and their inverse replicas.* Science China Chemistry, 2014. **57**(1): p. 58-69.
51. Stavroulakis, P.I., N. Christou, and D. Bagnall, *Improved deposition of large scale ordered nanosphere monolayers via liquid surface self-assembly.* Materials Science and Engineering: B, 2009. **165**(3): p. 186-189.
52. Abràmoff, M.D., P.J. Magalhães, and S.J. Ram, *Image processing with ImageJ.* Biophotonics international, 2004. **11**(7): p. 36-42.
53. Rasband, W., *ImageJ: Image processing and analysis in Java.* Astrophysics Source Code Library, 2012.

54. Als-Nielsen, J. and D. McMorrow, *Elements of modern X-ray physics*. 2011: John Wiley & Sons.
55. Tiilikainen, J., J.-M. Tilli, V. Bosund, M. Mattila, T. Hakkarainen, J. Sormunen, and H. Lipsanen, *Accuracy in x-ray reflectivity analysis.* Journal of Physics D: Applied Physics, 2007. **40**(23): p. 7497.
56. Warren, B.E., *X-ray Diffraction*. 1990: Courier Corporation.
57. Cullity, B.D. and S.R. Stock, *Elements of X-ray Diffraction*. 2014: Pearson Education.
58. Colthup, N., *Introduction to infrared and Raman spectroscopy*. 2012: Elsevier.
59. Benninghoven, A., F. Rudenauer, and H.W. Werner, *Secondary ion mass spectrometry: basic concepts, instrumental aspects, applications and trends.* 1987.
60. Kesapragada, S.V. and D. Gall, *Anisotropic broadening of Cu nanorods during glancing angle deposition.* Applied Physics Letters, 2006. **89**(20): p. 203121.
61. Karabacak, T., J.P. Singh, Y.P. Zhao, G.C. Wang, and T.M. Lu, *Scaling during shadowing growth of isolated nanocolumns.* Physical Review B, 2003. **68**(12).
62. Liedtke, S., C. Grüner, A. Lotnyk, and B. Rauschenbach, *Glancing angle deposition of sculptured thin metal films at room temperature.* Nanotechnology, 2017. **28**(38): p. 385604.
63. Smith, D.O., M.S. Cohen, and G.P. Weiss, *Oblique-Incidence Anisotropy in Evaporated Permalloy Films.* Journal of Applied Physics, 1960. **31**(10): p. 1755-1762.
64. Park, Y., E.E. Fullerton, and S.D. Bader, *Growth-induced uniaxial in-plane magnetic anisotropy for ultrathin Fe deposited on MgO(001) by oblique-incidence molecular beam epitaxy.* Applied Physics Letters, 1995. **66**(16): p. 2140-2142.
65. Messier, R., T. Gehrke, C. Frankel, V.C. Venugopal, W. Otaño, and A. Lakhtakia, *Engineered sculptured nematic thin films.* Journal of Vacuum Science & Technology A: Vacuum, Surfaces, and Films, 1997. **15**(4): p. 2148-2152.
66. Krug, J., *The columnar growth angle in obliquely evaporated Thin films.* Materialwissenschaft und Werkstofftechnik, 1995. **26**(1): p. 22-26.
67. Abell, A.B., K.L. Willis, and D.A. Lange, *Mercury Intrusion Porosimetry and Image Analysis of Cement-Based Materials.* Journal of Colloid and Interface Science, 1999. **211**(1): p. 39-44.
68. Poxson, D.J., F.W. Mont, M.F. Schubert, J.K. Kim, and E.F. Schubert, *Quantification of porosity and deposition rate of nanoporous films grown by oblique-angle deposition.* Applied Physics Letters, 2008. **93**(10): p. 101914.
69. Holý, V., J. Kuběna, I. Ohlídal, K. Lischka, and W. Plotz, *X-ray reflection from rough layered systems.* Physical Review B, 1993. **47**(23): p. 15896-15903.
70. Tanto, B., G. Ten Eyck, and T.M. Lu, *A model for column angle evolution during oblique angle deposition.* Journal of Applied Physics, 2010. **108**(2): p. 026107.
71. Zhu, H., W. Cao, G.K. Larsen, R. Toole, and Y. Zhao, *Tilting angle of nanocolumnar films fabricated by oblique angle deposition.* Journal of Vacuum Science & Technology B, Nanotechnology and Microelectronics: Materials, Processing, Measurement, and Phenomena, 2012. **30**(3): p. 030606.
72. Jeong, S., *Adsorption and diffusion of a Si adatom on the H/Si(1 1 1) surface: comparison with the H/Si(0 0 1) surface.* Surface Science, 2003. **530**(3): p. 155-160.
73. Ji, J.-Y. and T.C. Shen, *Low-temperature silicon epitaxy on hydrogen-terminated Si(001) surfaces.* Physical Review B, 2004. **70**(11).

74. Lee, S.M., Y.H. Lee, and N.-g. Kim, *Role of hydrogen for adsorption and diffusion of a Si adatom on monohydride and dihydride Si (0 0 1) surfaces.* Surface science, 2000. **470**(1-2): p. 89-105.
75. Murty, M.R. and H.A. Atwater, *Silicon epitaxy on hydrogen-terminated Si (001) surfaces using thermal and energetic beams.* Surface science, 1997. **374**(1-3): p. 283-290.
76. Ogawa, N., *Curvature-dependent diffusion flow on a surface with thickness.* Physical Review E, 2010. **81**(6): p. 061113.
77. Feder, R., C. Bundesmann, H. Neumann, and B. Rauschenbach, *Ion beam sputtering of Ag–Angular and energetic distributions of sputtered and scattered particles.* Nuclear Instruments and Methods in Physics Research Section B: Beam Interactions with Materials and Atoms, 2013. **316**: p. 198-204.
78. Buzea, C., G. Beydaghyan, C. Elliott, and K. Robbie, *Control of power law scaling in the growth of silicon nanocolumn pseudo-regular arrays deposited by glancing angle deposition.* Nanotechnology, 2005. **16**(10): p. 1986-92.
79. Tang, F., T. Karabacak, L. Li, M. Pelliccione, G.C. Wang, and T.M. Lu, *Power-law scaling during shadowing growth of nanocolumns by oblique angle deposition.* Journal of Vacuum Science & Technology A: Vacuum, Surfaces, and Films, 2007. **25**(1): p. 160-166.
80. Mukherjee, S. and D. Gall, *Power law scaling during physical vapor deposition under extreme shadowing conditions.* Journal of Applied Physics, 2010. **107**(8): p. 084301.
81. Dong, L., R.W. Smith, and D.J. Srolovitz, *A two-dimensional molecular dynamics simulation of thin film growth by oblique deposition.* Journal of Applied Physics, 1996. **80**(10): p. 5682-5690.
82. Kim, B.-H. and Y.-C. Chung, *Molecular dynamics simulation of the thin film deposition of Co/Cu(111) with Pb surfactant.* Journal of Applied Physics, 2009. **106**(4): p. 044304.
83. Gilmer, G.H., H. Huang, T.D. de la Rubia, J. Dalla Torre, and F. Baumann, *Lattice Monte Carlo models of thin film deposition.* Thin Solid Films, 2000. **365**(2): p. 189-200.
84. Zhang, P., X. Zheng, S. Wu, J. Liu, and D. He, *Kinetic Monte Carlo simulation of Cu thin film growth.* Vacuum, 2004. **72**(4): p. 405-410.
85. Dagum, L. and R. Menon, *OpenMP: an industry standard API for shared-memory programming.* IEEE computational science and engineering, 1998. **5**(1): p. 46-55.
86. Marsaglia, G., *Random Number Generators.* Journal of Modern Applied Statistical Methods, 2003. **2**(1): p. 2-13.
87. Bensimon, D., *D. Bensimon, B. Shraiman and S. Liang, Phys. Lett. 102 A, 238 (1984).* Phys. Lett., 1984. **102**: p. 238.
88. Ramanlal, P. and L.M. Sander, *Theory of Ballistic Aggregation.* Physical Review Letters, 1985. **54**(16): p. 1828-1831.
89. Meakin, P., P. Ramanlal, L.M. Sander, and R.C. Ball, *Ballistic deposition on surfaces.* Physical Review A, 1986. **34**(6): p. 5091-5103.
90. Lubachevsky, B.D., V. Privman, and S.C. Roy, *Morphology of amorphous layers ballistically deposited on a planar substrate.* Physical Review E, 1993. **47**(1): p. 48-53.
91. Ye, D.X. and T.M. Lu, *Fanlike aggregations on seeds by parallel ballistic flux: Experimental results and Monte Carlo simulations of the growth of three-dimensional Si structures.* Physical Review B, 2007. **75**(11).

92. Patzig, C., T. Karabacak, B. Fuhrmann, and B. Rauschenbach, *Glancing angle sputter deposited nanostructures on rotating substrates: Experiments and simulations.* Journal of Applied Physics, 2008. **104**(9): p. 094318.
93. Tanto, B., C.F. Doiron, and T.M. Lu, *Large artificial anisotropic growth rate in on-lattice simulation of obliquely deposited nanostructures.* Phys Rev E Stat Nonlin Soft Matter Phys, 2011. **83**(1 Pt 2): p. 016703.
94. Blackburn, P. *Exploring Ballistic Deposition with PNGwriter* 2002 [cited 2018 March 21st]; Available from: http://pngwriter.sourceforge.net/examples/ballisticdeposition/index-en.php.
95. Bresenham, J.E., *Algorithm for computer control of a digital plotter.* IBM Systems Journal, 1965. **4**(1): p. 25-30.
96. Amanatides, J. and A. Woo, *A fast voxel traversal algorithm for ray tracing.* Proceedings of Eurographics '87, 1987: p. 7.
97. Sinitskii, A., S. Neumeier, J. Nelles, M. Fischler, and U. Simon, *Ordered arrays of silicon pillars with controlled height and aspect ratio.* Nanotechnology, 2007. **18**(30): p. 305307.
98. Liu, D.L., D.X. Ye, F. Khan, F. Tang, B.K. Lim, R.C. Picu, G.C. Wang, and T.M. Lu, *Mechanics of Patterned Helical Si Springs on Si Substrate.* Journal of Nanoscience and Nanotechnology, 2003. **3**(6): p. 492-495.
99. Patzig, C., B. Rauschenbach, W. Erfurth, and A. Milenin, *Ordered silicon nanostructures by ion beam induced glancing angle deposition.* Journal of Vacuum Science & Technology B: Microelectronics and Nanometer Structures, 2007. **25**(3): p. 833.
100. Lei, Y., W. Cai, and G. Wilde, *Highly ordered nanostructures with tunable size, shape and properties: A new way to surface nano-patterning using ultra-thin alumina masks.* Progress in Materials Science, 2007. **52**(4): p. 465-539.
101. Patzig, C., J. Zajadacz, K. Zimmer, R. Fechner, C. Khare, and B. Rauschenbach, *Patterning concept for sculptured nanostructures with arbitrary periods.* Applied Physics Letters, 2009. **95**(10): p. 103107.
102. Khare, C., B. Fuhrmann, H.S. Leipner, J. Bauer, and B. Rauschenbach, *Optimized growth of Ge nanorod arrays on Si patterns.* Journal of Vacuum Science & Technology A: Vacuum, Surfaces, and Films, 2011. **29**(5): p. 051501.
103. Bauer, J., M. Weise, B. Rauschenbach, N. Geyer, and B. Fuhrmann, *Shape evolution in glancing angle deposition of arranged Germanium nanocolumns.* Journal of Applied Physics, 2012. **111**(10): p. 104309.
104. Cason, C., T. Froehlich, N. Kopp, and R. Parker, *POV-Ray for Windows.* Persistence of Vision, Raytracer Pty. Ltd, Victoria, Australia. URL: http://www.povray.org, 2004.
105. Phong, B.T., *Illumination for computer generated pictures.* Communications of the ACM, 1975. **18**(6): p. 311-317.
106. Stukowski, A., *Visualization and analysis of atomistic simulation data with OVITO–the Open Visualization Tool.* Modelling and Simulation in Materials Science and Engineering, 2009. **18**(1): p. 015012.
107. Saito, Y. and S. Omura, *Domain competition during ballistic deposition: effect of surface diffusion and surface patterning.* Phys Rev E Stat Nonlin Soft Matter Phys, 2011. **84**(2 Pt 1): p. 021601.
108. Grüner, C., S. Liedtke, S.G. Mayr, and B. Rauschenbach, *Avoiding anisotropies in on-lattice simulations of ballistic deposition.* Computer Physics Communications, 2018 - under review.

109. Hodgkinson, I., Q.h. Wu, and J. Hazel, *Empirical equations for the principal refractive indices and column angle of obliquely deposited films of tantalum oxide, titanium oxide, and zirconium oxide.* Applied Optics, 1998. **37**(13): p. 2653-2659.
110. Lichter, S. and J. Chen, *Model for columnar microstructure of thin solid films.* Phys Rev Lett, 1986. **56**(13): p. 1396-1399.
111. Alvarez, R., C. Lopez-Santos, J. Parra-Barranco, V. Rico, A. Barranco, J. Cotrino, A.R. Gonzalez-Elipe, and A. Palmero, *Nanocolumnar growth of thin films deposited at oblique angles: Beyond the tangent rule.* Journal of Vacuum Science & Technology B, Nanotechnology and Microelectronics: Materials, Processing, Measurement, and Phenomena, 2014. **32**(4): p. 041802.
112. Grüner, C., S. Liedtke, J. Bauer, S.G. Mayr, and B. Rauschenbach, *Morphology of Thin Films Formed by Oblique Physical Vapor Deposition.* ACS Applied Nano Materials, 2018. **1**(3): p. 1370-1376.
113. Li, J., H. Yu, and Y. Li, *Aligned Si nanowire-based solar cells.* Nanoscale, 2011. **3**(12): p. 4888.
114. Koynov, S., M.S. Brandt, and M. Stutzmann, *Black nonreflecting silicon surfaces for solar cells.* Applied Physics Letters, 2006. **88**(20): p. 203107.
115. Tian, B., X. Zheng, T.J. Kempa, Y. Fang, N. Yu, G. Yu, J. Huang, and C.M. Lieber, *Coaxial silicon nanowires as solar cells and nanoelectronic power sources.* Nature, 2007. **449**(7164): p. 885-9.
116. Kayes, B.M., H.A. Atwater, and N.S. Lewis, *Comparison of the device physics principles of planar and radial p-n junction nanorod solar cells.* Journal of Applied Physics, 2005. **97**(11): p. 114302.
117. Peters, M., J. Christoph Goldschmidt, and B. Bläsi, *Efficiency limit and example of a photonic solar cell.* Journal of Applied Physics, 2011. **110**(4): p. 043104.
118. Peköz, R., O.B. Malcıoğlu, and J.Y. Raty, *First-principles design of efficient solar cells using two-dimensional arrays of core-shell and layered SiGe nanowires.* Physical Review B, 2011. **83**(3).
119. Yang, X., A.C. To, and R. Tian, *Anomalous heat conduction behavior in thin finite-size silicon nanowires.* Nanotechnology, 2010. **21**(15): p. 155704.
120. Donadio, D. and G. Galli, *Atomistic simulations of heat transport in silicon nanowires.* Phys Rev Lett, 2009. **102**(19): p. 195901.
121. Wang, Z. and N. Mingo, *Diameter dependence of SiGe nanowire thermal conductivity.* Applied Physics Letters, 2010. **97**(10): p. 101903.
122. Hochbaum, A.I., R. Chen, R.D. Delgado, W. Liang, E.C. Garnett, M. Najarian, A. Majumdar, and P. Yang, *Enhanced thermoelectric performance of rough silicon nanowires.* Nature, 2008. **451**(7175): p. 163-7.
123. Kesapragada, S.V., P. Victor, O. Nalamasu, and D. Gall, *Nanospring Pressure Sensors Grown by Glancing Angle Deposition.* Nano Letters, 2006. **6**(4): p. 854-857.
124. Patzig, C. and B. Rauschenbach, *Temperature effect on the glancing angle deposition of Si sculptured thin films.* Journal of Vacuum Science & Technology A: Vacuum, Surfaces, and Films, 2008. **26**(4): p. 881-886.
125. Deniz, D. and R.J. Lad, *Temperature threshold for nanorod structuring of metal and oxide films grown by glancing angle deposition.* Journal of Vacuum Science & Technology A: Vacuum, Surfaces, and Films, 2011. **29**(1): p. 011020.
126. Kaplan, R., B. Kaplan, and S.S. Hegedus, *A comparative study of photoconductivity and carrier transport in a-Si:H p–i–n solar cells with different back contacts.* Solid-State Electronics, 2010. **54**(1): p. 22-27.

127. Orduña-Diaz, A., C.G. Treviño-Palacios, M. Rojas-Lopez, R. Delgado-Macuil, V.L. Gayou, and A. Torres-Jacome, *FTIR and electrical characterization of a-Si:H layers deposited by PECVD at different boron ratios.* Materials Science and Engineering: B, 2010. **174**(1-3): p. 93-96.
128. Shah, A., J. Meier, A. Buechel, U. Kroll, J. Steinhauser, F. Meillaud, H. Schade, and D. Dominé, *Towards very low-cost mass production of thin-film silicon photovoltaic (PV) solar modules on glass.* Thin Solid Films, 2006. **502**(1): p. 292-299.
129. Street, R.A., *Hydrogenated Amorphous Silicon*. 2005: Cambridge University Press.
130. Street, R.A., *Doping and the Fermi energy in amorphous silicon.* Physical Review Letters, 1982. **49**(16): p. 1187.
131. Biegelsen, D.K. and M. Stutzmann, *Hyperfine studies of dangling bonds in amorphous silicon.* Physical Review B, 1986. **33**(5): p. 3006.
132. Jackson, W.B. and N.M. Amer, *Direct measurement of gap-state absorption in hydrogenated amorphous silicon by photothermal deflection spectroscopy.* Physical Review B, 1982. **25**(8): p. 5559.
133. Spear, W. and P. Le Comber, *Substitutional doping of amorphous silicon.* Solid state communications, 1975. **17**(9): p. 1193-1196.
134. Van de Walle, C.G., *Energies of various configurations of hydrogen in silicon.* Physical Review B, 1994. **49**(7): p. 4579.
135. Lim, P.K., W.K. Tam, L.F. Yeung, and F.M. Lam, *Effect of hydrogen on dangling bond in a-Si thin film.* Journal of Physics: Conference Series, 2007. **61**: p. 708-712.
136. Spear, W., P. Le Comber, and A. Snell, *An investigation of the amorphous-silicon barrier and pn junction.* Philosophical Magazine B, 1978. **38**(3): p. 303-317.
137. Spear, W., P. Le Comber, S. Kinmond, and M. Brodsky, *Amorphous silicon p-n junction.* Applied Physics Letters, 1976. **28**(2): p. 105-107.
138. Wronski, C. and D. Carlson, *Surface states and barrier heights of metal-amorphous silicon schottky barriers.* Solid State Communications, 1977. **23**(7): p. 421-424.
139. Deneuville, A. and M. Brodsky, *Influence of preparation conditions on forward-bias currents of amorphous silicon Schottky diodes.* Journal of Applied Physics, 1979. **50**(3): p. 1414-1421.
140. *QuickField*. 2014, Tera Analysis Ltd.
141. Kuo, Y., H. Nominanda, M. Ristova, H. Lee, and J. Tewg. *Boron-doped a-Si: H thin film deposition process and applications in p-channel thin film transistor and photodiode for He-Ne laser light detection*. in *Thin Film Transistor Technologies VI: Proceedings of the International Symposium*. 2003. The Electrochemical Society.
142. Brodsky, M., M. Cardona, and J. Cuomo, *Infrared and Raman spectra of the silicon-hydrogen bonds in amorphous silicon prepared by glow discharge and sputtering.* Physical Review B, 1977. **16**(8): p. 3556.
143. Pankove, J., D. Carlson, J. Berkeyheiser, and R. Wance, *Neutralization of shallow acceptor levels in silicon by atomic hydrogen.* Physical review letters, 1983. **51**(24): p. 2224.
144. Fedders, P. and D. Drabold, *Theory of boron doping in a-Si: H.* Physical Review B, 1997. **56**(4): p. 1864.

145. Pandey, A., B. Cai, N. Podraza, and D. Drabold, *Electrical activity of boron and phosphorus in hydrogenated amorphous silicon.* Physical Review Applied, 2014. **2**(5): p. 054005.
146. Cai, B. and D.A. Drabold, *The electronic activity of boron and phosphorus impurities in a-Si and a-Si: H.* arXiv preprint arXiv:1105.1538, 2011.
147. Mirabella, S., D. De Salvador, E. Bruno, E. Napolitani, E.F. Pecora, S. Boninelli, and F. Priolo, *Mechanism of boron diffusion in amorphous silicon.* Physical review letters, 2008. **100**(15): p. 155901.
148. De Salvador, D., E. Napolitani, S. Mirabella, E. Bruno, G. Impellizzeri, G. Bisognin, E.F. Pecora, F. Priolo, and A. Carnera, *Experimental investigations of boron diffusion mechanisms in crystalline and amorphous silicon.* Materials Science and Engineering: B, 2008. **154-155**: p. 240-246.
149. Venezia, V.C., R. Duffy, L. Pelaz, M.J.P. Hopstaken, G.C.J. Maas, T. Dao, Y. Tamminga, and P. Graat, *Boron diffusion in amorphous silicon.* Materials Science and Engineering: B, 2005. **124-125**: p. 245-248.
150. Boukai, A.I., Y. Bunimovich, J. Tahir-Kheli, J.K. Yu, W.A. Goddard, 3rd, and J.R. Heath, *Silicon nanowires as efficient thermoelectric materials.* Nature, 2008. **451**(7175): p. 168-71.
151. Wang, Z.L. and J. Song, *Piezoelectric nanogenerators based on zinc oxide nanowire arrays.* Science, 2006. **312**(5771): p. 242-246.
152. Tan, S., Z. Tang, X. Liang, and N.A. Kotov, *Resonance tunneling diode structures on CdTe nanowires made by conductive AFM.* Nano Letters, 2004. **4**(9): p. 1637-1641.
153. Abdulhalim, I., M. Zourob, and A. Lakhtakia, *Surface Plasmon Resonance for Biosensing: A Mini-Review.* Electromagnetics, 2008. **28**(3): p. 214-242.
154. Shalabney, A. and I. Abdulhalim, *Sensitivity-enhancement methods for surface plasmon sensors.* Laser & Photonics Reviews, 2011. **5**(4): p. 571-606.
155. Fleischmann, M., P.J. Hendra, and A.J. McQuillan, *Raman spectra of pyridine adsorbed at a silver electrode.* Chemical Physics Letters, 1974. **26**(2): p. 163-166.
156. Albrecht, M.G. and J.A. Creighton, *Anomalously intense Raman spectra of pyridine at a silver electrode.* Journal of the American Chemical Society, 1977. **99**(15): p. 5215-5217.
157. Smith, E. and G. Dent, *Modern Raman Spectroscopy: A Practical Approach*. 2005: Wiley.
158. Kneipp, K., M. Moskovits, and H. Kneipp, *Surface-Enhanced Raman Scattering: Physics and Applications*. 2006: Springer Berlin Heidelberg.
159. Petrov, D., *Commentary: Raman nanospectroscopy of single DNA molecules.* Journal of Nanophotonics, 2010. **4**(1): p. 040306-040306-3.
160. Lee, S.N., V. Stolarski, A. Letton, and J. Laane, *Studies of bisphenol-A–polycarbonate aging by Raman difference spectroscopy.* Journal of Molecular Structure, 2000. **521**(1–3): p. 19-24.
161. Xu, H., E.J. Bjerneld, M. Käll, and L. Börjesson, *Spectroscopy of Single Hemoglobin Molecules by Surface Enhanced Raman Scattering.* Physical Review Letters, 1999. **83**(21): p. 4357-4360.
162. Shanmukh, S., L. Jones, J. Driskell, Y. Zhao, R. Dluhy, and R.A. Tripp, *Rapid and Sensitive Detection of Respiratory Virus Molecular Signatures Using a Silver Nanorod Array SERS Substrate.* Nano Letters, 2006. **6**(11): p. 2630-2636.
163. Xu, H., J. Aizpurua, M. Käll, and P. Apell, *Electromagnetic contributions to single-molecule sensitivity in surface-enhanced Raman scattering.* Physical Review E, 2000. **62**(3): p. 4318-4324.

164. Li, A., S.K. Srivastava, I. Abdulhalim, and S. Li, *Engineering the hot spots in squared arrays of gold nanoparticles on a silver film.* Nanoscale, 2016. **8**(34): p. 15658-15664.

165. Abdulhalim, I., A. Karabchevsky, C. Patzig, B. Rauschenbach, B. Fuhrmann, E. Eltzov, R. Marks, J. Xu, F. Zhang, and A. Lakhtakia, *Surface-enhanced fluorescence from metal sculptured thin films with application to biosensing in water.* Applied Physics Letters, 2009. **94**(6): p. 063106.

166. Suzuki, M., W. Maekita, Y. Wada, K. Nagai, K. Nakajima, K. Kimura, T. Fukuoka, and Y. Mori, *Ag nanorod arrays tailored for surface-enhanced Raman imaging in the near-infrared region.* Nanotechnology, 2008. **19**(26): p. 265304.

167. Leverette, C.L., S.A. Jacobs, S. Shanmukh, S.B. Chaney, R.A. Dluhy, and Y.-P. Zhao, *Aligned Silver Nanorod Arrays as Substrates for Surface-Enhanced Infrared Absorption Spectroscopy.* Applied Spectroscopy, 2006. **60**(8): p. 906-913.

168. Tao, A., F. Kim, C. Hess, J. Goldberger, R. He, Y. Sun, Y. Xia, and P. Yang, *Langmuir−Blodgett Silver Nanowire Monolayers for Molecular Sensing Using Surface-Enhanced Raman Spectroscopy.* Nano Letters, 2003. **3**(9): p. 1229-1233.

169. Orendorff, C.J., L. Gearheart, N.R. Jana, and C.J. Murphy, *Aspect ratio dependence on surface enhanced Raman scattering using silver and gold nanorod substrates.* Phys Chem Chem Phys, 2006. **8**(1): p. 165-70.

170. Abdulhalim, I., *Plasmonic Sensing Using Metallic Nano-Sculptured Thin Films.* Small, 2014. **10**(17): p. 3499-3514.

171. Karabchevsky, A., C. Khare, B. Rauschenbach, and I. Abdulhalim, *Microspot sensing based on surface-enhanced fluorescence from nanosculptured thin films.* Journal of Nanophotonics, 2012. **6**(1): p. 061508-1-061508-12.

172. Zhou, Q., Z. Li, Y. Yang, and Z. Zhang, *Arrays of aligned, single crystalline silver nanorods for trace amount detection.* Journal of Physics D: Applied Physics, 2008. **41**(15): p. 152007.

173. Sánchez-Valencia, J.R., J. Toudert, A. Borras, C. López-Santos, A. Barranco, I.O. Feliu, and A.R. González-Elipe, *Tunable In-Plane Optical Anisotropy of Ag Nanoparticles Deposited by DC Sputtering onto SiO2 Nanocolumnar Films.* Plasmonics, 2010. **5**(3): p. 241-250.

174. Wang, F. and Y.R. Shen, *General Properties of Local Plasmons in Metal Nanostructures.* Physical Review Letters, 2006. **97**(20): p. 206806.

175. Khare, C., C. Patzig, J.W. Gerlach, B. Rauschenbach, and B. Fuhrmann, *Influence of substrate temperature on glancing angle deposited Ag nanorods.* Journal of Vacuum Science & Technology A: Vacuum, Surfaces, and Films, 2010. **28**(4): p. 1002-1009.

176. Hankus, M.E., D.N. Stratis-Cullum, and P.M. Pellegrino. *Towards advanced biological detection using surface enhanced raman scattering (SERS)-based sensors*. 2010.

177. Srivastava, S.K., C. Grüner, D. Hirsch, B. Rauschenbach, and I. Abdulhalim, *Enhanced intrinsic fluorescence from carboxidized nano-sculptured thin films of silver and their application for label free dual detection of glycated hemoglobin.* Optics Express, 2017. **25**(5): p. 4761-4772.

178. Hadjigeorgiou, K., E. Kastanos, and C. Pitris. *Multi-bacteria multi-antibiotic testing using surface enhanced Raman spectroscopy (SERS) for urinary tract infection (UTI) diagnosis*. 2013.

179. Tripp, R.A., R.A. Dluhy, and Y. Zhao, *Novel nanostructures for SERS biosensing.* Nano Today, 2008. **3**(3-4): p. 31-37.

180. Cao, Y.C., *Nanoparticles with Raman Spectroscopic Fingerprints for DNA and RNA Detection.* Science, 2002. **297**(5586): p. 1536-1540.
181. Pan, Q., X.L. Zhang, H.Y. Wu, P.W. He, F. Wang, M.S. Zhang, J.M. Hu, B. Xia, and J. Wu, *Aptamers That Preferentially Bind Type IVB Pili and Inhibit Human Monocytic-Cell Invasion by Salmonella enterica Serovar Typhi.* Antimicrobial Agents and Chemotherapy, 2005. **49**(10): p. 4052-4060.
182. Souza, G.R., D.R. Christianson, F.I. Staquicini, M.G. Ozawa, E.Y. Snyder, R.L. Sidman, J.H. Miller, W. Arap, and R. Pasqualini, *Networks of gold nanoparticles and bacteriophage as biological sensors and cell-targeting agents.* Proceedings of the National Academy of Sciences, 2006. **103**(5): p. 1215-1220.
183. Selvin , E., M.W. Steffes , H. Zhu , K. Matsushita , L. Wagenknecht , J. Pankow , J. Coresh , and F.L. Brancati *Glycated Hemoglobin, Diabetes, and Cardiovascular Risk in Nondiabetic Adults.* New England Journal of Medicine, 2010. **362**(9): p. 800-811.
184. Heinemann, L. and G. Freckmann, *Quality of HbA1c Measurement in the Practice.* Journal of Diabetes Science and Technology, 2015. **9**(3): p. 687-695.
185. Srivastava, S.K., A. Shalabney, I. Khalaila, C. Grüner, B. Rauschenbach, and I. Abdulhalim, *SERS Biosensor Using Metallic Nano-Sculptured Thin Films for the Detection of Endocrine Disrupting Compound Biomarker Vitellogenin.* Small, 2014. **10**(17): p. 3579-3587.
186. Nilsen, B.M., K. Berg, J.K. Eidem, S.-I. Kristiansen, F. Brion, J.-M. Porcher, and A. Goksøyr, *Development of quantitative vitellogenin-ELISAs for fish test species used in endocrine disruptor screening.* Analytical and Bioanalytical Chemistry, 2004. **378**(3): p. 621-633.
187. Rodríguez, E.M., D.A. Medesani, and M. Fingerman, *Endocrine disruption in crustaceans due to pollutants: A review.* Comparative Biochemistry and Physiology Part A: Molecular & Integrative Physiology, 2007. **146**(4): p. 661-671.
188. Heppell, S.A., N.D. Denslow, L.C. Folmar, and C.V. Sullivan, *Universal assay of vitellogenin as a biomarker for environmental estrogens.* Environmental Health Perspectives, 1995. **103**(Suppl 7): p. 9-15.
189. Srivastava, S.K., H.B. Hamo, A. Kushmaro, R.S. Marks, C. Grüner, B. Rauschenbach, and I. Abdulhalim, *Highly sensitive and specific detection of E. coli by a SERS nanobiosensor chip utilizing metallic nanosculptured thin films.* The Analyst, 2015. **140**(9): p. 3201-3209.
190. Kalele, S.A., A.A. Kundu, S.W. Gosavi, D.N. Deobagkar, D.D. Deobagkar, and S.K. Kulkarni, *Rapid Detection of Escherichia coli by Using Antibody-Conjugated Silver Nanoshells.* Small, 2006. **2**(3): p. 335-338.
191. Guven, B., N. Basaran-Akgul, E. Temur, U. Tamer, and İ.H. Boyacı, *SERS-based sandwich immunoassay using antibody coated magnetic nanoparticles for Escherichia coli enumeration.* The Analyst, 2011. **136**(4): p. 740-748.
192. Van Dorst, B., J. Mehta, K. Bekaert, E. Rouah-Martin, W. De Coen, P. Dubruel, R. Blust, and J. Robbens, *Recent advances in recognition elements of food and environmental biosensors: A review.* Biosensors and Bioelectronics, 2010. **26**(4): p. 1178-1194.
193. Grüner, C., I. Abdulhalim, and B. Rauschenbach, *Glancing Angle Deposition for Biosensing Applications*, in *Encyclopedia of Interfacial Chemistry*, K. Wandelt, Editor. 2018, Elsevier: Oxford. p. 129-137.
194. Han, W.-K., G.-H. Hwang, S.-J. Hong, S.-S. Kim, C.-S. Yoon, N.-J. Kwak, S.-J. Yeom, J.-H. Kim, and S.-G. Kang, *Conformal electroless deposition of Cu seed*

layer on a 60-nm trench pattern modified with a self-assembled monolayer. Microelectronic Engineering, 2009. **86**(3): p. 374-378.

195. George, S.M., *Atomic Layer Deposition: An Overview.* Chemical Reviews, 2010. **110**(1): p. 111-131.
196. Josell, D., B. Baker, C. Witt, D. Wheeler, and T.P. Moffat, *Via Filling by Electrodeposition.* Journal of The Electrochemical Society, 2002. **149**(12): p. C637.
197. Chandrasekar, M.S. and M. Pushpavanam, *Pulse and pulse reverse plating—Conceptual, advantages and applications.* Electrochimica Acta, 2008. **53**(8): p. 3313-3322.
198. Changdong, G., X. Hui, and Z. Tong-Yi, *Fabrication of high aspect ratio through-wafer copper interconnects by reverse pulse electroplating.* Journal of Micromechanics and Microengineering, 2009. **19**(6): p. 065011.
199. Grüner, C., P. Reeck, P.-P. Jacobs, S. Liedtke, A. Lotnyk, and B. Rauschenbach, *Gold coated metal nanostructures grown by glancing angle deposition and pulsed electroplating.* Physics Letters A, 2018. **382**(19): p. 1287-1290.

10 List of Abbreviations

4-ATP	4-aminothiophenol
ACCS	Active chamber cooling system
AFM	Atomic force microscopy
ALD	Atomic layer deposition
a-Si	Amorphous silicon
ATP	4-aminothiophenol
BSA	Bovine serum albumin
BSE	Back-scattered electrons
cfu	Colony forming units
CVD	Chemical vapor deposition
DC	Direct current
DDA	Digital differential analyzer
DFT	Density functional theory
DI-water	De-ionized water
DNA	Deoxyribonucleic acid
EBE	Electron beam evaporation
e-beam	Electron beam
EDC-NHS	1-Ethyl-3-(3-dimethylaminopropyl)carbodiimide – N-Hydroxysuccinimide
EDX	Energy-dispersive X-ray spectroscopy
FEM	Finite element method
FFT	Fast Fourier transform
FIB	Focused ion beam
GLAD	Glancing angle deposition
Hb	Hemoglobin
HbA1c	Glycated hemoglobin
hcp	Hexagonal close-packed
HDD	Hard disk drive
I^{2}C	Inter-Integrated Circuit
IBS	Ion beam sputtering
IBSD	Ion beam sputter deposition
LCD	Liquid-crystal display
LNSH	Liquid nitrogen cooled sample holder
MC	Monte Carlo (method)
MD	Molecular dynamics

MFC	Mass flow controller
ML	Monolayer
NSL	Nanosphere lithography
OAD	Oblique angle deposition
PCB	printed circuit board
PLD	Pulsed laser deposition
PS	Polystyrene
PSS	Polystyrene sphere
PVD	Physical vapor deposition
PWM	Pulse-width modulation
QCMB	Quartz crystal microbalance
RAM	Random-access memory
RF	Radio frequency
RT	Room temperature
sccm	Standard cubic centimeters per minute,
SDS	Sodium dodecyl sulfate
SE	Secondary electrons
SEF	Surface-enhanced fluorescence
SEIRA	Surface-enhanced infrared absorption
SEM	Scanning electron microscopy
SERS	Surface-enhanced Raman scattering / spectroscopy
SIMS	Secondary ion mass spectrometry
SMU	Source measure unit
SPI	Serial peripheral interface
TC	Thermocouple
TEM	Transmission electron microscopy
THF	Tetrahydrofuran
TMP	Turbomolecular pump
uC	Microcontroller
Vg	Vitellogenin
VTE	Vertical thickness equivalent
XRD	X-ray diffraction
XRR	X-ray reflectometry

11 Acknowledgements

First of all, I would like to thank Prof. Dr. Dr. h.c. Bernd Rauschenbach for giving me the chance to work intensively on this topic. I am also thankful for dozens, or rather hundreds, of discussions about physics and various other topics. While not always sharing the same opinions, I really appreciated them.

I also want to thank Prof. Dr. Stefan Mayr for many discussions and for initially moving me to start my own simulation code.

Further, my thanks go to Dr. Jens Bauer for introducing me to the GLAD topic and for making me familiar with vacuum technology. I thank Dr. Jürgen Gerlach for introduction to XRD and XRR, and for many discussions as well. I thank Dietmar Hirsch for introduction to SEM and for carrying out the SIMS measurements. Dr. Andriy Lotnyk carried out the TEM measurements and Agnes Mill prepared the lamellas – thank you for that. I thank Jan Lehnert for the Raman measurements and Dr. Martin Ehrhardt for laser cutting of the polyimide masks. I further want to thank Ingrid Herold and Toni Liebeskind for providing and cleaning the various used substrates and Petra Hertel for etching the trenches, used for the fan angle measurements. Huge thanks go to the IOM workshop for so many small and big constructions (as the LNSH). I also thank Marco Müller for help with the electrics and electronics and for commenting on my PCB layouts.

I am very grateful for our partner group at the Ben Gurion University in Israel, for functionalizing the Ag GLAD structures and for carrying out the SEF and SERS measurements. Particularly, my thanks go to Prof. Ibrahim Abdulhalim, Dr. Atef Shalabney, and Dr. Sachin Kumar Srivastava.

I thank all of the people that helped in the GLAD laboratory, by borrowing equipment, helping with heavy parts, and so on. These are Dr. Jürgen Gerlach, Marcel Hennes, Susann Liedtke, Michael Mensing, Thomas Pröhl, Philipp Schumacher and a few that I have probably forgotten.

Dr. Jürgen Gerlach and Susann Liedtke commented on the manuscript of this thesis – thank you!

I further gladly remember so many laughing and open-minded discussions about nearly everything thinkable with my office colleagues Annemarie Finzel, Susann Liedtke, Michael Mensing, and Xinxing Sun, and the frequent visitors Fritz Lehnert and Jan Lehnert.

Finally, I want to thank my friends, my family, and my wife Susann for tremendous support over the years. Words are not enough to describe my gratefulness.

Appendix

Appendix A

The presented device allows to acquire the thermo-voltage of up to three k-type thermocouples that are electrically connected to each other at their measurement side (‘hot junction). To avoid parasitic thermo-current flowing through the other TCs, each of the TCs is electrically isolated at the read-out side (‘cold junction’). Using reed relays, the TCs can be connected separately with a MAX31855. During measurement the TCs are sequentially measured and then disconnected again. In the following the circuit diagram and the PCB layout is presented. For further details about the signal processing and the usage, compare section 3.1.2.

Figure A.1 **a** shows the circuit diagram. The red and blue connections indicate the T- and T+ paths of the TCs. The TCs are connected pairwise to K3. The capacitors C1, C2, and C3 smooth the measured thermos-voltages. The generic ferrites avoid picking up 13.56 MHz noise, allowing to use the device in the other deposition systems as well. The used reed relays RE1 – RE6 have an internal clamping diode and can therefore be controlled directly by the ATmega328, which is the core of the used Arduino Uno board. The LEDs D1, D2 and D3 indicate which channel is actually connected to the MAX31855 and are switched by the software. The MAX31855 requires a voltage of 3.3 V that is supplied by the Arduino board. The data transfer between MAX31855 and ATmega328 utilizes SPI. As the ATmega runs at 5V, D4 and R4 as well as D5 and R5 form level shifters to protect the inputs of the MAX31855. The MISO connection does not require a level shifter, since the ATmega does not follow the typical TTL levels. It rather uses comparator inputs, detecting voltage levels higher than 2.5 V as digital HIGH, so that the 3.3 V levels of the MAX31855 can be applied directly.

The layout (as presented in Figure A.1 **b** – **d**) follows the usual Arduino Uno shield dimensions. The ground planes on both PCB sides are mainly intended to reduce thermal gradients over the board, as different temperatures at the TC-copper junctions and at the relays would induce errors in the measured thermos-voltage. The copper thickness was 35 µm and eutectic 63/37 Sn-Pb solder was used.

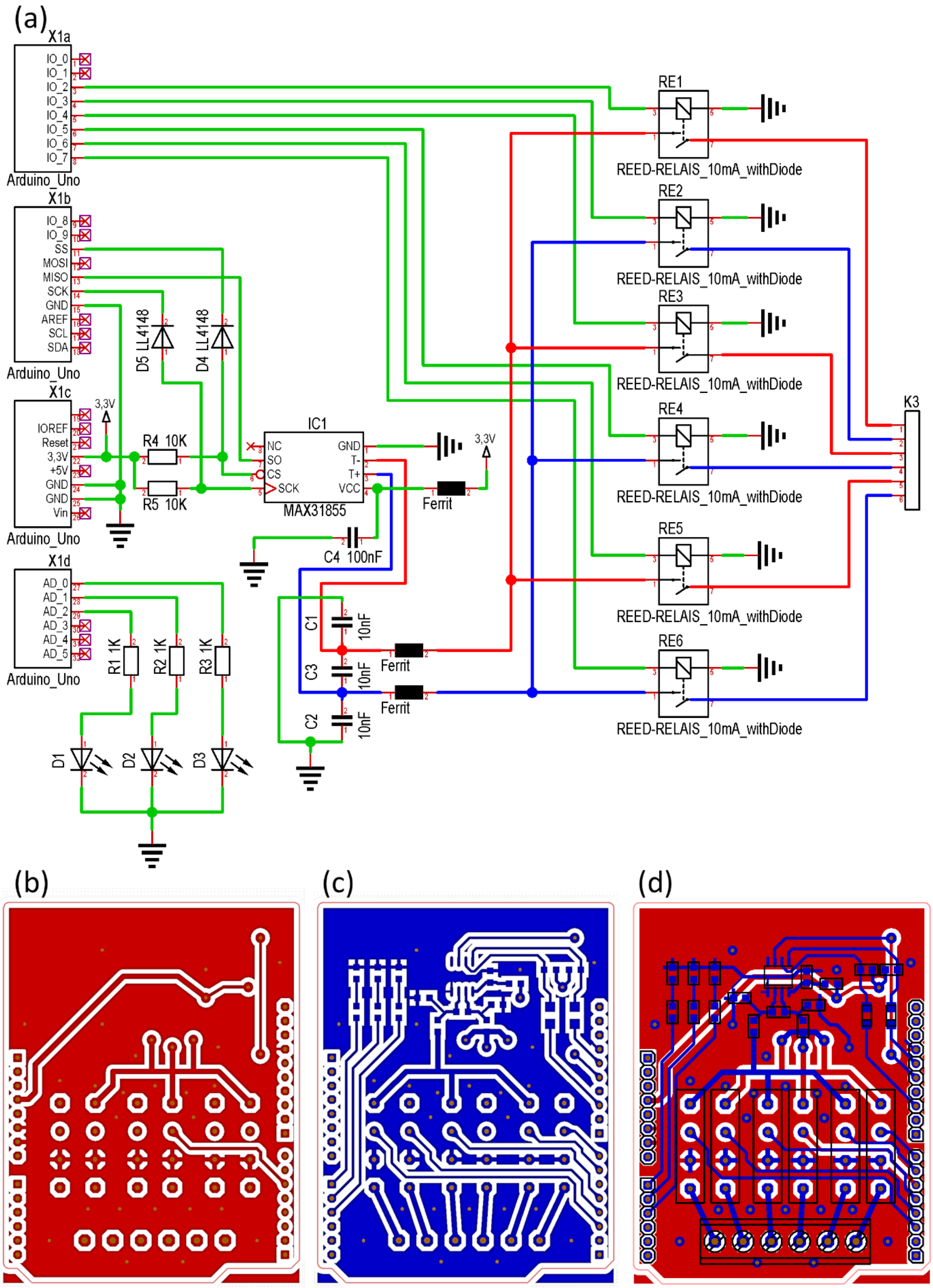

Figure A.1: (**a**) Circuit diagram of the temperature readout device for the LNSH. Corresponding PCB layout: (**b**) bottom layer, (**c**) top layer, (**d**) both layers composed (top layer without ground plane).

Appendix B

To capture the vacuum measurements from the various transceivers / gauges, a custom read-out device for the IBS chamber was developed. Despite being from different companies, all of the attached vacuum gauges require a voltage supply of 24 V DC and provide the pressure value analogous on a logarithmic 0 V – 10 V scale. In Figure A.2 the circuit diagram of the device is presented. Figure A.2 **a** shows the power supply. +24 V DC is provided by a generic external power supply and transferred to the device via a symmetric 4-pin pin header (K4). +5 V DC for the electronics is created from the 24 V by a TSR 1-2450, which is a fully integrated step-down converter. D5 protects the TSR from reverse voltages, in the case of a sudden input voltage drop. The LEDs D3 and D4 indicate the presence of the +24 V and the + 5V. The stability of the voltages is measured by the internal ADC of the Arduino Nano, utilizing the internal 1.1 V reference. Figure A.2 **b** illustrates the signal conditioning – a voltage divider and low-pass filter. The connections to the vacuum gauges are presented in Figure A.2 **c**. Each of the four channels contains a fast 1A fuse and ferrite filters. The connectors K5 – K8 are symmetric 5-pin headers with 24V – GND – signal – GND – 24V, to shield the gauge output signal from the voltage supply. Signal conditioning is similar to **b**, with the difference, that the signal is divided to fit the 0 V – 5 V range of the ADS1115. This IC is an integrated 16 bit ADC, with internal reference and an I^2C interface, as shown in Figure A.2 **d**. Since the ADS1115 has a TSSOP package with a pin pitch o 0.5 mm, soldering has to be done carefully. The measured pressures optionally can be displayed on a generic HD44780 LCD, using 4-bit interface. The connection to the LCD is presented in Figure A.2 **e** and contains a linear potentiometer to adjust the display contrast. For the final device, a 4 x 20 character display is used. Background illumination is not integrated, but might be added simply by connecting a resistor to the 24 V supply. An Arduino Nano board, containing an ATmega328 similar to the above used Arduino Uno, handles data processing. The Arduino Nano provides a better geometric form factor for the presented board, and was therefore preferred. Communication to the PC is realized by an RS232 interface, providing a higher connection stability, compared to USB. A MAX232 with the usual layout is used for this purpose. Two LEDs (D1 and D2) indicate active communication and the RS232 DST line is connected via two capacitors to the reset circuit of the ATmega. This makes it possible to program the Arduino, without using the native USB interface. The RS232 circuit it presented in Figure A.2 **g**. All capacitors smaller than 10 µF are MLCCs.

The firmware of the device reads all voltages from the ADS1115 and calculates the corresponding pressures with the formulas from the respective data sheets of the vacuum gauges. The pressures then are displayed on the LCD and transferred to the PC for further processing with the control software.

Finally, Figure A.3 shows the PCB layout, photos of the two PCB sides, and a photo of the complete device in the control rack.

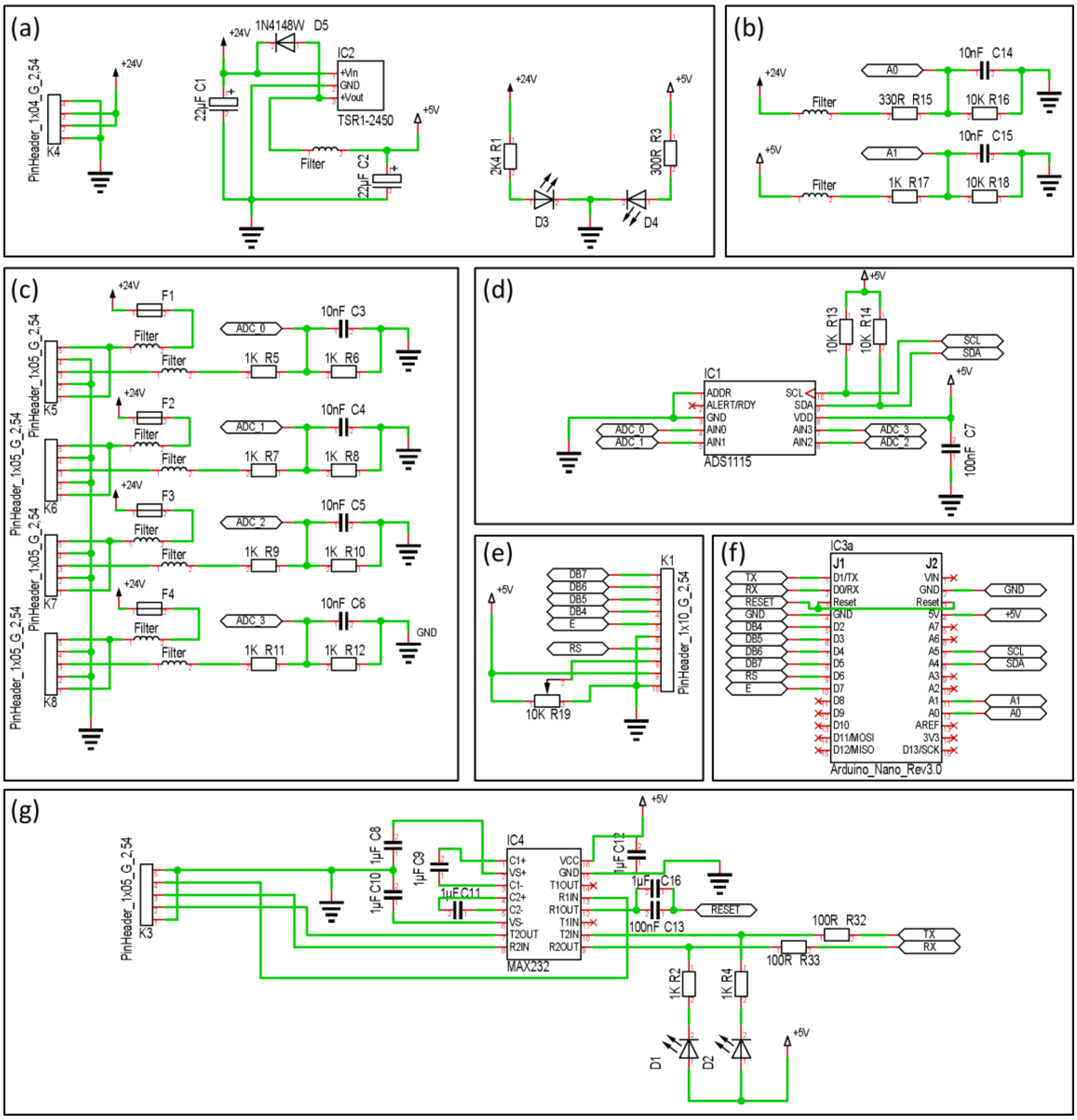

Figure A.2: Circuit diagram of the vacuum-readout for the IBS-chamber. For explanations, see text.

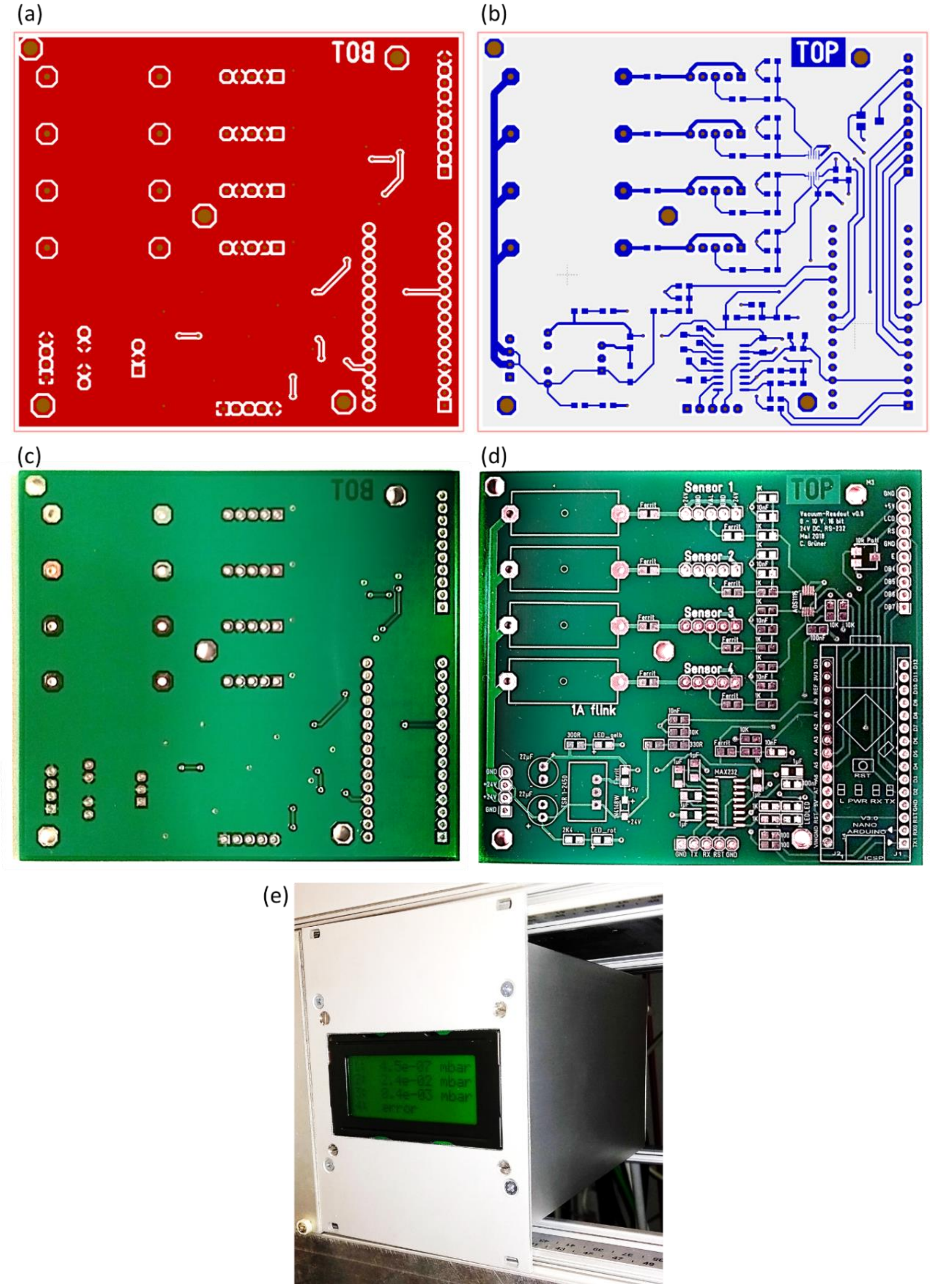

Figure A.3: (**a**), (**b**) Layout of the vacuum-readout device. (**c**), (**d**) Photos of the PCB. (**c** mirrored to fit **a**). (**e**) Photo of the complete device with the LCD, mounted to the control rack.

Publication List

The following list shows the authored and co-authored publications that are directly linked to this thesis, in the order they appear in the thesis.

[39] Liedtke, S., **C. Grüner**, J.W. Gerlach, and B. Rauschenbach, *Comparative study of sculptured metallic thin films deposited by oblique angle deposition at different temperatures.* Beilstein journal of nanotechnology, 2018. 9: p. 954.

[62] Liedtke, S., **C. Grüner**, A. Lotnyk, and B. Rauschenbach, *Glancing angle deposition of sculptured thin metal films at room temperature*. Nanotechnology, 2017. 28(38): p. 385604.

[108] **Grüner, C.**, S. Liedtke, S.G. Mayr, and B. Rauschenbach, *Avoiding anisotropies in on-lattice simulations of ballistic deposition*. Computer Physics Communications, 2018 - under review.

[112] **Grüner, C**., S. Liedtke, J. Bauer, S.G. Mayr, and B. Rauschenbach, *Morphology of Thin Films Formed by Oblique Physical Vapor Deposition.* ACS Applied Nano Materials, 2018. 1(3): p. 1370-1376.

[177] Srivastava, S.K., **C. Grüner**, D. Hirsch, B. Rauschenbach, and I. Abdulhalim, *Enhanced intrinsic fluorescence from carboxidized nano-sculptured thin films of silver and their application for label free dual detection of glycated hemoglobin*. Optics Express, 2017. 25(5): p. 4761-4772.

[185] Srivastava, S.K., A. Shalabney, I. Khalaila, **C. Grüner**, B. Rauschenbach, and I. Abdulhalim, *SERS Biosensor Using Metallic Nano-Sculptured Thin Films for the Detection of Endocrine Disrupting Compound Biomarker Vitellogenin*. Small, 2014. 10(17): p. 3579-3587.

[189] Srivastava, S.K., H.B. Hamo, A. Kushmaro, R.S. Marks, **C. Grüner**, B. Rauschenbach, and I. Abdulhalim, *Highly sensitive and specific detection of E. coli by a SERS nanobiosensor chip utilizing metallic nanosculptured thin films*. The Analyst, 2015. 140(9): p. 3201-3209.

[193] **Grüner, C.**, I. Abdulhalim, and B. Rauschenbach, *Glancing Angle Deposition for Biosensing Applications*, **invited chapter** in Encyclopedia of Interfacial Chemistry, K. Wandelt, Editor. 2018, Elsevier: Oxford. p. 129-137.

[199] **Grüner, C.**, P. Reeck, P.-P. Jacobs, S. Liedtke, A. Lotnyk, and B. Rauschenbach, *Gold coated metal nanostructures grown by glancing angle deposition and pulsed electroplating.* Physics Letters A, 2018. 382(19): p. 1287-1290.

Conference contributions as oral presentation (o) or poster (p):

- DPG Spring Meetings 2013, 2015 – 2018, Germany (2 × p, 3 × o)
- 19th International Vacuum Congress (IVC-19), Paris, France, 9.9. - 13.9. 2013 (p)
- Nanotech France, Paris, France, 28.6. - 30.6. 2017 (o)
- Leibniz MMS Days 2018, Leipzig, Germany, 28.2. - 2.3. 2018 (o)
- Materials Science and Engineering Congress - MSE 2018, Darmstadt, Germany, 26.9. - 28.9. 2018 (o)

Selbstständigkeitserklärung

Hiermit versichere ich, dass ich die vorliegende Arbeit ohne unzulässige Hilfe und ohne Benutzung anderer als der angegebenen Hilfsmittel angefertigt wurde und dass die aus fremden Quellen direkt oder indirekt übernommenen Gedanken in der Arbeit als solche kenntlich gemacht wurden.

Ich versichere, dass alle Personen, von denen ich bei der Auswahl und Auswertung des Materials sowie bei der Herstellung des Manuskripts Unterstützungsleistungen erhalten habe, in der Danksagung der vorliegenden Arbeit aufgeführt sind.

Ich versichere, dass – außer die in der Danksagung genannten – weitere Personen bei der geistigen Herstellung der vorliegenden Arbeit nicht beteiligt waren. Insbesondere versichere ich, nicht die Hilfe eines Promotionsberaters in Anspruch genommen zu haben und weitere Personen von mir oder in meinem Auftrag weder unmittelbar noch mittelbar geldwerte Leistungen für Arbeiten erhalten haben, die im Zusammenhang mit dem Inhalt der vorgelegten Dissertation stehen.

Ich versichere, dass die vorgelegte Arbeit oder Teile daraus weder im Inland noch im Ausland in gleicher oder in ähnlicher Form einer anderen Prüfungsbehörde zum Zwecke einer Promotion oder eines anderen Prüfungsverfahrens vorgelegt wurde.

Ich teile mit, dass keine früheren erfolglosen Promotionsversuche stattgefunden haben.